SYNTHESIS OF ALLOYS AND LATERAL HETEROSTRUCTURES OF ATOMICALLY THIN TRANSITION-METAL DICHALCOGENIDES FOR OPTOELECTRONIC APPLICATIONS

A Dissertation
Presented to
The Academic Faculty

by

Hossein Taghinejad

In Partial Fulfillment
of the Requirements for the Degree
Doctor of Philosophy in the
Electrical and Computer Engineering

Georgia Institute of Technology
August 2020

SYNTHESIS OF ALLOYS AND LATERAL HETEROSTRUCTURES OF ATOMICALLY THIN TRANSITION-METAL DICHALCOGENIDES FOR OPTOELECTRONIC APPLICATIONS

Approved by:

Dr. Ali Adibi, Advisor
School of Electrical and Computer Engineering
Georgia Institute of Technology

Dr. Phillip N. First
School of Physics
Georgia Institute of Technology

Dr. Eric M. Vogel
School of Materials Science and Engineering
Georgia Institute of Technology

Dr. Benjamin D. B. Klein
School of Electrical and Computer Engineering
Georgia Institute of Technology

Dr. Wenshan Cai
School of Electrical and Computer Engineering
Georgia Institute of Technology

Date Approved: April 24, 2020

I wholeheartedly dedicate this dissertation to my beloved parents and my amazing siblings, who are undoubtedly the greatest assets in my life. I sincerely thank my parents for everything they have done for me, for their unconditional love and support, for always putting me before themselves, for their countless sacrifice, and for giving me the strength to chase my dreams with commitment and persistence. Thank you Mom. Thank you Dad. You are my heroes. I am also very gratefully to my siblings, who are my role models in several ways, and from whom I always seek advice and guidance as I navigate through the ups and downs of life.

ACKNOWLEDGEMENTS

Although a PhD degree is an affidavit of some degree of resilience, perseverance, creativity, and knowledge (among other traits) for the awardee, many other individuals contribute, to different extents, to it. It is hard to clearly pinpoint and duly acknowledge these contributions. One can only try. First, I would like to sincerely thank my advisor, Dr. Ali Adibi, for his continued support throughout my PhD study at Georgia Tech. I am grateful to him for giving me the freedom and support to navigate around and purse my research passion. He is a great presenter and a very sharp learner who never forgets the importance of bigger pictures. His ability in forming big research teams, his collaborative attitude, and his leadership skills are among unique talents that he has. The lessons I learned from him will serve me for the rest of my career. I would like to thank the members of my thesis reading committee, Dr. Eric Vogel, Dr. Wenshan Cai, Dr. Phillip First, and Dr. Benjamin Kline. I would like to thank Dr. Eric Vogel and his research team (especially Dr. Alexey Tarasov, Dr. Philip Campbell, Dr. Eric Tsai, and Dr. Christopher Perini) for bringing me to speed at the early stage of my research on 2D materials. Dr. Vogel's group generously supplied large-area MoS_2 films and, more importantly, shared with me their experiences with the sulfurization furnace. I would also like to thank Dr. Wenshan Cai and his group for giving me the opportunity to engage in their exciting projects on ultrafast carrier dynamics in hybrid material platforms and most recently in 2D materials. I also thank Dr. Pulickel Ajayan and his research team in the Rice university for generously providing me with high-quality monolayer MoS_2 and $MoSe_2$ in past four years. I thank Dr. Even Reed and his group in Stanford for helping me better understand the complex

underlying alloying mechanisms from a theoretical standpoint. I am also very grateful to Dr. Reza Eftekhar, one of the brightest minds I have ever seen. Working with him was a great pleasure and of course a privilege. His great insight and fluid mind were indispensable to the progress of my projects.

Most of my experiments and material characterizations were performed in Institute for Electronic and Nanotechnology (IEN) and Materials Characterization Facilities (MCF) in Georgia Tech. I received a tremendous support for amazing engineers and scientists who work there. I would like to especially thank Mr. Gary Spinner and Walter Henderson whose leaderships have turned IEN and MCF into outstanding places for conducting state-of-the art research. I sincerely thank Eric Woods for his constant support of my characterization needs throughout my research in Georgia Tech. I also sincerely thank Rebdehavi Monikandran, Todd Walters, and Dr. Meng-Kun Tian for their support and friendship during these years. Technical support and maintenance of the sulfurization furnace was performed by Vinh Nguyen, Thomas Johnson-Averette, and Alex Gallmon. I was literary impressed by the level of knowledge and skill they put into modifying a pre-built furnace so it meets my research needs. I am also very grateful to the help and friendship of my past and present groupmates, especially Tianren Fan, Dr. Hesam Moradinejad, Sajjad Abdollahramezani, Dr. Amir Hossein Hosseinnia, and Dr. Majid Sodagar.

Most special thanks are due to my family. I am ultimately and infinitely grateful to my parents, my two sisters and two brothers. My parents did everything in their power to make sure we always had everything we needed to pursue our passion for science and learning. I love them and to them I owe everything I have, small or big. Last, but most certainly not least, comes my life-long friend, my best friend, my classmate, my colleague,

my mentor and mentee, and above all my brother, soon to be Dr. Mohammad Taghinejad with whom I have shared EVERY single step of my life. He is the best brother anyone can ask for. He has been with me in brightest and darkest days alike. I consider myself the luckiest man in the whole world for having such a brother. His contribution in my work and my life is beyond explanation. So, I don't even try to put it into words. I am proud of him and proud of our unbreakable bonds.

TABLE OF CONTENTS

LIST OF FIGURES

LIST OF SYMBOLS AND ABBREVIATIONS

TMD	Transition-Metal Dichalcogenide
HS	Heterostructure
CVD	Chemical Vapor Deposition
PVD	Physical Vapor Deposition
2D	Two-Dimensional
CMOS	Complementary Metal-Oxide-Semiconductor
Au	Gold
Mo	Molybdenum
S	Sulfur
Se	Selenium
Si	Silicon
Ti	Titanium
SiO_2	Silicon Dioxide
FIB	Focused Ion Beam
PNA	Plasmonic Nano Antenna
PL	Photoluminescence
XPS	X-Ray Photoelectron Spectroscopy
LP	Lattice Plasmon
LED	Light-Emitting Diode
ToF-SIMS	Time of Flight Secondary Ion Mass Spectroscopy
SEM	Scanning Electron Microscope
STEM	Scanning Transmission Electron Microscope

AFM	Atomic-Force Microscope
DFT	Density Functional Theory
FP	Fabry-Perot
hBN	Hexagonal Boron Nitride
FET	Field-Effect Transistor
Ga	Gallium

SUMMARY

The development of novel material platforms is the driving force behind steady advancements in microelectronics and optical sciences. Demonstrating novel functionalities, achieving faster data processing speeds, and minimizing the power consumption are the most important figures of merit, which shape the research roadmap for the discovery of new applied materials. Along this venue, most often, combing heterogeneous material is the most viable approach for simultaneously achieving these figures of merit all in one single chip. Motivated by this precedent, the objective of my research is oriented towards the implementation of a holist material platform for the synthesis of atomically thin lateral heterostructures (HSs) with engineerable morphologies and tunable optoelectronic properties in addressable sites on an electron chip. Employing the multipotent transition-metal dichalcogenide (TMD) material system, I first establish a technique for the post-growth alloying of binary TMDs and then harness it for the synthesis of patterned lateral TMD HSs using a CMOS-compatible fabrication protocol. Following a complete set of spectroscopies and characterizations, I provide detailed insights into the HS synthesis mechanism and further discuss technical challenges and viable solutions. I believe the developed knowledge in my PhD research can find immediate applications in multiple technologies including quantum information-processing, wearable devices, and the next generation of optoelectronics.

CHAPTER 1. INTRODUCTION

The never-ending interest for the development of new layered two-dimensional (2D) materials is the legacy of the graphene success. Among various 2D materials, transition-metal dichalcogenides (TMDs) with MX_2 formula (M: transition metal; X: chalcogen) have emerged as the ace of the post-graphene era. TMDs exist in various crystalline phases including semiconducting and metallic. More importantly, the electronic bandgap of the semiconducting phase can be controlled via changing M or X elements (Figure 1-1(a)), offering a digital portfolio of 2D materials for optoelectronic applications over a relatively wide optical window that covers visible and near infrared regimes. In addition, this digital portfolio can be turned into an analogue one through the alloying of 2D TMDs, a unique feature that enables the design of 2D materials with customized properties. The combination of these properties renders 2D TMDs a family materials with unmatched qualities for various applications including micro/nanoelectronics,[1-3] optoelectronics, [4-6] sensing, [7, 8] and energy harvesting. [9]

The rich diversity of material phases, electronic bandgaps and band alignments, and chemical compositions has been the motivation for employing 2D TMDs as building blocks for the realization of devices with complex functionalities as well as the exploration of novel physical phenomena. In a simple analogy, different layered TMDs can be considered as atomically thin Legos that can be vertically stacked or laterally stitched to construct engineered structures. Such a Lego-like vision has been the driving force for the synthesis of lateral (Figure 1-1(b)) and vertical (Figure 1-1(c)) heterostructures (HSs) with unprecedented properties. Early experimental demonstrations started with the vertical

stacking of heterogenous 2D materials either using the mechanical transfer of exfoliated films [11] or the direct growth of different TMDs on top of one another. [12, 13] However, the realization of lateral HSs with in-plane heterogeneities was slowed down by the development of advanced growth protocols, but it was eventually demonstrated using the edge epitaxy method. [13-15]

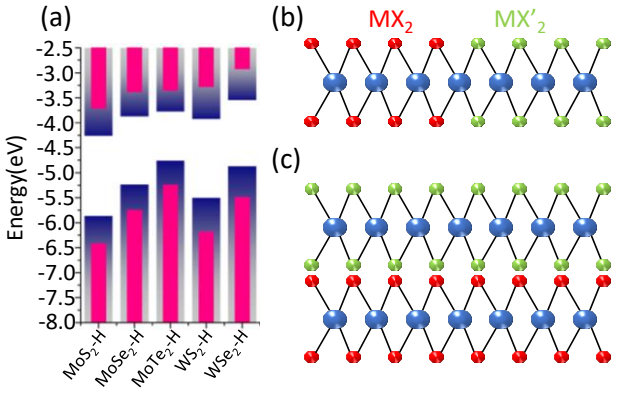

Figure 1-1: Heterostructures of TMDs. (a) The electronic bandgap and the relative alignment of band edges for several group-VI TMDs. Energies are calculated with respect to the vacuum level. (b, c) The schematic illustrations of lateral and vertical HSs, respectively. Panel (a) is adopted from. [10]

Despite the initial surge of attention to vertical HSs, lateral HSs have demonstrated a greater potential for the integration with the mainstream complementary metal-oxide-semiconductor (CMOS) fabrication processes. Indeed, the lateral nature of the junction enables (1) a straightforward electrical access to the junction area, (2) the formation of a depletion region around the junction, (3) small device footprints, and (4) in-plane carrier confinements, a set of features that are mandatory for the large-scale fabrication of fundamental optoelectronic components such as diodes and transistors. The current state-of-the-art has employed edge epitaxy methods (reviewed below) for the formation of coherent, defect-free, and atomically sharp lateral heterojunctions in atomically thin layers of TMDs. However, the edge epitaxy methods offer no control over the geometrical

parameters of HSs and often yield a mixed combination of vertical and lateral junctions in unpredictable locations across growth substrates. Such limitations have impeded the integration of this material platform into practical applications. Thus, I believe my research offers a holistic solution to the aforementioned challenges and paves the way for the faster demonstration of real-world applications based on the lateral HSs of atomically thin TMDs.

In my opinion, HS synthesis methods are often adopted versions of conventional techniques used for the alloying of 2D TMDs. Thus, in section 1.1, I will start with a brief review of mainstream strategies used for the alloying of TMD films. Then, in section 1.2, I will review the state-of-the-art methods used for the synthesis of lateral HSs.

1.1 Alloying

Alloying has long served as an irreplaceable approach for tuning optoelectronic properties of atomically thin semiconducting TMDs. In a ternary TMD alloy (i.e., $MX'_{2x}X_{2(1-x)}$ or $M'_xM_{1-x}X_2$; M, M': transition metals and X, X': chalcogens), changing the alloying ratio (i.e., x) enables tuning the bandgap of 2D materials, offering specifications that binary crystals (i.e., MX_2) fail to provide. Because of identical crystal symmetries and relatively small lattice-constant mismatch among various TMDs, thermodynamic calculations prove that 2D alloys of TMDs are stable and can be synthesized at moderate temperatures. [16] Accordingly, several studies experimentally demonstrated synthesis of ternary alloys such as $Mo_xW_{1-x}Se_2$, [17] $WS_{2x}Se_{2(1-x)}$, [18] $MoS_{2x}Se_{2(1-x)}$, [19, 20] and $Mo_xW_{1-x}S_2$. [21] In addition to the rudimentary bandgap tuning, harnessing the kinetics and thermodynamics of alloying reactions is at the heart of state-of-the-art methods that are currently being used for the synthesis of lateral and vertical HSs. Therefore, to

systematically trace the role of alloying in the formation of HSs, in the following I divide the alloying methods into two major categories that I refer to as direct and indirect (or post-growth) alloying methods. However, the mechanical exfoliation from alloyed bulk crystals (e.g., Ref. [17]) is not covered in my survey of alloying techniques, primarily because of major shortcomings for practical applications.

1.1.1 Direct Alloying

Direct alloying is based on the simultaneous reaction of multiple precursors for the synthesis of TMD alloys in a single step. In the most commonly practiced strategy (see Figure 1-2(a)), three sources (e.g., two metals and one chalcogen) are evaporated at appropriate temperatures to provide precursors for the chemical vapor deposition (CVD) [22, 23] or physical vapor deposition (PVD) [24] synthesis of a ternary alloy on a substrate that is held at the upstream of the reaction chamber. In an alternative approach called the vapor-phase transport (VPT), the solid phases of two "stoichiometric" precursors such as MoS_2 and WS_2 are simultaneously evaporated at relatively high temperatures, and the generated vapor phase of these crystals are transported via a carrier gas (usually Ar) to the colder zone of the reaction chamber, where a mixed composition (i.e., an alloy) condensates on the substrate. It is worth noting that, because of relatively stable stoichiometric precursors, the synthesis of TMD alloys via VPT method is often performed at high processing temperatures.

The direct alloying is the mainstream method for the synthesis of ternary TMD crystals because of unique flexibilities such as: compatibility with various synthesis protocols (CVD, PVD, VPT, etc.), compatibility with a diverse set of precursors, the possibility of

producing high-quality alloys with randomly mixed metals (Figure 1-2(b)) or randomly mixed chalcogens (Figure 1-2(c)), and compatibility with various substrate materials (e.g., SiO_2 and sapphire (Al_2O_3)). In this approach the ratio of precursors, the vapor pressure of individual precursors, and the reaction temperature are key parameters for controlling the optoelectronic and structural properties of alloys. However, the co-existence of multiple precursors often demands the generation of a complex temperature profile for solid-phase precursors or a complex gas-delivery system for gaseous precursors.

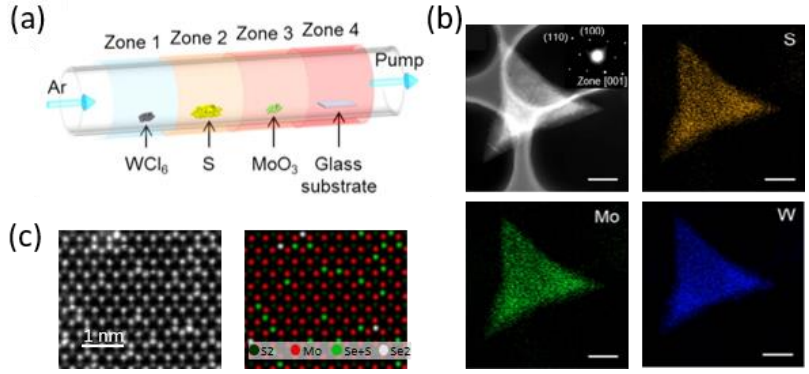

Figure 1-2: Alloying of 2D TMDs. (a) The schematic illustration of a representative direct-alloying approach in which the simultaneous reaction of WCl_6, MoO_3, and S precursors yields metal-mixed $W_xMo_{1-x}S_2$ alloys. (b) Elemental analysis using EDS spectroscopy confirms the uniform distribution of all elements (i.e., a random alloy). (c) An atomic-resolution STEM image (left) and the elemental mapping (right) of a chalcogen-mixed $MoS_{2x}Se_{2(1-x)}$ alloy synthesized via the direct reaction of MoO_3, S, and Se precursors. Similarly, a randomly mixed alloy is obtained. Panels (a, b) and (c) are adopted from [25] and [20].

1.1.2 Indirect (Post-Growth) Alloying

The indirect alloying method starts with the growth of a binary MX_2 film in the first step. In the second step, using a high-temperature annealing process in the presence of a dissimilar chalcogen vapor (i.e., X'), the X chalcogens of the MX_2 crystal are partially replaced by the X' chalcogens, which yields a ternary $MoX'_{2x}X_{2(1-x)}$ alloy. This approach is sometimes called the post-growth alloying because the allying step occurs after the

growth of a binary crystal. In this approach the degree of the elemental replacement defines the composition ration of alloys (i.e., x between 0 to 1). In comparison to the direct alloying approach, the post-growth alloying has been far less explored, mostly because of the complexity of the alloying process. Indeed, in the post-growth alloying, a well-established binary lattice- with fixed lattice parameters needs to be disturbed and converted into an alloy with different lattice parameters, a chain of changes that complicates this alloying method.

Although the indirect alloying method offers a promising direction for customizing material properties, the extension of the literature on this subject is limited to the proof-of-concept demonstrations in only a few reports, [26, 27] and important details such as chalcogen-substitution mechanism, the impact of the starting binary lattice, and substrate materials have remained largely unknown. Thus, as a part of my PhD research, I planned a set of systematic experiments followed by extensive spectroscopic characterizations to (1) shed light into the details of the indirect allying method (will be covered in CHAPTER 2 and 3), and (2) employ this method for the synthesis of lateral HSs for advanced optoelectronic devices (will be covered in CHAPTER 4 and 5).

1.2 Synthesis of Lateral HSs via Edge-Epitaxy

A lateral HS forms when two heterogenous 2D materials are brought together to form a seamless junction within an atomically thin plane (Figure 1(b)). Such junctions have been realized between various pairs of 2D materials including graphene-TMDs, [28, 29] graphene-hBN, [30] and TMD-TMD. [27, 31, 35] In this section, I will review the synthesis of junctions only made of heterogenous TMDs films.

Lateral TMD-TMD HSs were first realized using a method widely referred to as the "edge epitaxy". This technique relies on the growth of a TMD crystal on the active edge of a dissimilar TMD crystal. Indeed, because of the relatively small lattice mismatch between various TMDs, the unsaturated edge of a TMD film can serve as an active growth front for the lateral epitaxy of a dissimilar TMD film (Figure 1-3(a)). This approach has been implemented in several variations including single-step, [13, 14] two-step, [15] and sequential [31] schemes. In the single step approach, two stoichiometric TMD crystals such as MX_2 and $M'X_2$ are simultaneously placed in a single boat held at high temperatures, and the vapor phase of these two TMDs are carried to the colder zone of the reaction chamber, where they condense side by side on a substrate to form a MX_2-$M'X_2$ lateral HS. Using this strategy, several groups demonstrated the synthesis of MoS_2-WS_2, [13, 32] $MoSe_2$-WSe_2, [14] and MoS_2-$MoSe_2$ [14] lateral HSs. As exemplified in Figure 1-3(b), such HSs are composed of a central TMD crystal surrounded by a dissimilar TMD crystal on their periphery.

The edge epitaxy can be performed in a sequential mode for the synthesis of structures composed of multiple junctions between two heterogenous TMDs (Figure 1-3(e-g)). The development of such structures requires the cyclic exchange of active precursors to alternatively perform the epitaxy on the fresh edge of the last-grown TMD film. To realize such structures, selective and cyclic evaporation of "solid" TMD targets via cyclic switching of the carrier gas was proposed. [31] In this approach, solid MoX_2 and WX_2 (X: S or Se) crystals were simultaneously placed in a boat held at a moderate temperature at which neither of the crystals are volatile (thus no growth). Then, by flowing $N_2 + H_2O_{(g)}$ carrier gas into the reaction chamber the growth of only MoX_2 was promoted.

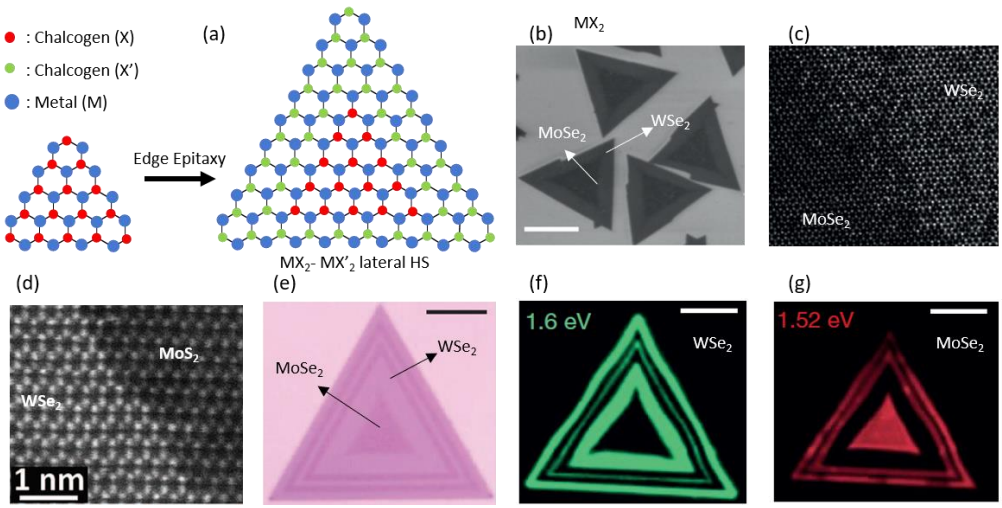

Figure 1-3: Synthesis of Lateral HSs via the edge epitaxy method. (a) The schematic illustration of the edge epitaxy for the synthesis of a MX_2-MX'_2 lateral HS. (b) The STEM image of $MoSe_2$-WSe_2 HSs synthesized through a single-step edge epitaxy. These HSs are synthesized via a single VPT step using the evaporation of $MoSe_2$ and WSe_2 powders, typically at 950 ^oC. (c) STEM images obtained at the $MoSe_2$-WSe_2 junction, which shows formation of an alloyed interface. (d) A representative STEM image that illustrates formation of an atomically sharp interface obtained via a two-step epitaxy of MoS_2 on the edge of a WSe_2 monolayer. (e) The optical image of a multi-junction $MoSe_2$-WSe_2 Lateral HS synthesized via a sequential edge epitaxy technique. (f, g) PL maps obtained at 1.6 eV (WSe_2) and 1.52 eV ($MoSe_2$) emission energies, respectively, which clearly confirms formation of a multi-junction structure. All scale bars represent 10 µm. Panels (b, c), (d), and (e-g) are adopted from [33], [15], and [32], respectively.

Subsequently, switching the carrier gas to Ar + H_2(5%) terminates the growth of MoX_2 and selectively promotes the epitaxy of WX_2 on the edge of MoX_2. Therefore, cyclic switching between the two carrier gases enables the sequential epitaxy of multiple-junction TMD HSs. In this approach, the fast depletion of pre-existing precursors is very important, otherwise the trace of precursors from a previous step leads to the formation of an alloyed junction instead of a sharp one. [31] It is worth noting that the two-step edge epitaxy method is also capable of producing sequential junctions via sequential transferring of the sample from one reaction chamber to another. However, this strategy has a very low yield and it encounters edge contamination issues because of exposing the sample to the ambient during the transfer process.

The one-step edge epitaxy approach encounters two major issues, mostly routed in the co-existence of multiple precursors in the vapor phase. First, it often yields an alloyed junction with a finite width (Figure 1-3(c)) instead of an abrupt junction with an atomically sharp interface. [13, 14] Second, the one-step nature of the process necessitates a growth condition that works for both TMD crystals that are intended to form the lateral junction. Because of this limitation, lateral HSs created by the one-pot strategy are composed of either common-chalcogen TMDs (e.g., MoS_2-WS_2) or common-metal TMDs (e.g., MoS_2-$MoSe_2$), which have relatively similar growth conditions. These two limitations are addressed in the two-step synthesis scheme in which a TMD crystal is first grown and then transferred to another chamber for the lateral epitaxy of the second TMD crystal on the edge of the first one. Such an approach offers two major advantages: (i) it eliminates the interference of the precursors needed for the growth of the two TMD films, which allows for the synthesis of atomically sharp junctions, and (ii) it enables changing both transition metal and chalcogen elements on either side of the junction, which expands the variety of lateral junctions that can be achieved via the edge epitaxy. Using this strategy, WSe_2-MoS_2 lateral HSs with atomically sharp interfaces and dissimilar chalcogens and transition metals have been demonstrated (Figure 1-3(d)). [15] However, the similarity of this approach to the post-growth alloying recipe (section 1.1.2) limits the growth sequence. Indeed, to avoid alloying or destabilizing the first-grown TMD film in the second step, the TMD film with a higher growth temperature (e.g., WSe_2, 925 ^{o}C) must be synthesized in the first step and then followed by the edge epitaxy of the second TMD crystal with a lower growth temperature (e.g., MoS_2, 755 ^{o}C).

Despite state-of-the-art demonstrations, in all variations of the edge epitaxy method, the geometrical shape of the lateral junction is strictly limited by crystal orientations, lattice symmetries, and the chirality of exposed edges. Therefore, via the edge epitaxy, lateral HSs with only certain shapes such as triangles or hexagons can be obtained. [31] In addition, the edge epitaxy yields lateral junctions in random and unpredictable locations across the growth substrate, which is a major setback for the implementation of practical devices. These two major issues have hampered widespread demonstration of optoelectronic devices based on lateral HSs of TMDs synthesized via edge epitaxy methods. To address these issues, I dedicated a significant part of my PhD work to develop alternative approaches for the fabrication of lateral TMD HSs with arbitrary shapes and arbitrary dimensions in predefined locations. As I will discuss in CHAPTERs 3 and 4, my proposed methods are rooted in the post-growth alloying technique. Considering the revolutionary impact of nano structures in various research fields including sensing [36-41] and optoelectronics [42-45], I believe that achievements of this PhD research will offer a yet another novel platform that can further enrich the portfolio of functional nanostructures.

1.3 References

1. R. P. Zhou, V. Ostwal, and J. Appenzeller, "Vertical versus lateral two-dimensional heterostructures: on the topic of atomically abrupt p/n-junctions," Nano Lett **17**, 4787 (2017).
2. M. Y. Tsai, A. Tarasov, Z. R. Hesabi, H. Taghinejad, P. M. Campbell, C. A. Joiner, A. Adibi, and E. M. Vogel, "Flexible MoS_2 field-effect transistors for gate-tunable piezoresistive strain sensors," Acs Appl Mater Inter **7**, 12850 (2015).
3. B. Radisavljevic, A. Radenovic, J. Brivio, V. Giacometti, and A. Kis, "Single-layer MoS_2 transistors," Nat Nanotechnol **6**, 147 (2011).
4. S. F. Wu, S. Buckley, J. R. Schaibley, L. F. Feng, J. Q. Yan, D. G. Mandrus, F. Hatami, W. Yao, J. Vuckovic, A. Majumdar, and X. D. Xu, "Monolayer semiconductor nanocavity lasers with ultralow thresholds," Nature **520**, 69 (2015).
5. H. Taghinejad, M. Taghinejad, A. Tarasov, M. Y. Tsai, A. H. Hosseinnia, H. Moradinejad, P. M. Campbell, A. A. Eftekhar, E. M. Vogel, and A. Adibi,

"Resonant light-induced heating in hybrid cavity-coupled 2D transition-metal dichalcogenides," Acs Photonics **3**, 700 (2016).

6. H. Taghinejad, S. H. Shams-Mousavi, Y. J. Gong, M. Taghinejad, A. A. Eftekhar, P. Ajayan, and A. Adibi, "Lattice plasmon induced large enhancement of excitonic emission in monolayer metal dichalcogenides," Plasmonics **12**, 1975 (2017).
7. B. Cho, M. G. Hahm, M. Choi, J. Yoon, A. R. Kim, Y. J. Lee, S. G. Park, J. D. Kwon, C. S. Kim, M. Song, Y. Jeong, K. S. Nam, S. Lee, T. J. Yoo, C. G. Kang, B. H. Lee, H. C. Ko, P. M. Ajayan, and D. H. Kim, "Charge-transfer-based gas sensing using atomic-layer MoS_2," Sci Rep-Uk **5**, 8052 (2015).
8. W. S. Zhang, P. P. Zhang, Z. Q. Su, and G. Wei, "Synthesis and sensor applications of MoS_2-based nanocomposites," Nanoscale **7**, 18364 (2015).
9. O. Lopez-Sanchez, D. Lembke, M. Kayci, A. Radenovic, and A. Kis, "Ultrasensitive photodetectors based on monolayer MoS_2," Nat Nanotechnol **8**, 497 (2013).
10. A. Castellanos-Gomez, M. Buscema, R. Molenaar, V. Singh, L. Janssen, H. S. J. van der Zant, and G. A. Steele, "Deterministic transfer of two-dimensional materials by all-dry viscoelastic stamping," 2D Mater **1**, 011002 (2014).
11. Y. C. Lin, R. K. Ghosh, R. Addou, N. Lu, S. M. Eichfeld, H. Zhu, M. Y. Li, X. Peng, M. J. Kim, L. J. Li, R. M. Wallace, S. Datta, and J. A. Robinson, "Atomically thin resonant tunnel diodes built from synthetic van der Waals heterostructures," Nat Commun **6**, 8311 (2015).
12. Y. J. Gong, J. H. Lin, X. L. Wang, G. Shi, S. D. Lei, Z. Lin, X. L. Zou, G. L. Ye, R. Vajtai, B. I. Yakobson, H. Terrones, M. Terrones, B. K. Tay, J. Lou, S. T. Pantelides, Z. Liu, W. Zhou, and P. M. Ajayan, "Vertical and in-plane heterostructures from WS_2/MoS_2 monolayers," Nat Mater **13**, 1135 (2014).
13. X. D. Duan, C. Wang, J. C. Shaw, R. Cheng, Y. Chen, H. L. Li, X. P. Wu, Y. Tang, Q. L. Zhang, A. L. Pan, J. H. Jiang, R. Q. Yu, Y. Huang, and X. F. Duan, "Lateral epitaxial growth of two-dimensional layered semiconductor heterojunctions," Nat Nanotechnol **9**, 1024 (2014).
14. M. Y. Li, Y. M. Shi, C. C. Cheng, L. S. Lu, Y. C. Lin, H. L. Tang, M. L. Tsai, C. W. Chu, K. H. Wei, J. H. He, W. H. Chang, K. Suenaga, and L. J. Li, "Epitaxial growth of a monolayer WSe_2-MoS_2 lateral p-n junction with an atomically sharp interface," Science **349**, 524 (2015).
15. H. P. Komsa and A. V. Krasheninnikov, "Two-dimensional transition metal dichalcogenide alloys: stability and electronic properties," J Phys Chem Lett **3**, 3652 (2012).
16. M. Zhang, J. X. Wu, Y. M. Zhu, D. O. Dumcenco, J. H. Hong, N. N. Mao, S. B. Deng, Y. F. Chen, Y. L. Yang, C. H. Jin, S. H. Chaki, Y. S. Huang, J. Zhang, and L. M. Xie, "Two-dimensional molybdenum tungsten diselenide alloys: photoluminescence, Raman scattering, and electrical transport," Acs Nano **8**, 7130 (2014).
17. X. D. Duan, C. Wang, Z. Fan, G. L. Hao, L. Z. Kou, U. Halim, H. L. Li, X. P. Wu, Y. C. Wang, J. H. Jiang, A. L. Pan, Y. Huang, R. Q. Yu, and X. F. Duan, "Synthesis of $WS_{2x}Se_{2-2x}$ alloy nanosheets with composition-tunable electronic properties," Nano Lett **16**, 264 (2016).

18. H. Taghinejad, D. A. Rehn, C. Muccianti, A. A. Eftekhar, M. K. Tian, T. R. Fan, X. Zhang, Y. Z. Meng, Y. W. Chen, T. V. Nguyen, S. F. Shi, P. M. Ajayan, J. Schaibley, E. J. Reed, and A. Adibi, "Defect-mediated alloying of monolayer transition-metal dichalcogenides," Acs Nano **12**, 12795 (2018).
19. Y. J. Gong, Z. Liu, A. R. Lupini, G. Shi, J. H. Lin, S. Najmaei, Z. Lin, A. L. Elias, A. Berkdemir, G. You, H. Terrones, M. Terrones, R. Vajtai, S. T. Pantelides, S. J. Pennycook, J. Lou, W. Zhou, and P. M. Ajayan, "Band gap engineering and layer-by-layer mapping of selenium-doped molybdenum disulfide," Nano Lett **14**, 442 (2014).
20. K. Bogaert, S. Liu, T. Liu, N. Guo, C. Zhang, S. Gradecak, and S. Garaj, "Two-dimensional $Mo_xW_{1-x}S_2$ graded alloys: growth and optical properties," Sci Rep **8**, 12889 (2018).
21. W. T. Zhang, X. D. Li, T. T. Jiang, J. L. Q. Song, Y. Lin, L. X. Zhu, and X. L. Xu, "CVD synthesis of $Mo_{(1-x)}W_xS_2$ and $MoS_{2(1-x)}Se_{2x}$ alloy monolayers aimed at tuning the bandgap of molybdenum disulfide," Nanoscale **7**, 13554 (2015).
22. S. Umrao, J. Jeon, S. M. Jeon, Y. J. Choi, and S. Lee, "A homogeneous atomic layer $MoS_{2(1-x)}Se_{2x}$ alloy prepared by low-pressure chemical vapor deposition, and its properties," Nanoscale **9**, 594 (2017).
23. Q. L. Feng, N. N. Mao, J. X. Wu, H. Xu, C. M. Wang, J. Zhang, and L. M. Xie, "Growth of $MoS_{2(1-x)}Se_{2x\ (x=0.41-1.00)}$ monolayer alloys with controlled morphology by physical vapor deposition," Acs Nano **9**, 7450 (2015).
24. M. Mahjouri-Samani, M. W. Lin, K. Wang, A. R. Lupini, J. Lee, L. Basile, A. Boulesbaa, C. M. Rouleau, A. A. Puretzky, I. N. Ivanov, K. Xiao, M. Yoon, and D. B. Geohegan, "Patterned arrays of lateral heterojunctions within monolayer two-dimensional semiconductors," Nat Commun **6**, 7749 (2015).
25. H. Taghinejad, A. A. Eftekhar, P. M. Campbell, B. Beatty, M. Taghinejad, Y. Zhou, C. J. Perini, H. Moradinejad, W. E. Henderson, E. V. Woods, X. Zhang, P. Ajayan, E. J. Reed, E. M. Vogel, and A. Adibi, "Strain relaxation via formation of cracks in compositionally modulated two-dimensional semiconductor alloys," Npj 2d Mater Appl **2**, 1 (2018).
26. S. H. Su, W. T. Hsu, C. L. Hsu, C. H. Chen, M. H. Chiu, Y. C. Lin, W. H. Chang, K. Suenaga, J. H. He, and L. J. Li, "Controllable synthesis of band-gap-tunable and monolayer transition-metal dichalcogenide alloys," Frontiers in Energy Research **2**, 27 (2014).
27. W. Wei, Y. Dai, and B. B. Huang, "Straintronics in two-dimensional in-plane heterostructures of transition-metal dichalcogenides," Phys Chem Chem Phys **19**, 663 (2017).
28. V. Rahneshin, D. A. Ziolkowska, A. McClelland, J. Cromwell, J. B. Jasinski, and B. Panchapakesan, "The coupled straintronic-photothermic effect," Sci Rep **8**, 64 (2018).
29. X. Ling, Y. X. Lin, Q. Ma, Z. Q. Wang, Y. Song, L. L. Yu, S. X. Huang, W. J. Fang, X. Zhang, A. L. Hsu, Y. Q. Bie, Y. H. Lee, Y. M. Zhu, L. J. Wu, J. Li, P. Jarillo-Herrero, M. Dresselhaus, T. Palacios, and J. Kong, "parallel stitching of 2D materials," Adv Mater **28**, 2322 (2016).

30. M. H. D. Guimaraes, H. Gao, Y. M. Han, K. Kang, S. Xie, C. J. Kim, D. A. Muller, D. C. Ralph, and J. Park, "atomically thin ohmic edge contacts between two-dimensional materials," Acs Nano **10**, 6392 (2016).
31. M. P. Levendorf, C. J. Kim, L. Brown, P. Y. Huang, R. W. Havener, D. A. Muller, and J. Park, "Graphene and boron nitride lateral heterostructures for atomically thin circuitry," Nature **488**, 627 (2012).
32. P. K. Sahoo, S. Memaran, Y. Xin, L. Balicas, and H. R. Gutierrez, "One-pot growth of two-dimensional lateral heterostructures via sequential edge-epitaxy," Nature **553**, 63 (2018).
33. K. Bogaert, S. Liu, J. Chesin, D. Titow, S. Gradecak, and S. Garaj, "Diffusion-mediated synthesis of MoS_2/WS_2 lateral heterostructures," Nano Lett **16**, 5129 (2016).
34. Y. Li, K. A. N. Duerloo, K. Wauson, and E. J. Reed, "Structural semiconductor-to-semimetal phase transition in two-dimensional materials induced by electrostatic gating," Nat Commun **7**, 10671 (2016).
35. H. Taghinejad, M.Taghinejad, A. A. Eftekhar, Z. Li, M. P. West, M. H. Javani, S. Abdollahramezani, X. Zhang, M. K. Tian, T. Johnson-Averette, P. M. Ajayan, E. M. Vogel, S. F. Shi, W. Cai, and A. Adibi, "Defect-mediated alloying of monolayer transition-metal dichalcogenides," Acs Nano (2020). DOI: https://doi.org/10.1021/acsnano.0c02885.
36. M. Abdolahad, M. Taghinejad, H. Taghinejad, M. Janmaleki, S. Mohajerzadeh, A Vertically Aligned Carbon Nanotube-Based Impedance Sensing Biosensor for Rapid and High Sensitive Detection of Cancer Cells. Lab on a Chip 12, 1183-1190 (2012).
37. M. Abdolahad, S. Mohajerzadeh, M. Janmaleki, H. Taghinejad, M. Taghinejad, Evaluation of the Shear Force of Single Cancer Cells by Vertically Aligned Carbon Nanotubes Suitable for Metastasis Diagnosis. Integrative Biology 5, 535-542 (2013).
38. M. Mashinchian, S. Bonakdar, H. Taghinejad, V. Satarifard, M. Heidari, M. Majidi, S. Sharifi, A. Peirovi, S. Saffar, M. Taghinejad, M. Abdolahad, S. Mohajerzadeh, M. A. Shokrgozar, S. M. Rezayat, M. R. Ejtehadi, M. J. Dalby, M. Mahmoudi, Cell-Imprinted Substrates Act as an Artificial Niche for Skin Regeneration. ACS applied materials & interfaces 6, 13280-13292 (2014).
39. H. Taghinejad, M. Taghinejad, M. Abdolahad, A. Saeidi, S. Mohajerzadeh, Fabrication and Modeling of High Sensitivity Humidity Sensors Based on Doped Silicon Nanowires. Sensors and Actuators B-Chem 176, 413-419 (2013).
40. M. Abdolahad, A. Saeidi, M. Janmaleki, O. Mashinchian, M. Taghinejad, H. Taghinejad, S. Azimi, M. Mahmoudi, S. Mohajerzadeh, A Single-Cell Correlative Nanoelectromechanosensing Approach to Detect Cancerous Transformation: Monitoring the Function of F-Actin Microfilaments in the Modulation of the Ion Channel Activity. Nanoscale 7, 1879-1887 (2015).
41. M. Abdolahad, H. Taghinejad, A. Saeidi, M. Taghinejad, M. Janmaleki, S. Mohajerzadeh, S. Cell Membrane Electrical Charge Investigations by Silicon Nanowires Incorporated Field Effect Transistor (Sinwfet) Suitable in Cancer Research. RSC Advances 4, 7425-7431 (2014).

42. M. Taghinejad, H. Taghinejad, M. Abdolahad, S. Mohajerzadeh, S. A Nickel-Gold Bilayer Catalyst Engineering Technique for Self-Assembled Growth of Highly Ordered Silicon Nanotubes (SiNT). Nano Letters 13, 889-897 (2013).
43. M. Taghinejad, H. Taghinejad, M. Ganji, A. Rostamian, S. Mohajerzadeh, M. Abdolahad, M. Kolahdouz, Integration of Ni2Si/Si Nanograss Heterojunction on n-MOSFET to Realize High-Sensitivity Phototransistors. IEEE Transactions on Electron Devices 61, 3239-3244 (2014).
44. H. Taghinejad, M. Taghinejad, M. Abdolahad, S. Rajabali, A. Rostamian, S. Mohajerzadeh, E. Hosseinian, The Conformal Silicon Deposition on Carbon Nanotubes as Enabled by Hydrogenated Carbon Coatings for Synthesis of Carbon/Silicon Core/Shell Heterostructure Photodiodes. Carbon 87, 299-308 (2015).
45. M. Gharooni, M. Hosseini, S. Mohajerzadeh, M. Taghinejad, H. Taghinejad, Y. Abdi, Realization of Highly Crystallographic Three-Dimensional Nanosheets by a Stress-Induced Oriented-Diffusion Method. Applied Physics Letters 105, 043110 (2014).

CHAPTER 2. POST-GROWTH ALLOYING OF MONOLAYER TRANSITION-METAL DICHALCOGENIDES

In this chapter, I will explain how a "binary" monolayer TMD crystal can be converted into a "ternary" alloy using a post-growth alloying technique. In our alloying approach, a monolayer $MoSe_2$ film serves as a host crystal in which exchanging selenium (Se) atoms with sulfur (S) atoms yields a $MoS_{2x}Se_{2(1-x)}$ ternary alloy. Such an alloying protocol will be referred to as the sulfurization process throughout this dissertation. Following a systematic variation of alloying parameters (i.e., time, temperature, etc.) combined with detailed characterization techniques, the as-prepared alloys will be studied, and the alloying process will be optimized to enable the synthesis of high-quality materials with compositionally tunable optoelectronic properties. In addition, we combine a set of systematic experiments with *ab-initio* density-functional theory (DFT) calculations to identify the nature of the alloying process, which relies on the important role of pre-existing atomic vacancies and crystal defects in the starting binary TMD film (i.e., $MoSe_2$). Our study reveals that the driving force required for the alloying of films with abundant vacancy-type defects (e.g., CVD-grown films) is significantly lower than what is required for the alloying of films with fewer vacancies (e.g., exfoliated films). Indeed, we show that pre-existing Se vacancies in the host $MoSe_2$ lattice mediate the replacement of chalcogen atoms and facilitate the synthesis of $MoS_{2x}Se_{2(1-x)}$ alloys. Our DFT calculations suggest that S atoms can bind to Se vacancies and then diffuse throughout the host $MoSe_2$ lattice *via* exchanging the position with Se vacancies, further supporting our proposed defect-mediated alloying mechanism.

2.1 Alloying Procedure

As schematically shown in Figure 2-1(a), our alloying process relies on replacing Se atoms of $MoSe_2$ monolayers by S atoms. To experimentally demonstrate such an alloying scheme, we employ a high-temperature sulfurization recipe that anneals $MoSe_2$ monolayers under the sulfur ambient in a quartz tube. A quartz crucible loaded with sulfur powder supplies the sulfur to the reaction chamber. We place the crucible 5 cm away from monolayer $MoSe_2$ samples and then evacuate the chamber to a base pressure below 10^{-4} Torr. Then, we seal the chamber and rise the pressure to 5-7 Torr by introducing argon (Ar) gas into the chamber. Subsequently, at a rate of +20 ^{o}C/min, we increase the temperature to the sulfurization temperature (700-950 ^{o}C) and anneal the sample at such a condition for a variable time. At the end of the sulfurization period, sulfur precursor is purged out of the reaction chamber by a constant flow of Ar (2000 sccm), and then furnace is cooled down to the room temperature at a rate of -20 ^{o}C/min. The sulfurization time and temperature determine the extent of the chalcogen replacement, defining the composition ratio (*i.e.*, x) in the $MoS_{2x}Se_{2(1-x)}$ alloy. The whole process is a computer-controlled recipe.

The photoluminescence (PL) spectroscopy performed on CVD-grown $MoSe_2$ samples sulfurized at different temperatures (Figure 2-1(b)) demonstrates that sulfurization at 950 ^{o}C for 20 mins leads to the complete replacement of Se atoms by S atoms, converting the starting $MoSe_2$ crystal (x = 0, PL peak ≈ 870 nm) into a MoS_2 crystal (x = 1, PL peak ≈ 680 nm). Accordingly, sulfurization at lower temperatures leads to the partial substitution of chalcogen atoms and the synthesis of ternary alloys with $0 < x < 1$. We also draw a similar conclusion from Raman spectroscopy (Figure 2-1(c)) in which, upon increasing the sulfurization temperature, the A_{1g} Raman mode of the starting $MoSe_2$ monolayer at 240

cm^{-1} gradually disappears, and the E^1_{2g} and A_{1g} modes of the MoS_2 monolayer at 381 cm^{-1} and 401 cm^{-1} emerge.

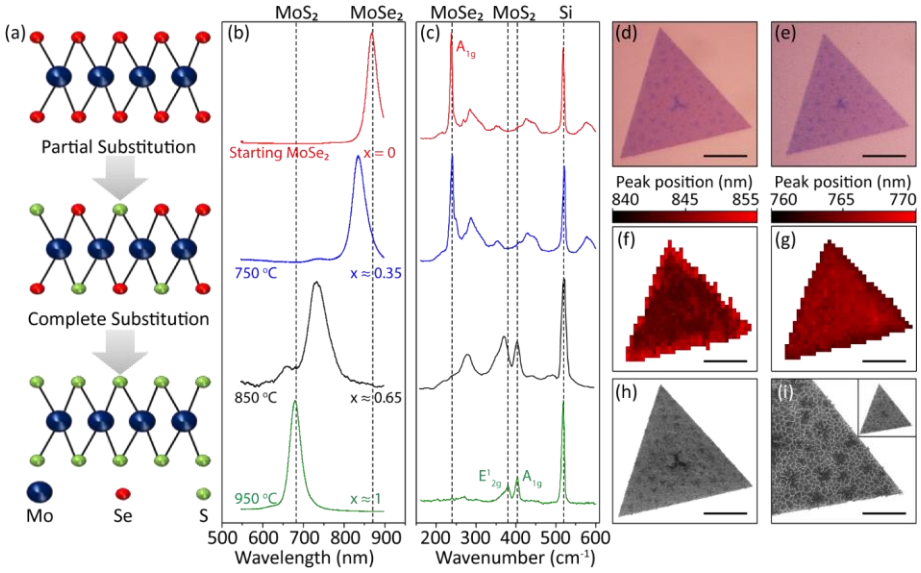

Figure 2-1: Synthesis of 2D ternary alloys *via* the atomic substitution on chalcogen sites. (a) Schematic representation of the alloying process. Using a controlled sulfurization process, the Se atoms of a starting $MoSe_2$ crystal (top) are partially replaced by S atoms, yielding $MoS_{2x}Se_{2(1-x)}$ alloys (middle). The complete replacement of chalcogens converts the $MoSe_2$ crystal into MoS_2 (bottom). (b, c) Representative PL and Raman spectra, respectively, acquired from CVD-grown $MoSe_2$ monolayers sulfurized at various temperatures for 20 mins. Composition ratios (*i.e.*, x) are marked on PL spectra in panel (b). (d, e) The optical-microscope images and (f, g) PL maps of a representative monolayer film before and after sulfurization (850 ^oC, 20 mins), respectively. Color bars in (f) and (g) represent PL peak positions. (h) The SEM image of the $MoSe_2$ film before sulfurization. (i) The SEM image taken from the bottom-right corner of the triangle after the sulfurization step, revealing that the alloying process yields a cracked film. The inset shows the whole triangle after the sulfurization step. Scale bars in (d)-(h) and (i) represent 10 µm and 5 µm, respectively.

Our characterizations show that, in comparison to the Raman spectroscopy, the PL spectroscopy offers better sensitivity to the composition variation. For example, the PL spectrum of the sample sulfurized at 750 ^oC displays a clear red-shift (~ 30 nm) from that of the starting $MoSe_2$ crystal (Figure 2-1(b)), while the Raman spectrum of this sample is relatively similar to that of the starting $MoSe_2$ film (Figure 2-1(c)). Thus, we use the PL

spectroscopy to estimate the composition ratio of $MoS_{2x}Se_{2(1-x)}$ alloys synthesized at various sulfurization conditions (labeled in Figure 2-1(b)). In addition, we employed the PL mapping before and after the sulfurization of CVD-grown $MoSe_2$ monolayers (Figure 2-1(d)-(g)) to explore the spatial uniformity of the chalcogen replacement across the plane of the 2D material. As Figure 2-1(g) shows, for a sample sulfurized at 850 ^oC for 20 mins, the PL map displays a relatively uniform emission profile (765 ± 5 nm, $x \approx 0.45 \pm 0.04$), suggesting that the chalcogen substitution takes place uniformly across the entire plane of the 2D material. Our experiments showed that such a notable spatial uniformity is also achievable in $MoS_{2x}Se_{2(1-x)}$ alloys with other values of x.

Here, I would like to briefly point to the major challenge of the post-growth alloying technique. Investigating the as-synthesized $MoS_{2x}Se_{2(1-x)}$ crystals using scanning-electron microscopy (SEM) reveals that, while the starting CVD-grown $MoSe_2$ films are seamless (Figure 2-1(h)), the sulfurization process generates fractured alloys with submicron-sized domains enclosed by cracks (Figure 2-1(i)). The origin of this phenomenon, which lies in the two-step nature of the alloying process, and practical solutions for addressing this issue will be discussed in detains in CHAPTER 3.

2.1.1 Anomalous Saturation of Chalcogen Substitution

Duration of the sulfurization process is another important parameter that affects the composition (i.e., x) of the as-synthesized alloys. The general perception is that the elongation of the sulfurization process allows for more sulfur incorporation into the starting $MoSe_2$ lattice, which yields $MoS_{2x}Se_{2(1-x)}$ alloys with larger x values. Our experiments show that, this expectation is only partially true, and it depends on the sulfurization

temperature as well. To elaborate this point in a systematic way, we performed multiple alloying runs with varying sulfurization time while keeping the temperature fixed. Results of these experiment are presented in Figure 2-2.

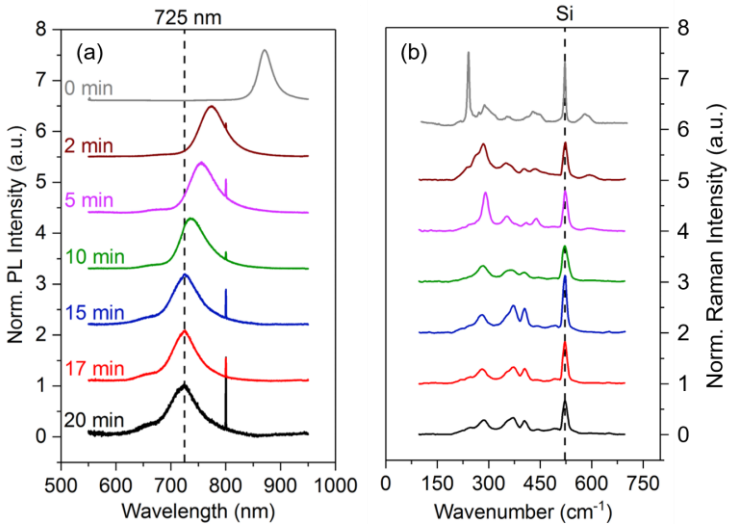

Figure 2-2: Effect of sulfurization time on the composition of the $MoS_{2x}Se_{2(1-x)}$. (a) The PL spectra of $MoSe_2$ films annealed at 850 ^oC for various sulfurization times as designated on the figure. The spectral shift of the PL becomes asymptotic after ~10 mins of sulfurization, suggesting the saturation of chalcogen substitution. (b) The Raman spectra of samples shown in panel (a). The Raman resonance of silicon at 521 cm^{-1} is used as the calibration reference.

As shown in Figure 2-2(a) at the representative temperature of 850 ^oC, by increasing the sulfurization time, the PL peak position monotonically blueshifts from ~ 825 nm (i.e., $MoSe_2$) to an asymptotic value of 725 nm. Interestingly, after 15 mins, further elongation of the sulfurization process does not shift the PL peak position anymore, though it degrades the material quality as evident by the weaker signal-to-noise ratio of the PL spectrum collected from the sample sulfurized for 20 mins. Similarly, the Raman spectroscopy in Figure 2-2(b) shows that the characteristic resonance mode of the $MoSe_2$ at ~ 241 cm^{-1} gradually weakens and the two resonance modes of MoS_2 between 390-410 cm^{-1} appear. Again, elongation of the sulfurization process beyond 15 mins, changes neither the spectral

position nor the weight of the $MoSe_2$ and MoS_2 features in the overall Raman spectrum, suggesting that the composition of the alloy has reached a saturation point.

To study the temperature dependence of this saturation effect, we performed similar experiments at two different temperatures of 800 ^oC and 950 ^oC. After each sulfurization run, we performed PL measurements to estimate the composition ratios of obtained alloys (see below for details) and related the obtained x values to the sulfurization time. As depicted in Figure 2-3, at all three temperatures, the chalcogen substitution saturates with increasing the sulfurization time, meaning that x initially increases and then asymptotically reaches to an upper value. In addition, our experiments reveal that the saturation value of x is temperature dependent and a larger portion of the Se atoms in the host $MoSe_2$ lattice can be replaced by the S atoms at higher sulfurization temperatures. Our observation is interesting in the sense that it adds an addendum to the general understanding of the role of alloying time on the extent of elemental replacement in the post-growth alloying procedures. In other words, our observation implies that the progress of chalcogen replacement with time is true for only short sulfurization processes.

We note that the exact mechanism behind the observed saturation phenomenon is still unclear to us. However, we speculate that the type and density of native defects in starting $MoSe_2$ films and their temperature-driven diffusion within the plane of the 2D material is the plays an important role. This point becomes clear in the following parts (specifically section 2.3), where we shed more light into the role of native defects in mediating the chalcogen replacement during the sulfurization process.

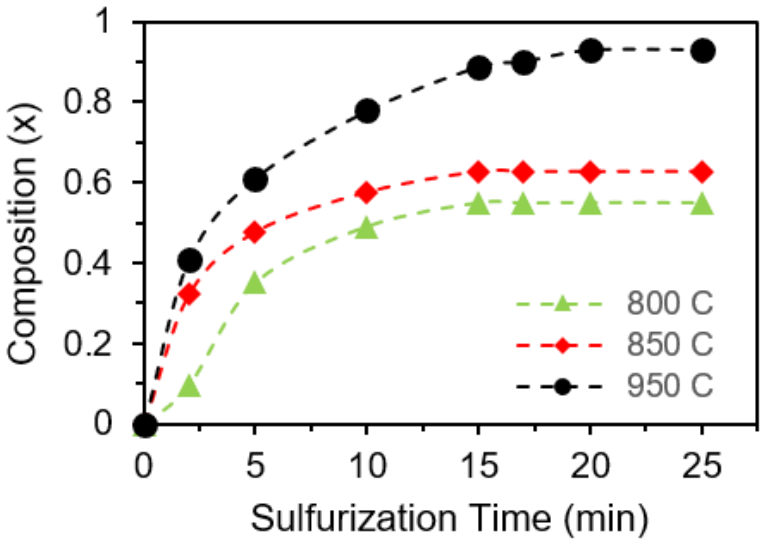

Figure 2-3: Saturation of chalcogen substitution. A temperature-dependent saturation of the alloy composition (i.e., x in $MoS_{2x}Se_{2(1-x)}$) is observed. The saturation value becomes larger as the temperature increases.

In the above discussions, we relied on the widely used bandgap criterion for the estimation of composition values at various alloying conditions. In this criterion, we use the following equation:

$$E[MoS_{2x}Se_{2(1-x)}] = x \times E[MoS_2] + (1-x) \times E[MoSe_2] \quad (1)$$

In equation 1, E represents the bandgap energy of the compound identified in brackets. Here, we have assumed that the bowing effect is negligible, in agreement with ab initio calculations. $E[MoS_2]$ and $E[MoSe_2]$ were experimentally obtained from the PL spectra of pristine CVD-grown MoS_2 and $MoSe_2$ films, respectively. $E[MoS_{2x}Se_{2(1-x)}]$ values at each alloying condition were also estimated from the PL spectra of synthesized films. Thus, using these inputs, the x values can be mathematically calculated from equation 1.

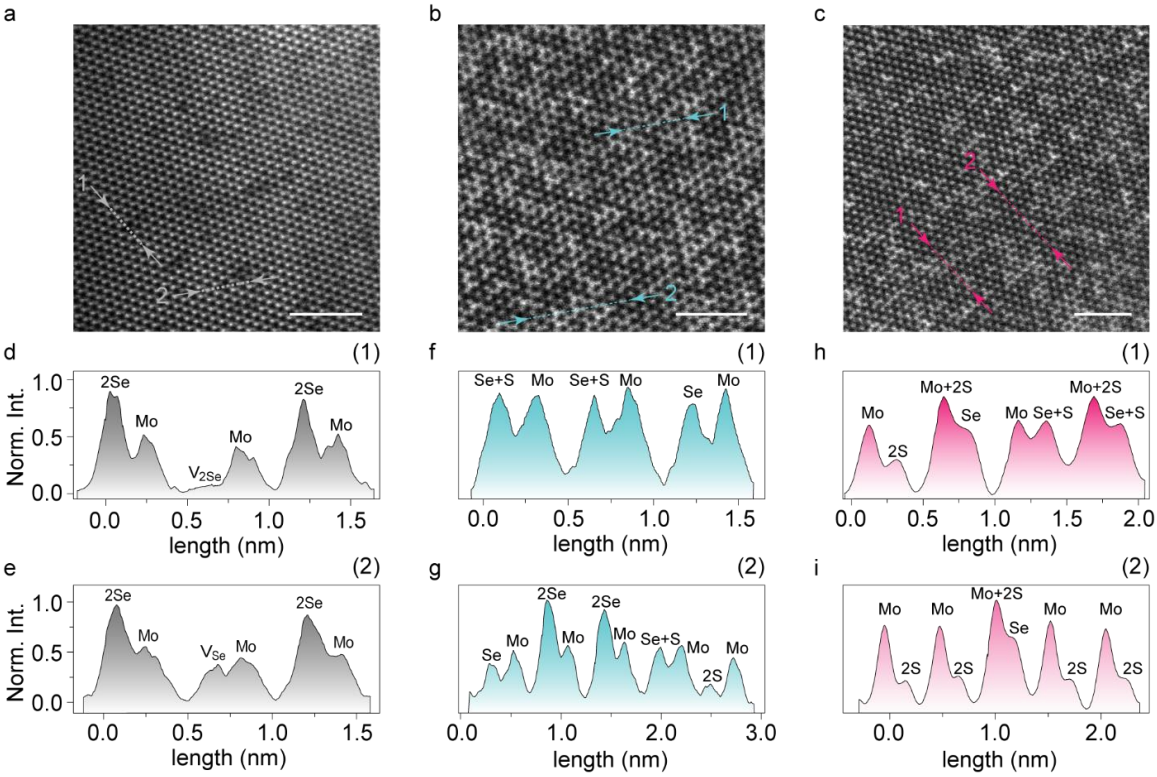

Figure 2-4: STEM analysis of atomic arrangements in $MoS_{2x}Se_{2(1-x)}$. (a-c) High-resolution STEM images of a pristine $MoSe_2$ monolayer, an alloy with $x \approx 0.35$, and an alloy with $x \approx 0.65$, respectively. (d-i) Intensity profiles along the atomic lines highlighted on panels (a-c). A random intermixing of S and Se atoms are observed. Scale bars in panels (a)-(c) represent 2 nm. (Mo: molybdenum, S: sulfur, Se: selenium, V_{Se}: single-Se vacancy, and V_{2Se}: double-Se vacancy)

2.2 Spectroscopic Characterization of $MoS_{2x}Se_{2(1-x)}$ Alloys

To better understand the structure of as-synthesized alloys, we study the atomic structure of $MoS_{2x}Se_{2(1-x)}$ films *via* conducting scanning transmission electron microscopy (STEM) on monolayer films before and after the sulfurization process. Our STEM imaging was performed in an aberration-corrected STEM tool (Hitachi HD2700) working in high-angle annular dark field (HAADF) mode at an acceleration voltage of 80 kV. We used a low current dosage (< 30 pA) to minimize the ionization damage. Our STEM characterization relies on the image-intensity variation at atomic sites for identifying the

distribution of Mo, Se, and S elements across an imaging window. In this criterion, the atomic number (Z) of elements and the number of atoms that occupy an atomic site are primary parameters that contribute to the image intensity. [1] Thus, in STEM images obtained from pristine $MoSe_2$ monolayers (Figure 2-4(a)), chalcogen columns with two Se atoms ($Z_{se} = 34$) appear brighter than metallic columns with only one Mo atom ($Z_{Mo} = 42$). Such a distinction is reflected in the intensity profiles shown in Figure 2-4(d) and (e). Moreover, our STEM analysis identifies single-Se vacancies (V_{Se}) and double-Se vacancies (V_{2Se}) in pristine $MoSe_2$ monolayers. V_{Se} and V_{2Se} can be readily determined *via* the drop of the image intensity to half and zero (*i.e.*, the background level) at chalcogen columns, as respectively shown in representative profiles in Figure 2-4(e) and (d).

Sulfurization replaces Se atoms with lighter S atoms ($Z_S = 16$), which reduces the image intensity at chalcogen sites in $MoS_{2x}Se_{2(1-x)}$ alloys, and the image becomes darker as the sulfur content (*i.e.*, x) increases. In Figure 2-4(b) and (c), we compare the STEM images taken from two different $MoS_{2x}Se_{2(1-x)}$ alloys with $x \approx 0.35$ and $x \approx 0.65$, respectively. In the sample with the lower sulfur content, most of chalcogen columns are occupied by Se+S stacks (Figure 2-4(f)), while 2S columns and 2Se columns (Figure 2-4(g)) appear at significantly smaller counts. In contrast, in the sample with the higher sulfur content, 2S columns occupy the majority of chalcogen sites, while 2Se appears in only a few atomic sits. We have also observed the stacking of sulfur atoms on the top of Mo atoms in some isolated sites (Figure 2-4(i)). Collectively, our STEM findings suggest that the insertion of S atoms into the $MoSe_2$ lattice starts with replacing only one of the Se pairs in a 2Se column, and is then followed by the replacement of the second Se atom as the composition of the alloy approaches that of MoS_2 (*i.e.*, x = 1). More importantly, our STEM analysis

reveals that the employed sulfurization process successfully yields randomly mixed Mo-S-Se alloys without any phase segregation. This point is critically important as the random mixing of Se and S enables continuous tuning of the electronic bandgap in Mo-S-Se alloys, a feature that cannot be achieved in phase segregated alloys with poor tunability. [2]

In addition to the atomic structure of the as-synthesized alloys, we also investigated the chemical properties of the sulfurized samples using X-ray photoelectron spectroscopy (XPS). Figure 2-5 shows a representative XPS spectra of a fully converted sample (i.e., x = 1) that was produced from a $MoSe_2$ monolayer sulfurized at 950 ^oC for ~15 mins. Observation of the Mo-3d doublet at ~229.5 eV and 233.8 eV and S-3p at 162.3eV and 163.8 eV confirm the formation of chemical bounds between incorporated S atoms and the Mo atoms of the host lattice, further confirming the establishment of an chemically ordered structure following the sulfurization of the sample. We note that we have also observed a pronounced MoO_3 peak at ~ 235.5 eV that could be due to the partial oxidation of the sample during exposure to the ambient or, alternatively, due to the presence of trace oxygen in the sulfurization chamber.

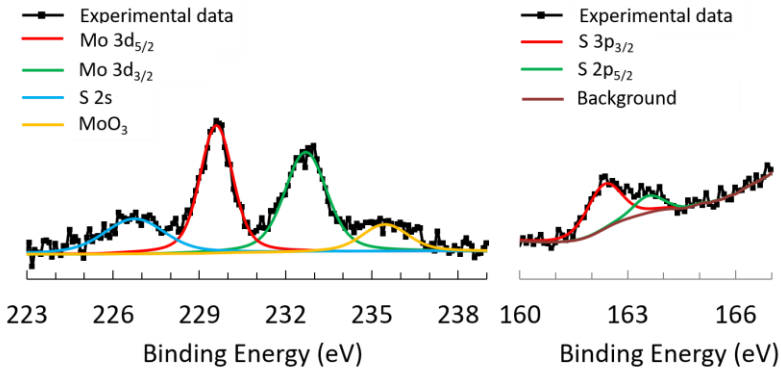

Figure 2-5: XPS analysis of converted MoS_2 monolayers. A representative XPS spectrum of a fully converted MoS_2 sample (i.e., x = 1). Squares represent experimental

data and the solid lines represent fitted curves. Mo-3d and S-3p features are separately displayed in left and right panels, respectively.

Collectively, our STEM and XPS analysis, combined with previously discussed optical spectroscopies (i.e., Raman and PL), prove that our developed post-growth alloying protocol based on controlled sulfurization of binary TMDs offers a robust approach for the synthesis of atomically mixed and chemically ordered alloys with compositionally tunable optical properties. The observation of well-defined excitonic emissions from the as-synthesized alloys further attests the high quality of $MoS_{2x}Se_{2(1-x)}$ alloys.

2.3 Alloying Mechanism: Role of Native Defects

Atomically thin nature of two-dimensional (2D) transition-metal dichalcogenides (TMDs) makes them susceptible to structural defects of various types and densities. [3-6] Native defects are intrinsically introduced during material synthesis processes, often performed at relatively high temperatures. Among various synthesis techniques, chemical-vapor deposition (CVD), [7-9] physical-vapor deposition (PVD), [10, 11] the sulfurization/selenization of transition metals, [1, 12] and the mechanical exfoliation from bulk crystals [13, 14] have attracted extensive attention to form monolayer TMD films. Accordingly, details of the synthesis process (*i.e.*, temperature, precursor gases, *etc.*) define the type and concentration of defects in monolayer TMD crystals. [15] For instance, PVD-grown monolayer TMDs primarily host a large density of anti-site defects (*e.g.*, Mo atoms occupying S sites in a MoS_2 lattice), [5] while CVD-grown and mechanically exfoliated samples mostly host chalcogen vacancies (*e.g.*, missing Se atoms in the lattice of $MoSe_2$) with considerably lower densities. [16, 17] Several studies have explored the influence of native defects on electrical, [18, 19] optical, [16, 20] mechanical, [21, 22] and electrochemical [23] properties of monolayer TMDs. These studies show that defects may

cause adverse effects such as reducing the carrier mobility of electronic devices, [18] lowering the quantum efficiency of light emitters, [16] and weakening the strength of mechanical devices [22] made of monolayer TMDs. On the other hand, defects can also be leveraged for enhancing electrochemical activities, [23] devising single-photon emissions, [24] and controlling the doping type/density [25] in 2D TMD crystals.

In the post-growth alloying approach, a binary crystal (*i.e.*, MX_2) serves as a host lattice in which native elements (*e.g.*, X) can be partially replaced by a dissimilar counterpart (*e.g.*, X') to synthesize a ternary compound (*i.e.*, $MX'_{2x}X_{2(1-x)}$). [2, 31, 32] In such a scheme, the presence of native defects in the starting host crystal may affect the details of the alloying process as well as the ultimate properties of ternary crystals synthesized *via* the post-growth alloying approach. However, despite the urge, the current span of the literature lacks a systematic study that elucidates the contribution of native defects in the alloying of monolayer TMD crystals. In this section, I bridge the gap between these two crucial subjects and unravel the interplay between "native defects" and the post-growth "alloying" of binary TMD crystals. Motivated by their widespread use, we employ CVD-grown and mechanically exfoliated $MoSe_2$ monolayers as the host binary crystal in sulfurization process. Comparing the response of these two different host materials to the sulfurization process provides unprecedent insights into the atomistic details of the post-growth alloying mechanism.

We first repeated our sulfurization process on "exfoliated" $MoSe_2$ monolayers and compared the properties of obtained alloys with those synthesized from "CVD-grown" $MoSe_2$ monolayers (as discussed in previous sections). Figure 2-6(a-d) display the optical images and PL maps of an exfoliated $MoSe_2$ film before (top row) and after (bottom row)

sulfurization at 950 ^{o}C for 15 mins. The representative PL and Raman spectra of the sample are also shown in Figure 2-6(e) and 2(f), respectively. In these figures, the blueshift of the PL peak as well as the emergence of two new Raman peaks (around 400 cm^{-1}) prove the successful incorporation of S atoms into the lattice of exfoliated $MoSe_2$ films. However, in comparison to CVD-grown crystals, the chalcogen exchange in exfoliated $MoSe_2$ monolayers is less efficient. For instance, sulfurization at 950 ^{o}C for 20 mins enables near-complete chalcogen replacement in CVD-grown $MoSe_2$ monolayers (Figure 2-1), while an identical sulfurization condition leads to only 35-50 % chalcogen replacement in exfoliated monolayer crystals (Figure 2-6).

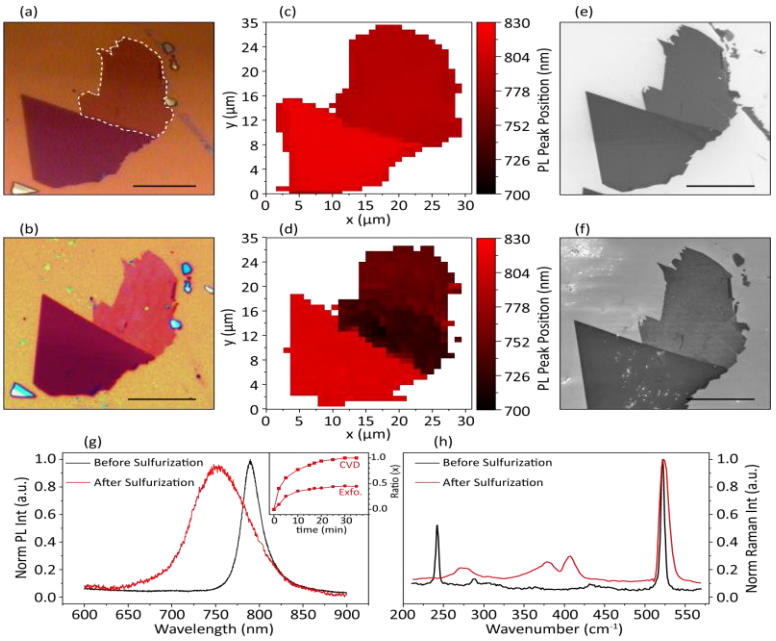

Figure 2-6: Alloying of exfoliated $MoSe_2$. (a, b) Optical images of an exfoliated $MoSe_2$ film before and after the sulfurization process (950 ^{o}C, 20 mins), respectively. The dashed line outlines the monolayer region. (c, d) The PL mapping of the sample before and after the sulfurization process, respectively. (e, f) The SEM images of the sample before and after the sulfurization process, respectively. The alloying process does not generate cracks in the exfoliated crystal. (g, h) Representative normalized PL and Raman spectra, respectively, of the sample before and after the sulfurization process. The inset of panel (g) displays x values obtained at different sulfurization times (temperature was fixed at 950 ^{o}C). Symbols represent experimental data point, and lines are guides to the eye. Scale bars represent 10 µm.

The above observation suggests that further chalcogen substitution in exfoliated $MoSe_2$ films demands sulfurization at temperatures above 950 ^oC, which is out of the reach of our experimental setup. Alternatively, we extended the sulfurization time to allow for more chalcogen substitution. However, as the inset of Figure 2-6(e) shows, the chalcogen substitution in exfoliated films saturates at $x \approx 0.45$ after ~ 30 mins of sulfurization at 950 ^oC, which is consistent with our previous discussion in section 2.1.1. Interestingly, under identical sulfurization conditions, the saturation point is at a significantly larger value of $x \approx 1$ (the inset of Figure 2-6(e)). Therefore, we conclude that replacing chalcogen atoms in exfoliated $MoSe_2$ monolayers is less efficient than that in CVD-grown samples. Considering consistent sulfurization conditions used for CVD-grown and exfoliated $MoSe_2$ monolayers, we infer that the characteristic material properties of the host $MoSe_2$ film play the primary role in the obtained attributes of the as-synthesized $MoS_{2x}Se_{2(1-x)}$ alloys. We note that, unlike CVD-grown films, exfoliated $MoSe_2$ does not crack after the post-growth alloying. Explanation of this phenomenon will be provided in the next chapter.

TMD crystals are known to host point defects of various types and densities. [3-6] Such point defects may serve as atomic-scale sites from which the S atoms incorporate into the lattice of $MoSe_2$ crystals, hence, promoting the chalcogen replacement during the sulfurization process. Therefore, probing point defects in the starting $MoSe_2$ films can shed light on the atomic-scale details of the alloying process and help explaining the different chalcogen-substitution behaviors we observed in CVD-grown and exfoliated samples (*i.e.*, the inset of Figure 2-6(e)). Point defects can be probed *via* monitoring the optical states that they induce within the bandgap of an otherwise perfect semiconductor. [16, 29] However, because of the strong thermal broadening, such mid-gap optical states should be

monitored at low temperatures. Therefore, we carried out low-temperature (~ 4K) PL spectroscopy to compare the density of pre-existing point defects in CVD-grown and exfoliated $MoSe_2$ monolayers (Figure 2-7).

The low-temperature PL spectra of exfoliated $MoSe_2$ films (Figure 2-7(a)) display two spectrally symmetric emission peaks at ~ 745 nm and ~ 760 nm associated with neutral excitons (X^o) and charged excitons (*i.e.*, trions (T)), respectively. We measured a bonding-energy difference of ~ 30 meV between X^o and T that agrees with previous reports. [30] In addition to X^o and T emissions, we identify a spectrally asymmetric emission line at longer wavelengths that can be deconvoluted into multiple Gaussian lineshapes with emission energies ~ 0.15-0.2 eV below the X^o energy. We attribute these emission bands to the radiative recombination of excitons trapped by defect states in exfoliated $MoSe_2$ monolayers, and we refer to them as defect-trapped excitonic emissions (X^d). Such an assignment matches previous experimental observations and theoretical predictions based on DFT calculations, [29] which suggest the formation of defect-induced mid-gap states ~ 0.2-0.3 eV away from the edge of the conduction/valance band in $MoSe_2$ films. In Figure 2-7(b), we further verified the nature of the X^d emission *via* monitoring its integrated PL intensity as the power of the excitation laser changes. Since the X^d emission stems from defect-mediated radiative recombination, its emission intensity is expected to saturate at high excitation powers after defect states are fully populated with free excitons. Our experiments confirm this expectation as the emission intensity of X^d displays a sub-linear dependence on the excitation power, manifesting the saturation of the PL intensity at high excitation powers. In contrast, X^o and T emission bands follow linear trends with no sign of saturation within the measured range of excitation powers.

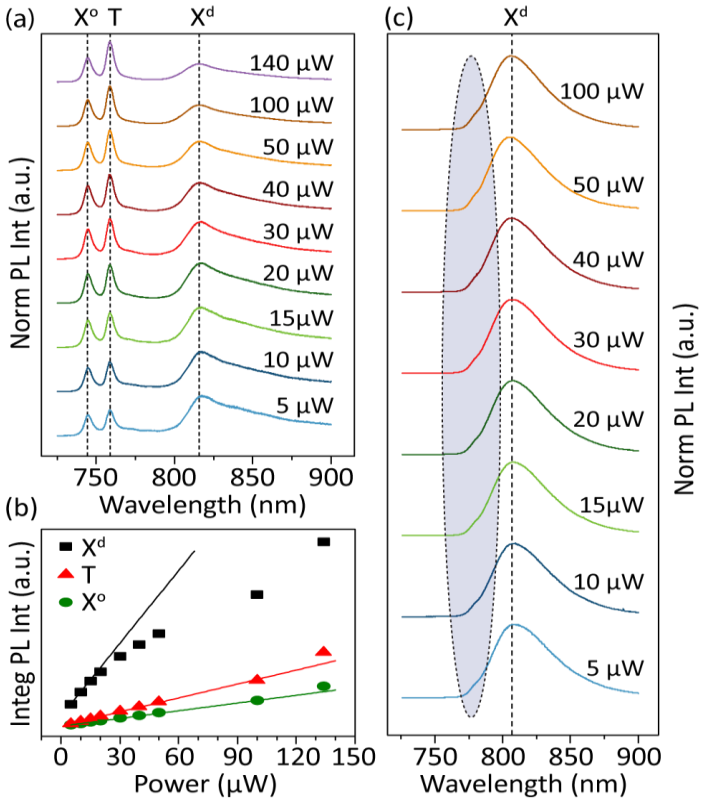

Figure 2-7: Low-temperature (~ 4K) PL spectroscopy of defects in $MoSe_2$ monolayers. (a) PL spectra obtained from a representative exfoliated $MoSe_2$ sample. Excitation powers are marked on the spectra. Three emission lines marked on the spectra associate with neutral excitons (X^o), trions (T), and defect-trapped excitons (X^d). (b) The integrated PL intensities of X^o and T emissions demonstrate linear dependence on the excitation power, while a sub-linear trend governs the behavior of the X^d emission. (c) PL spectra obtained from a representative CVD-grown $MoSe_2$ sample. Excitation powers are marked on the spectra. The defect-assisted emission dominates the PL spectra of CVD-grown samples, and X^o and T emissions only appear as weak peaks on the shoulder of the X^d emission. The shaded region highlights the approximate locations of X^o and T peaks.

In comparison to exfoliated $MoSe_2$ crystals, CVD-grown crystals display strikingly different low-temperature PL spectra (Figure 2-7(c)). In fact, in CVD-grown samples, the defect-mediated emission (*i.e.*, X^d) overwhelms the entire PL spectrum, and the emissions of free excitons/trions only appears as weak peaks on the short-wavelength shoulder of the broad X^d band, as highlighted by the shaded oval in Figure 2-7(c). In addition, within our accessible range of the excitation power, we did not observe any saturation in the emission

intensity at the X^d band of CVD-grown films. These collective observations suggest that the density of point defects in CVD-grown $MoSe_2$ monolayers is significantly larger than that in exfoliated $MoSe_2$ monolayers.

To further study native point defects, we performed STEM imaging on CVD-grown (Figure 2-8(a)) and exfoliated (Figure 2-8(b)) $MoSe_2$ monolayers. Here, we rely on the image-intensity variation at atomic sites (Figure 2-8(c)) to identify the type and areal density of defects in the examined monolayers. In STEM, the image intensity at a specific site is proportional to the atomic number (Z) as well as the number of atoms occupying the site. Thus, in a monolayer $MoSe_2$ film, chalcogen sites with two Se atoms (Z = 34) appear slightly brighter than metal sites with only one Mo atom (Z = 42). Accordingly, through the intensity mapping across atomic lines (*e.g.*, Figure 2-8(c), left panel), we can distinguish the chalcogen sub-lattice from the metal sublattice and readily build the 2D lattice of $MoSe_2$. Using this approach, lattice distortions or defects can be immediately identified through a deviation from the benchmark intensity profile. For instance, as the middle panel of Figure 2-8(c) represents, the intensity at a single Se-vacancy (V_{Se}) is approximately half of the intensity at a chalcogen site that is occupied by two Se atoms, and the intensity at a double-Se vacancy (V_{2Se}) drops to the background level because there is no Se atom at such atomic sites. Using this criterion, we analyzed STEM images and concluded that the V_{Se} vacancy is the dominant defect type in both CVD-grown and exfoliated $MoSe_2$ films. In addition to V_{Se} vacancies, CVD-grown $MoSe_2$ films also host V_{2Se} vacancies at a relatively lower density. We note that our CVD-grown and exfoliated films did not host any extended defects such as mirror twin boundaries that are frequently observed in films grown by molecular-beam epitaxy. [31]

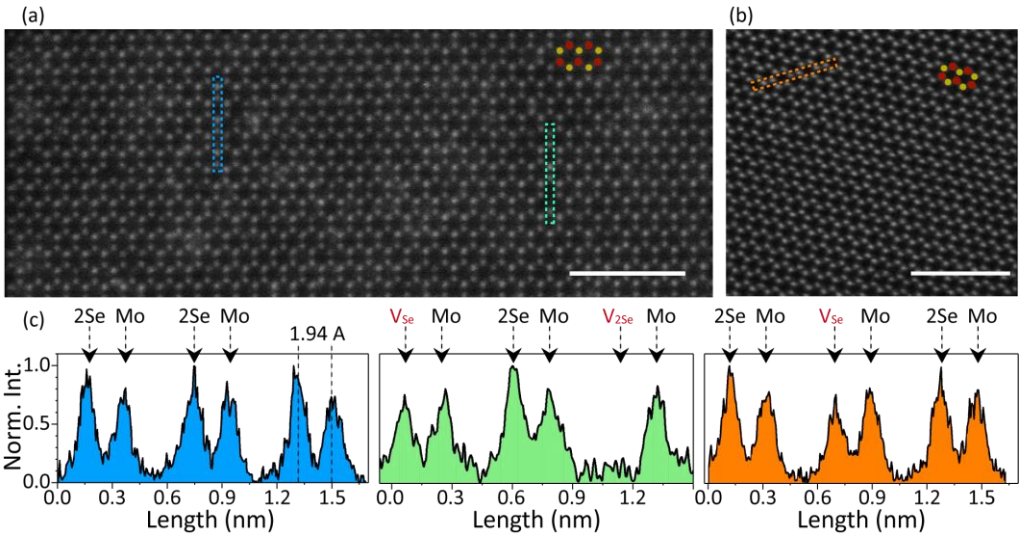

Figure 2-8: STEM analysis of Se vacancies. (a, b) High-resolution STEM images of representative CVD-grown and exfoliated $MoSe_2$ monolayers, respectively. Red and yellow circles mark Mo and Se_2 atomic sites, respectively. (c) Intensity profiles across the atomic lines highlighted in (a) and (b). Identical color codes are used in panels (a-c). Using the intensity profile (left profile), the Mo sub-lattice can be distinguished from the Se_2 sub-lattice (Mo-Se_2 distance: ~ 1.94 Å). Accordingly, deviation from the reference intensities is used to identify vacancies on CVD-grown (middle profile) and exfoliated (right profile) $MoSe_2$ samples. Scale bars represent 2 nm.

Using the above approach, we can count the number of V_{Se} and V_{2Se} vacancies across an imaged area and estimate the areal density of vacancies in CVD-grown and exfoliated films. Inspecting several samples from each $MoSe_2$ type revealed that the average density of V_{Se} vacancies in CVD-grown and exfoliated films are ~ 1.23×10^6 μm^{-2} and ~ 0.42×10^6 μm^{-2}, respectively. We also estimated the density of V_{2Se} vacancies in CVD-grown monolayers to be ~ 0.11×10^6 μm^{-2}. These areal vacancy densities translate into 7.83% and 2.17% Se deficiencies in CVD-grown and exfoliated monolayers, respectively, showing that the Se deficiency in CVD-grown films is more than three times larger than that in exfoliated monolayers. Since our alloying approach relies on replacing Se atoms by S atoms, the unoccupied Se sites (*i.e.*, Se vacancies) in starting $MoSe_2$ crystals may serve as atomic sites from which S atoms enter the $MoSe_2$ lattice. Thus, we speculate that the presence of Se vacancies lowers the barrier for the chalcogen substitution, facilitating the

alloying process. Accordingly, the sulfurization of CVD-grown $MoSe_2$ films with abundant Se vacancies results in $MoS_{2x}Se_{2(1-x)}$ alloys with x values larger than that in exfoliated samples with fewer native Se vacancies.

To obtain further insight into the vacancy-mediated alloying mechanism, we performed density-functional theory (DFT) calculations. In our DFT studies, we consider that S atoms enter the host lattice of $MoSe_2$ *via* occupying the pre-existing vacancy sites, meaning that vacancies serve as niches from which the alloying process initiates and further spreads throughout the lattice. However, since the Se deficiency in host $MoSe_2$ monolayers is limited to 7.83%, a sustainable vacancy-mediated alloying process needs an excess generation of Se vacancies after the pre-existing vacancies are infiltrated by S atoms. Our calculations show that the energy barrier for the generation of Se vacancies is larger than the provided thermal energy (*i.e.*, $(KT)_{max} \approx 0.12$ eV @ 950 ^{o}C) during our high-temperature alloying processes, suggesting that the thermal desorption of Se atoms is unlikely. Instead, our DFT calculations suggest that the infiltration of pre-existing vacancies by S atoms might release enough energy to overcome the energy barrier for producing additional Se vacancies in nearby sites. Therefore, a steady chalcogen substitution can be sustained beyond the density of pre-existing vacancies.

As demonstrated in PL maps (Figure 2-1(g) and Figure 2-6(d)), our sulfurization process yields $MoS_{2x}Se_{2(1-x)}$ alloys with spatially uniform compositions across the whole plane of the 2D material, suggesting that a diffusion process assists the uniform distribution of S atoms within the plane of host $MoSe_2$ monolayers. To computationally study this phenomenon, we considered a two-step process in which a sulfur binds to a Se-vacancy site and then diffuses throughout the layer *via* exchanging position with Se vacancies. To

estimate an energy barrier for this process, we performed nudged elastic band (NEB) calculations using DFT calculations (see Methods for computational details). In a 4-formula unit (f.u.) cell of monolayer $MoSe_2$, we replace one Se atom with one S atom, and removed a neighboring Se atom to create the vacancy to form Mo_4Se_6S. The computation of the diffusion barrier involves four intermediate NEB steps in the exchange of the Se vacancy and S atom positions, as shown in Figure 2-9(a). We compute a 1.75 eV NEB barrier for this process, as shown in Figure 6(b). Using this barrier, we can compute a temperature-dependent sulfur hopping rate (*i.e.*, ϑ) assuming an Arrhenius behavior; $\vartheta = \vartheta_0 \exp(-\Delta E/K_B T)$, where we take ϑ_0 = 3 THz, and ΔE = 1.75 eV is the barrier height obtained from the NEB calculations (*i.e.*, Figure 2-9(b)). In this equation, K_B and T represent the Boltzmann constant and temperature, respectively. The plot of the temperature dependence of the hopping rate is shown in Figure 2-9(c). At temperatures around 1000 K, close to our experimental condition, the hopping rate is approximately 4000 hops/second. Thus, considering the typical S-Se vacancy distance of 3 Å and assuming a random walk diffusion, annealing at 1000 K leads to less than 20nm/sec lateral diffusion within the plane of the host $MoSe_2$ lattice. This estimation indicates that S atoms could be diffusing through the crystal, but the diffusion length is not long enough to allow for the widespread sulfurization from a single vacancy site. Thus, a higher vacancy concentration throughout the sample could enhance the incorporation of S into Se vacancy sites and then subsequent diffusion of S atoms, leading to the nearly complete sulfurization of the sample at elevated temperatures.

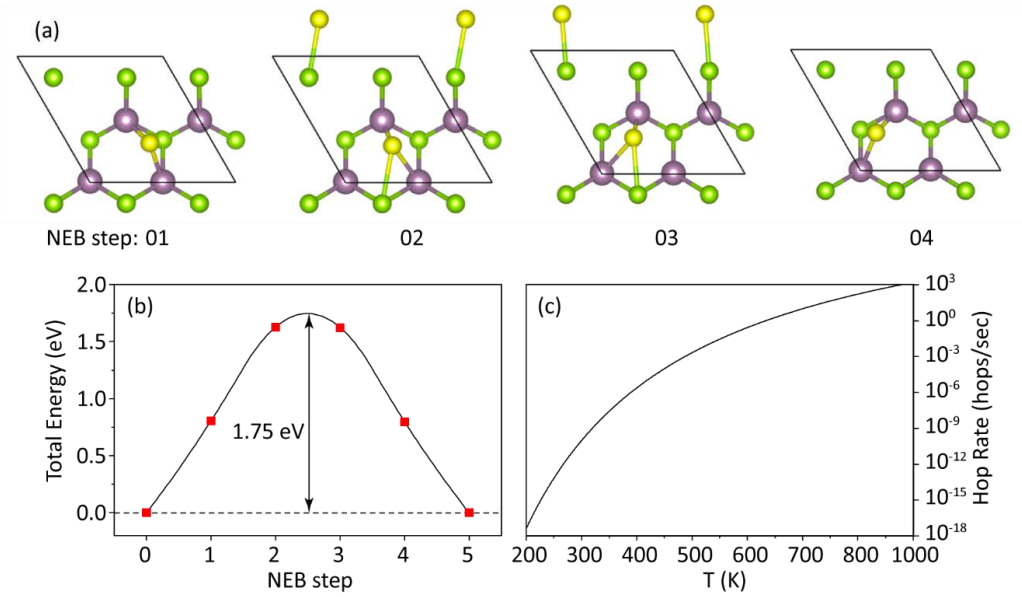

Figure 2-9: DFT calculation of the vacancy-mediated diffusion. (a) The top view of four intermediate stages used in the NEB calculation of a S atom exchanging places with a Se vacancy. In the 4-formula unit cell of $MoSe_2$, we replace one Se atom by S and remove a neighboring Se atom to create the vacancy to form Mo_4Se_6S. Purple, green, and yellow colors represent Mo, Se, and S, respectively. (b) The NEB energy barrier computed for the exchange of a S atom with a Se vacancy, as shown in the path illustrated in panel (a). Symbols represent computed values, and the line represents a quadratic fit to data points. (c) The temperature-dependent hopping rate computed using the 1.75 eV barrier height shown in panel (b).

I note that, in addition to Se vacancies, other types of defects such as edge sites (in both CVD-grown and exfoliated films) and nano-scale pinholes (mostly in CVD-grown samples) may also serve as alternative channels for the incorporation of S atoms into the $MoSe_2$ lattice. However, considering the short diffusion length of S atoms, we believe that such alternative channels play secondary roles in the alloying process. In fact, S atoms that enter the host $MoSe_2$ lattice *via* the edge sites can diffuse to only a short distance from the edges. Thus, the role of edge sites is restricted to a confined region close to the periphery of relatively large $MoSe_2$ films. Similarly, nano-scale pinholes appear at a very low density with a sparse distribution, implying that only a small fraction of the large $MoSe_2$ plane can be affected by the S atoms that enter the lattice through the pinholes. Therefore, we believe

that the randomly distributed Se vacancies are dominant sites for the incorporation of S atoms into the $MoSe_2$ lattice. In addition, because of the dense distribution of vacancies, the typical inter-vacancy distance is shorter than the estimated diffusion length, which enables the uniform alloying of the entire $MoSe_2$ plane through Se vacancies.

I also note that all periodic DFT calculations were performed with the Vienna *Ab-initio* Simulation Package (VASP) version 5.3.5. The calculations use the projector augmented-wave method, [32] and the electron exchange-correlation interaction was treated by the generalized gradient approximation (GGA) functional of Perdew, Burke, and Ernzerhof (PBE). A kinetic energy cutoff of 600 eV for the plane-wave basis set was used for structure relaxations. All atomic structures and in-plane lattice constants were relaxed using the conjugate gradient algorithm. The convergence thresholds for ionic and electronic relaxations were 10^{-5} eV per a 4 f.u. cell. The NEB calculations used 4 intermediate images with an energy cutoff of 400 eV. The initial and final NEB images were taken from relaxed structures. All calculations used an 8×8×1 Monkhorst-Pack k-mesh centered around k = Γ = (0, 0, 0). The unit cells all used a minimum of 15 Å of vacuum space to prevent interaction between periodic cell repeats, as well as a Gaussian electronic energy distribution smearing.

I also note that the ϑ_0 = 3 THz parameter is related to the vibrational frequency along the diffusion path. Because of the complex framework of our experiments at atomic scales, obtaining an accurate value for ϑ_0 is very difficult. However, the vibrational modes of alloys monitored by the Raman spectroscopy can provide a reasonable estimate about this value. In this regard, since the diffusion of vacancies occurs within the plane of the 2D material, we considered “in-plane” vibrational modes to obtain an estimated value.

2.4 References

1. Lu, X.; Utama, M. I. B.; Lin, J. H.; Gong, X.; Zhang, J.; Zhao, Y. Y.; Pantelides, S. T.; Wang, J. X.; Dong, Z. L.; Liu, Z.; Zhou, W.; Xiong, Q. H. Large-Area Synthesis of Monolayer and Few-Layer $MoSe_2$ Films on SiO_2 Substrates. *Nano Lett* **2014**, 14, 2419-2425.
2. Taghinejad, H.; Eftekhar, A. A.; Campbell, P. M.; Beatty, B.; Taghinejad, M.; Zhou, Y.; Perini, C. J.; Moradinejad, H.; Henderson, W. E.; Woods, E. V.; Zhang, Z.; Ajayan, P. M.; Reed, E. J.; Vogel, E. M.; Adibi, A. Strain Relaxation *via* Formation of Cracks in Compositionally Modulated Two-Dimensional Semiconductor Alloys. *Npj 2D Mater Appl* **2018**, 2, 1-8.
3. Liu, H. J.; Zheng, H.; Yang, F.; Jiao, L.; Chen, J. L.; Ho, W. K.; Gao, C. L.; Jia, J. F.; Xie, M. H. Line and Point Defects in $MoSe_2$ Bilayer Studied by Scanning Tunneling Microscopy and Spectroscopy. *ACS Nano* **2015**, 9, 6619-6625.
4. Zhou, W.; Zou, X. L.; Najmaei, S.; Liu, Z.; Shi, Y. M.; Kong, J.; Lou, J.; Ajayan, P. M.; Yakobson, B. I.; Idrobo, J. C. Intrinsic Structural Defects in Monolayer Molybdenum Disulfide. *Nano Lett* **2013**, 13, 2615-2622.
5. Hong, J. H.; Hu, Z. X.; Probert, M.; Li, K.; Lv, D. H.; Yang, X. N.; Gu, L.; Mao, N. N.; Feng, Q. L.; Xie, L. M.; Zhang, J.; Wu, D. Z.; Zhang, Z. Y.; Jin, C. H.; Ji, W.; Zhang, X. X.; Yuan, J.; Zhang, Z. Exploring Atomic Defects in Molybdenum Disulphide Monolayers. *Nat Commun* **2015**, 6, 6293.
6. Lu, C. P.; Li, G. H.; Mao, J. H.; Wang, L. M.; Andrei, E. Y. Bandgap, Mid-Gap States, and Gating Effects in MoS_2. *Nano Lett* **2014**, 14, 4628-4633.
7. Wang, X.; Gong, Y.; Shi, G.; Chow, W. L.; Keyshar, K.; Ye, G.; Vajtai, R.; Lou, J.; Liu, Z.; Ringe, E.; Tay, B. K.; Ajayan P. M. Chemical Vapor Deposition Growth of Crystalline Monolayer $MoSe_2$. *ACS Nano* **2014**, 8, 5125-5131.
8. Ozden, A.; Ay, F.; Sevik, C.; Perkgoz, N. K. CVD Growth of Monolayer MoS_2: Role of Growth Zone Configuration and Precursors Ratio. *Jpn J Appl Phys* **2017**, 56, 06GG05.
9. Zhu, D. C.; Shu, H. B.; Jiang, F.; Lv, D. H.; Asokan, V.; Omar, O.; Yuan, J.; Zhang, Z.; Jin, C. H. Capture the Growth Kinetics of CVD Growth of Two Dimensional MoS_2. *Npj 2D Mater Appl* **2017**, 1, 1-8.
10. Feng, Q.; Zhu, Y.; Hong, J.; Zhang, M.; Duan, W.; Mao, N.; Wu, J.; Xu, H.; Dong, F.; Lin, F.; Jin, C.; Wang, C.; Zhang, J.; Xie, L. Growth of Large-Area 2D $MoS_{(2)((1)-x)}Se_{(2)x}$ Semiconductor Alloys. *Adv Mater* **2014**, 26, 2648-2653.
11. Gong, C.; Huang, C. M.; Miller, J.; Cheng, L. X.; Hao, Y. F.; Cobden, D.; Kim, J.; Ruoff, R. S.; Wallace, R. M.; Cho, K.; Xu, X. D.; Chabal, Y. J. Metal Contacts on Physical Vapor Deposited Monolayer MoS_2. *ACS Nano* **2013**, 7, 11350-11357.
12. Taghinejad, H.; Taghinejad, M.; Tarasov, A.; Tsai, M. Y.; Hosseinnia, A. H.; Moradinejad, H.; Campbell, P. M.; Eftekhar, A. A.; Vogel, E. M.; Adibi, A. Resonant Light-Induced Heating in Hybrid Cavity-Coupled 2D Transition-Metal Dichalcogenides. *ACS Photonics* **2016**, 3, 700-707.
13. Li, H.; Wu, J. M. T.; Yin, Z. Y.; Zhang, H. Preparation and Applications of Mechanically Exfoliated Single-Layer and Multi-Layer MoS_2 and WSe_2 Nanosheets. *Acc Chem Res* **2014**, 47, 1067-1075.

14. Ottaviano, L.; Palleschi, S.; Perrozzi, F.; D'Olimpio, G.; Priante, F.; Donarelli, M.; Benassi, P.; Nardone, M.; Gonchigsuren, M.; Gombosuren, M.; Lucia, A.; Moccia, G.; Cacioppo, O. A. Mechanical Exfoliation and Layer Number Identification of MoS_2 Revisited. *2D Mater* **2017**, 4, 1.
15. Komsa, H. P.; Krasheninnikov, A. V. Native Defects in Bulk and Monolayer MoS_2 From First Principles. *Phys Rev B* **2015**, 91, 125304.
16. Li, X. F.; Puretzky, A. A.; Sang, X. H.; Santosh, K. C.; Tian, M. K.; Ceballos, F.; Mahjouri-Samani, M.; Wang, K.; Unocic, R. R.; Zhao, H.; Duscher, G.; Cooper, V. R.; Rouleau, C. M.; Geohegan, D. B.; Xiao, K. Suppression of Defects and Deep Levels Using Isoelectronic Tungsten Substitution in Monolayer $MoSe_2$. *Adv Funct Mater* **2017**, 27, 1603850.
17. Mahjouri-Samani, M.; Liang, L. B.; Oyedele, A.; Kim, Y. S.; Tian, M. K.; Cross, N.; Wang, K.; Lin, M. W.; Boulesbaa, A.; Rouleau, C. M.; Puretzky, A. A.; Xiao, K.; Yoon, M.; Eres, G.; Duscher, G.; Sumpter, B. G.; Geohegan, D. B. Tailoring Vacancies Far Beyond Intrinsic Levels Changes the Carrier Type and Optical Response in Monolayer $MoSe_{2-x}$ Crystals. *Nano Lett* **2016**, 16, 5213.
18. Wu, Z. T.; Luo, Z. Z.; Shen, Y. T.; Zhao, W. W.; Wang, W. H.; Nan, H. Y.; Guo, X. T.; Sun, L. T. L. T.; Wang, X. R.; You, Y. M.; Ni, Z. H. Defects as a Factor Limiting Carrier Mobility in WSe_2: a Spectroscopic Investigation. *Nano. Res.* **2016**, 9, 3622.
19. Yu, Z. H.; Pan, Y. M.; Shen, Y. T.; Wang, Z. L.; Ong, Z. Y.; Xu, T.; Xin, R.; Pan, L. J.; Wang, B. G.; Sun, L. T. L. T.; Wang, J. L.; Zhang, G.; Zhang, Y. W. ; Shi, Y.; Wang, X. R. Towards Intrinsic Charge Transport in monolayer molybdenum disulfide by defect and interface engineering. *Nat. Commun.* **2014**, 5, 5290.
20. Wu, Z. T.; Zhao, W. W.; Jiang, J.; Zheng, T.; You, Y. M.; Lu, J. P.; Ni, Z. H. Defect Activated Photoluminescence in WSe_2 Monolayer. *J Phys Chem C* **2017**, 121, 12294-12299.
21. Li, M. L.; Wan, Y. L.; Wang, W. D. Prediction of Mechanical Properties for Defective Monolayer MoS_2 with Single Molybdenum Vacancy Defects Using Molecular Dynamics Simulations. *IEEE Conf Nanotechnol* **2017**, 9-12.
22. Li, M. L.; Wan, Y. L.; Tu, L. P.; Yang, Y. C.; Lou, J. The Effect of V_{MoS3} Point Defect on the Elastic Properties of Monolayer MoS_2 with REBO Potentials. *Nanoscale Res Lett* **2016**, 11, 1.
23. Shu, H. B.; Zhou, D.; Li, F.; Cao, D.; Chen, X. S. Defect Engineering in $MoSe_2$ for the Hydrogen Evolution Reaction: From Point Defects to Edges. *ACS Appl Mater Interfaces* **2017**, 9, 42688.
24. Srivastava, A.; Sidler, M.; Allain, A. V.; Lembke, D. S.; Kis, A. A.; Imamoglu, A. Optically Active Quantum Dots in Monolayer WSe_2. *Nat Nanotechnol* **2015**, 10, 491-496.
25. Huang, B.; Yoon, M.; Sumpter, B. G.; Wei, S. H.; Liu, F. Alloy Engineering of Defect Properties in Semiconductors: Suppression of Deep Levels in Transition-Metal Dichalcogenides. *Phys Rev Lett* **2015**,115, 126806-1.
26. Mahjouri-Samani, M.; Lin, M. W.; Wang, K.; Lupini, A. R.; Lee, J.; Basile, L.; Boulesbaa, A.; Rouleau, C. M.; Puretzky, A. A.; Ivanov, I. N.; Xiao, K.; Yoon, M.; Geohegan, D. B. Patterned Arrays of Lateral Heterojunctions Within Monolayer Two-Dimensional Semiconductors. *Nat Commun* **2015**, 6, 7749.
27. Su, S. H.; Hsu, W. T.; Hsu, C. L.; Chen, C. H.; Chiu, M. H.; Lin, Y. C.; Chang, W. H.; Suenaga, K.; He, J. H.; Li, L. J. Controllable Synthesis of Band-Gap-Tunable and

Monolayer Transition-Metal Dichalcogenide Alloys, *Frontiers in Energy Research* **2014**, 2, 1.
28. Tongay, S.; Suh, J.; Ataca, C.; Fan, W.; Luce, A.; Kang, J. S.; Liu, J.; Ko, C.; Raghunathanan, R.; Zhou, J.; Ogletree, F.; Li, J. B.; Grossman, J. C.; Wu, J. Q. Defects Activated Photoluminescence in Two-Dimensional Semiconductors: Interplay Between Bound, Charged, and Free Excitons. *Sci Rep* **2013**, 3, 2657.
29. Surrente, A.; Dumcenco, D.; Yang, Z.; Kuc, A.; Jing, Y.; Heine, T.; Kung, Y. C.; Maude, D. K.; Kis, A.; Plochocka, P. Defect Healing and Charge Transfer-Mediated Valley Polarization in $MoS_2/MoSe_2/MoS_2$ Trilayer van der Waals Heterostructures. *Nano Lett* **2017**, 17, 4130-4136.
30. Lehtinen, O.; Komsa, H. P.; Pulkin, A.; Whitwick, M. B.; Chen, M. W.; Lehnert, T.; Mohn, M. J.; Yazyev, O. V.; Kis, A.; Kaiser, U.; Krasheninnikov, A. V. Atomic Scale Microstructure and Properties of Se-Deficient Two-Dimensional $MoSe_2$. *ACS Nano* **2015**, 9, 3274–3283.
31. Blochl, P. E. Projector Augmented-Wave Method. *Phys Rev B* **1994**, 50, 17953.
32. Perdew, J. P.; Burke, K.; Ernzerhof, M. Generalized Gradient Approximation Made Simple. *Phys Rev Lett* **1996**, 77, 3865.

CHAPTER 3. ALLOYING-INDUCED STRAIN: ORIGIN AND STRUCTURAL IMAPCT

Phenomenologically, the optoelectronic properties of alloys are entangled with a strain that is intrinsic to synthesis processes. In this chapter, I discuss the formation of an unprecedented biaxial strain that stems from the chalcogen substitution in monolayer TMD alloys, inflicting in-plane fractures within the plane of yielded monolayer crystals. We find that the starting crystal ($MoSe_2$) fails to adjust its lattice constant as the chalcogen atoms of the host crystal (i.e., Se) are replaced by foreign atoms (i.e., S) during the post-growth alloying process. Thus, the resulting alloy forms a stretched lattice and experiences a large biaxial tensile strain. Our experiments show that the biaxial strain relaxes via the formation of cracks in interior crystal domains or through less constraint bounds at the edges of monolayer alloys. Griffith's criterion suggests that the existence of defects combined with a sulfur-rich environment have the potential to significantly lower the critical strain level at which cracking occurs. Our calculations demonstrate a substantial reduction in the fracture-inducing critical strain from 11% (in standard TMD crystals) to a range below 4% in as-synthesized alloys.

3.1 Structural Fracture of $MoS_{2x}Se_{2(1-x)}$ Alloys

To gain more insight into the structural properties of the sulfurized 2D films, we studied the morphology of alloys using scanning electron microscopy (SEM). We first start with alloys with $x \approx 1$, that is MoS_2 films synthesized from the full substitution of Se atoms by S atoms in starting monolayer $MoSe_2$ films. As shown in Figure 3-1, we simultaneously

identify three types of morphologies across the samples: (i) entirely continuous (Figure 3-1(a)-(c)), (ii) entirely cracked (Figure 3-1(d)-(f)), and (iii) partially cracked (Figure 3-1(g)-(i)) films. The SEM inspection of multiple independently converted samples consistently confirms that more than ~ 90% of converted MoS_2 monolayers are entirely cracked and the rest are mostly continuous, with only a few partially cracked flakes on each sample. It is worth noting that prior to the conversion step, the pristine $MoSe_2$ crystals are all continuous and cracks form only after the sulfurization process.

We believe that the observed cracks stem from an induced strain that might originate from two sources: (i) the substitution of Se atoms by S atoms, and/or (ii) the thermal-expansion-coefficient mismatch between 2D materials and the underlying SiO_2 substrate. To distinguish between these two sources, we repeated our standard conversion process with no sulfur load so that monolayer crystals experience similar thermal treatment while no composition change occurs. In this experiment, to account for the state of the monolayer crystal at the beginning ($MoSe_2$) and the end (MoS_2) of the conversion process, we simultaneously anneal CVD-grown monolayer $MoSe_2$ and MoS_2 samples. Our SEM inspections did not show any formation of cracks in the as-treated samples. Therefore, we conclude that the mismatch of thermal-expansion coefficients does not play a primary role, and the composition-modulation event governs the formation of cracks. However, analogous to previous reports, [1, 2] we observed that high-temperature annealing generates rather straight corrosion lines at the boundaries of crystal domains, some of which are marked by arrows in Figure 3-1. Such corrosion lines should not be mistaken for cracks that form within individual crystal domains and span over significantly shorter ranges.

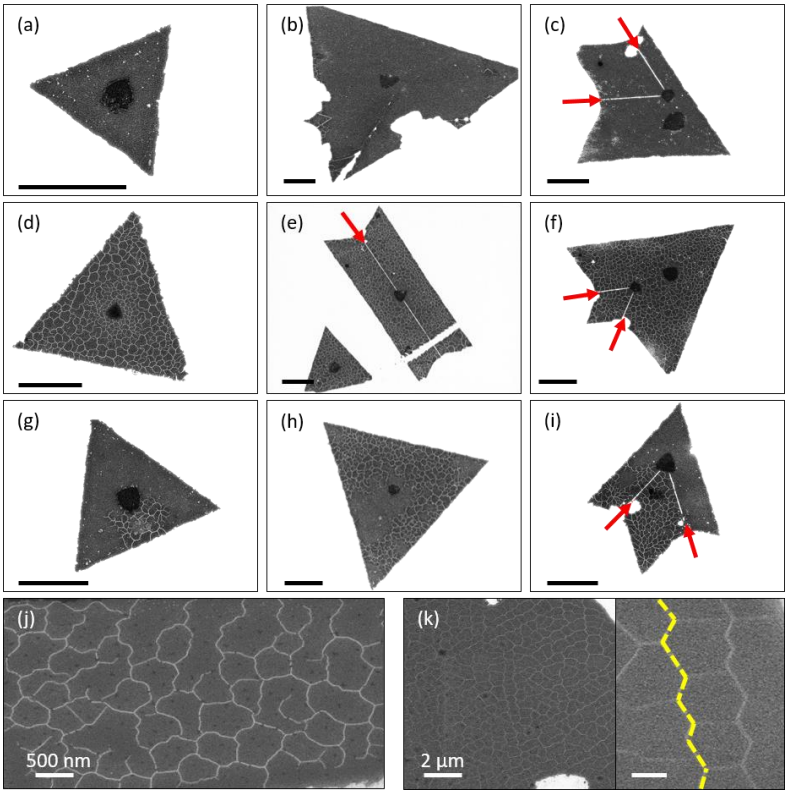

Figure 3-1: Crack formation in sulfurized films. SEM inspection identifies three different types of morphologies: (a-c) entirely continuous, (d-f) entirely cracked, and (g-i) partially cracked flakes. All the SEM images are collected from one sample after full conversion of the $MoSe_2$ monolayer crystals to MoS_2. Arrows point to the corrosion lines along the boundaries of the crystal domains. The effect of the conversion degree (i.e., 'x' in $MoS_{2x}Se_{2(1-x)}$) is elaborated via comparing the crack propagation path in (j) a fully converted $MoSe_2$ crystal (i.e., $x \approx 1$) and in (k) a partially converted film (with $x \approx 0.5$). The inset of panel (k) highlights the zigzag path as the most energetically favorable direction for crack propagation in partially converted sample. Scale bars in (j), (k), and the inset of pane (k) are 500 nm, 2 µm, and 300 nm, respectively.

To further confirm the dominant role of chalcogen substitution in cracking of $MoS_{2x}Se_{2(1-x)}$ alloys, we cover parts of the starting $MoSe_2$ films with a 50 nm-thick SiO_2 film and then repeat our sulfurization process using these samples. The SEM images of the as-prepared samples "after" the sulfurization process (950 ^{o}C for 15 mins) is presented in Figure 3-2. Interestingly, this experiment proves that the cracking is restricted to the unprotected regions, where the alloying occurs, while the protected regions underneath the SiO_2 layers remain seamless and free of cracks. This observation clearly verifies that

alloying-induced strain is the source of the crack formation and competing mechanisms such as interfacial strain at the MoS_2-$MoSe_2$ interface and or thermal-expansion-coefficient mismatch are not playing primary roles. A similar conclusion can be obtained in periodically patterned samples as shown in Figure 3-2(b) and (c).

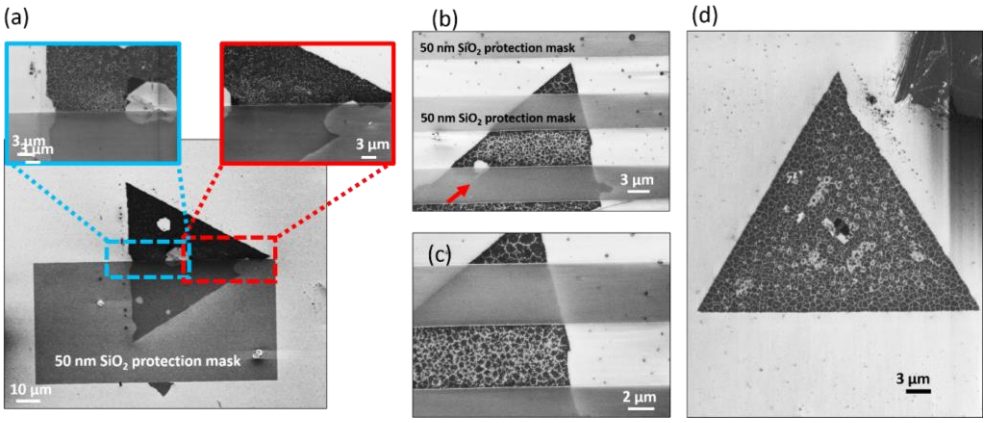

Figure 3-2: Cracking in pattered structures. (a) The SEM image of a triangular film, which its lower half is protected with 50 nm SiO_2. As shown in the inset images, cracks only form in the unprotected regions, where the alloying occurs. (b) Similar observation is made via periodic construction of the SiO_2 protection mask, which verifies the results observed in (a). (c) A closer look at the sample shown in (b). (d) The SEM image of a cracked 2D material covered with a 50 nm SiO_2 layer. Observation of the cracks in this sample shows that 50 nm SiO_2 film is transparent under the SEM microscope.

It is important to note that the 50 nm-thick SiO_2 protecting layer is transparent under the SEM microscope as the extent of the 2D material (e.g., insets of Figure 3-2(a)) or pre-existing scratches in 2D materials (e.g., the arrow in Figure 3-2(b)) are completely observable through the SiO_2 protecting film. However, to further confirm the transparency of the 50 nm-thick SiO_2 film, we first convert a $MoSe_2$ film into MoS_2 using a sulfurization step and then cover the sample with a 50 nm SiO_2 film. The obtained SEM images of the such a sample (Figure 3-2(d)) clearly shows that the cracks can be seen through the SiO_2 layer, which explicitly proves the transparency of the SiO_2 layer. Therefore, the observation

of seamless regions under SiO_2 in Figure 3-2(a)-(c) is not an artifact of the SiO_2 layer blocking the details of 2D material underneath it.

Examination of sulfurized samples reveals an important trend: cracks consistently branch out of Y-shaped (triple) junctions or from the edge of monolayer crystals (e.g., see Figure 3-1(d)). This observation suggests the existence of specific crack nucleation sites and preferential crystallographic directions over which cracks spread within the plane of monolayer crystals. Given that the origin of the strain is composition conversion, we think that unsaturated bonds (at the edges) or defect sites (within the interior domains of the film) serve as local sites at which the incorporation of S atoms into the lattice of $MoSe_2$ is initiated. A similar contribution of defect sites in the formation of cracks and Y-shaped branching behavior has been recorded in TMD [3] films subjected to biaxial strain.

The propagation path of cracks between Y-shaped junctions carries valuable information regarding conversion-induced strain. In the determination of the crack propagation path, the spatial distribution of the strain field at the tip of a propagating crack is a key factor. In addition, the Van der Waals interaction of monolayer crystals with the substrate provides a medium for the strain fields of individual cracks to mutually interact, defining a net propagation path between the Y-shaped junctions. Theoretical modeling based on molecular dynamics [4] and classical fracture mechanics [3] are effective for the qualitative prediction of the crack propagation path in monolayer MoS_2 crystals under biaxial strain. In these models, the strain field is assumed to extend to a critical radius of (r_c) from the tip of the propagating cracks. As schematically shown in Figure 3-3, cracks propagate between two individual Y-shaped junctions via a curved or straight path if r_c is a large or small value, respectively. To change the r_c value, we change the relative strength

of the strain by means of varying the composition ratio, x, in $MoSe_{2x}S_{2(1-x)}$ alloys in which increasing x monotonically increases the biaxial strain. Thus, we prepare two sets of samples: (i) a fully converted crystal (Figure 3-1(j)) with x = 1 (i.e., large strain and large r_c) and (ii) a partially converted crystal (Figure 3-1(k)) with x ≈ 0.5 (i.e., small strain and small r_c). A comparison of the SEM images of these samples shows that our experimental observations match the theoretical modeling; that is, in the fully converted sample, cracks mostly propagate via curved paths while in the partially converted sample, cracks obtain straight propagation paths (Figure 3-1(k)). Furthermore, in the partially converted sample, cracks mostly form hexagonal domains and propagate along zigzag directions (the inset of Figure 3-1(k)). This observation is also in agreement with molecular dynamics predictions, which identify the zigzag direction as the most feasible propagation path with a minimum surface energy. [4] Therefore, the structural analysis solidifies our assumption about the primary role of the conversion process (i.e., substitution of Se atoms by S atoms) in the creation of the biaxial strain and the formation of cracks in compositionally modulated monolayer alloys.

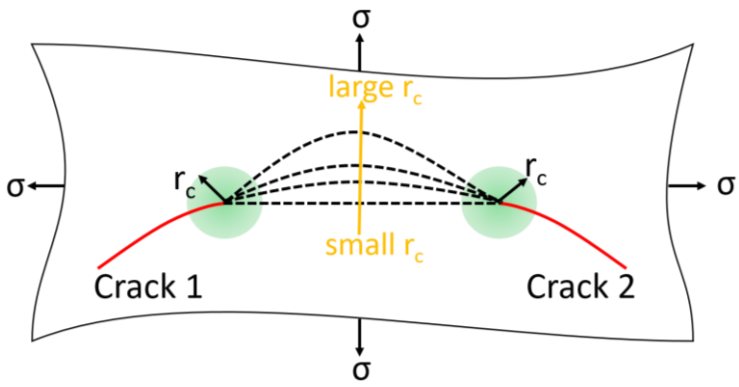

Figure 3-3: Prediction of the crack propagation path. Schematic representation shows the net propagation path upon interaction of two approaching cracks (i.e., cracks 1 & 2). Details of this modelling can be found in Ref. [5]. The strain field is assumed to extend to a distance r_c from the tip of an individual crack. Upon increasing r_c, the resulting pathway changes from a straight line to a curved one.

3.2 Quantitative Analysis of Alloying-Induced Strain

To quantitatively study the alloying-induced strain in sulfurized samples, we carry out PL spectroscopy, in which probing the optical bandgap provides direct information about the type (tensile/compressive) and the strength of the strain. [6-9] To magnify the the effect, we used a $MoS_{2x}Se_{2(1-x)}$ alloy with $x \approx 1$, that is a "converted" MoS_2 film in which the highest strain level is anticipated. In addition, we focus on partially cracked flakes (Figure 3-4(a), (b)) in which a direct comparison between the emission spectra of cracked and continuous regions is possible within a single film. Mapping the emission energy at the maximum PL intensity (Figure 3-4(c)) indicates that compared to cracked regions, the continuous (i.e., crack-free) regions emit light at lower energies. We also observe a significant drop in the intensity of the light emission in continuous regions (Figure 3-4(d)). These two distinctions can be concurrently observed in the representative PL spectra of cracked and continuous films as displayed in Figure 3-4(e).

Since the PL spectra of cracked regions match the standard emission spectrum of a pristine CVD-grown MoS_2 film, we denote the cracked regions as the strain-free parts. Accordingly, the reduction of the optical bandgap and the drop in the emission intensity are taken as indications of a biaxial tensile strain that acts on continuous regions. [9, 10] Thus, our study suggests that the formation of cracks in TMD alloys stems from a biaxial strain that is intrinsically linked to the chalcogen replacement during the sulfurization process. Indeed, the host $MoSe_2$ fails to adjust its lattice constant according to the composition of the alloy, leading to the development of a biaxial tensile strain in the alloy. Such strain results in the onset of fracture in monolayer alloys and further relaxes *via* the formation of cracks within the plane of the 2D material.

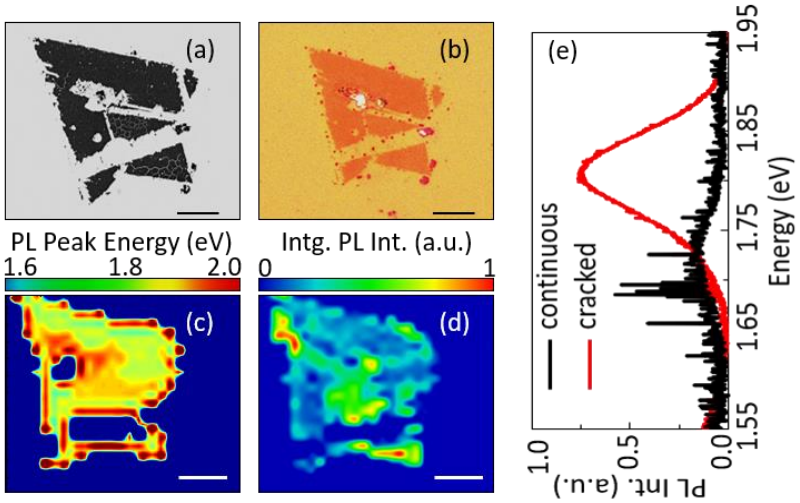

Figure 3-4: Strain relaxation via formation of cracks. (a) SEM and (b) optical images of a fully converted MoS_2 monolayer that is partially cracked. (c) Spatial mapping showing the PL energy at maximum PL intensity. The color bar depicts the energy span. (d) Spatial mapping of the PL intensity in which the continuous regions display low emission intensity. The normalized color bar represents the PL intensity integrated over 1.6-2.0 eV. (e) Representative PL spectra obtained from the cracked and continuous regions. Scale bars in (a)-(d) are 5 µm.

Several groups have investigated the effect of biaxial tensile strain on the MoS_2 bandgap, and a reduction of ~100 meV per one percent (%) of strain is the most commonly reported value. [9, 10] Therefore, the bandgap reduction of 120 $\pm$ 20 meV (extracted from Figure 3-4(c)) reflects a 1.2 $\pm$ 0.2 % biaxial tensile strain that acts on continuous regions. However, the expected scale of alloying-induced strain in $MoS_{2x}Se_{2(1-x)}$ monolayers is less than ~ 4% (see below for details), which is noticeably smaller than the reported 11% strain threshold for inducing fracture in TMD crystals. [11] Thus, cracking at such a small strain regime implies that the fracture strength of monolayer crystals is reduced by an extrinsic effect that seems to influence CVD-grown samples more than the exfoliated ones. Several studies have shown that crystal imperfections such as point defects (*i.e.*, atomic-scale defects), large defects (*e.g.*, pre-existing cracks), and grain boundaries significantly deteriorate the mechanical strength of 2D materials. [35-37] Among these types of defects,

large-scale defects and grain boundaries are shown to have the most deteriorating effect on various 2D materials including TMDs [14, 15] and graphene. [13] However, as we saw in Figure 3-1(d), the cracking phenomenon occurs in CVD-grown $MoSe_2$ samples with even only one crystallographic domain (*i.e.*, no grain boundaries). Such an observation suggests that pre-existing large-scale defects in the starting $MoSe_2$ films are the predominant factor in reducing the strength of 2D TMDs in our study.

To evaluate the role of pre-existing large-scale defects in the fracture of the as-synthesized $MoS_{2x}Se_{2(1-x)}$ alloys, we rely on the Griffith criterion. In this widely-used method, [15, 16] the critical strain, ε^c, (*i.e.*, strain at which the crystal fractures) is expressed in terms of the defect length ($2l$), the surface energy density (γ), and the Young's modulus of the 2D material (E); that is $\varepsilon^c = \sqrt{2\gamma/\pi \mathrm{E} l}$. On the other hand, alloying-induced strain ($\varepsilon(x)^{alloy}$) can be estimated from the mismatch between the lattice constant of the starting $MoSe_2$ film (a_{MoSe_2}) and that of the resulting $MoS_{2x}Se_{2(1-x)}$ alloy ($a(x)_{alloy}$), that is:

$$\varepsilon(x)^{alloy} = \frac{a_{MoSe_2} - a(x)_{alloy}}{a_{MoSe_2}} = x\,\frac{a_{MoSe_2} - a_{MoS_2}}{a_{MoSe_2}} \approx 0.039x \qquad (2)$$

Thus, if $\varepsilon(x)^{alloy}$ exceeds ε^c (*i.e.*, $\varepsilon(x)^{alloy} > \varepsilon^c$), the sulfurization process yields cracked $MoS_{2x}Se_{2(1-x)}$ crystals. This simple approach provides an estimate about the minimum length of defects sizes (*i.e.*, $2l_{min}$) in starting $MoSe_2$ films:

$$2l_{min} = \frac{4\gamma}{\pi E (0.039x)^2} \qquad (3)$$

Equations (2) and (3) are plotted as functions of x in Figure 3-5. Using Figure 3-5, we can estimate a minimum defect size (in starting $MoSe_2$ crystals) that causes the cracking of $MoS_{2x}Se_{2(1-x)}$ alloys under the alloying-induced strain of $\varepsilon(x)^{alloy}$. For example, the observation of cracks in $MoS_{2(0.45)}Se_{2(1-0.45)}$ (as in Figure 2-1(i)) indicates that the starting $MoSe_2$ film contained defects with sizes larger than $2l_{min} \approx 15$ nm, which caused the fracture of the alloy at a strain level as small as $\varepsilon(x = 0.45)^{alloy} \approx 1.75\%$.

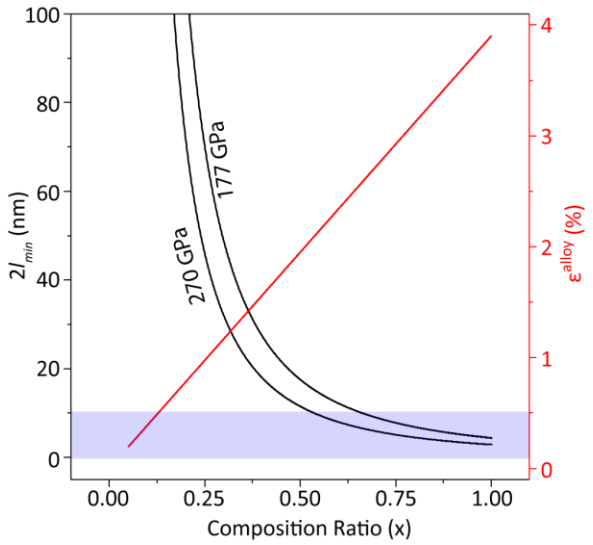

Figure 3-5: Estimating the defect size using the Griffith method. The alloying-induced strain (right axis, equation. (1)) and the minimum defect length (left axis, equation (2)) are plotted versus x. To estimate the length of defects (i.e., 2l), we used $\boldsymbol{\gamma}$ = 0.928 Joul/m^2 (see SI for details) and E = 177 GPa and 270 GPa, corresponding to the Young's moduli of $MoSe_2$ and MoS_2, respectively. These two values cover the full span of x ranging from 0 (i.e., $MoSe_2$) to 1 (i.e., MoS_2). The highlighted region marks 2l < 10 nm, over which the Griffith method overestimates the strength of a defective 2D material.

Following the insights provided by the Griffith method, we used the atomic-force microscopy (AFM) to inspect large-scale defects in several CVD-grown and exfoliated $MoSe_2$ films (Figure 3-6). Our analyses revealed that, unlike exfoliated films, CVD-grown $MoSe_2$ films contain large-scale defects with sizes typically ranging from several nanometers (nm) to ~ 100 nm. Based on Figure 3-5, such a span of the defect size can cause

cracking under alloying-induced strain values as small as ~ 0.8%, corresponding to $MoS_{2x}Se_{2(1-x)}$ alloys with composition ratios as small as x ≈ 0.2. Therefore, we conclude that the presence of large-scale defects in the form of pre-existing cracks in CVD-grown $MoSe_2$ films contributes to the formation of cracked alloys (*e.g.*, Figure 3-1), and the absence of such defects in exfoliated crystals yields seamless alloys without any cracks (*i.e.*, Figure 2-6). I note that the three different cracking morphologies (shown in Figure 3-1) can be attributed to the non-uniform distribution of the size/density of pre-existing defects within starting $MoSe_2$ crystals. In other words, only regions with a large size/density of pre-existing defects experience cracking, and defect-free regions remain seamless after the sulfurization step. Details of our findings in this chapter is presented in References 21-23.

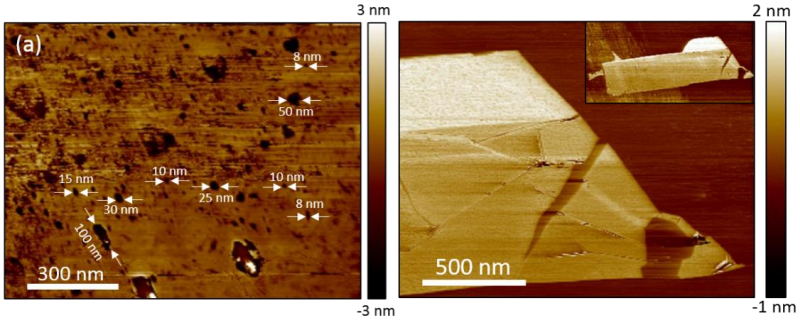

Figure 3-6: AFM imaging of CVD-grown/exfoliated $MoSe_2$ monolayers. AFM images of (a) CVD-grown and (b) exfoliated $MoSe_2$ films before the sulfurization process. The CVD-grown films contain large-scale defects (i.e., pre-existing cracks) with sizes ranging from several nanometers to 100 nm, while the exfoliated sample demonstrates a seamless film with no large-scale defects. We note that observed textures on the exfoliated sample are wrinkles and folds generated during the sample preparation and should not be mistaken for pre-existing cracks. The inset of panel (b) displays the extent of the exfoliated film.

3.3 Control Experiments

In addition to the chalcogen-substitution, other mechanisms may also contribute to the formation of the underlying strain that leads to the fracture of the 2D alloys synthesized

via the post-growth sulfurization of $MoSe_2$. Moreover, the interpretation of the results that were discussed in previous parts of this chapter may also be based on alternative mechanisms rather than strain. In this section, I list the most probable effects and study them via relevant control experiment.

3.3.1 Mismatch of Thermal-Expansion Coefficients

Thermal-expansion coefficients for MoS_2, $MoSe_2$, and SiO_2 are 8.7×10^{-6} $^oC^{-1}$, [17] 1.3×10^{-5} $^oC^{-1}$, [17] and 5.6×10^{-7} $^oC^{-1}$, [18] respectively. Despite the mismatch in thermal-expansion coefficients, Zheng Liu et. al [19] have shown that SiO_2 is not stiff enough to apply a large amount of thermal strain on the MoS_2, which is due to the significantly smaller Young's modulus of SiO_2 (66 GPa) [18] compared to that of the 2D material (177-270 GPa). [20] In addition, we transferred $MoSe_2$ monolayer onto other substrates such as monolayer hexagonal boron nitride (hBN) and then sulfurized the sample. As shown in Figure 3-7, the sulfurized sample are cracked again, meaning that the substrate is not a major player in the cracking of 2D films.

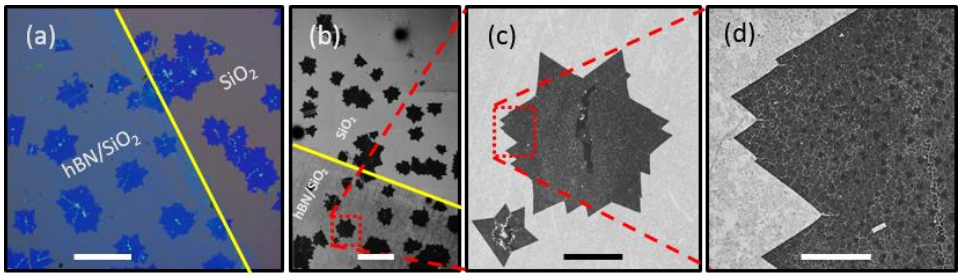

Figure 3-7: Effect of the substrate on the alloying-induced cracking. (a) The optical image of $MoSe_2$ monolayers transferred on a monolayer hBN/SiO_2 substrate (i.e., the region to the left of the yellow line). (b) The SEM image of the same region shown in panel (a). The solid line marks the boundary of the hBN layer underneath $MoSe_2$ monolayers. (c) The magnified SEM image of the $MoSe_2$ film marked in panel (b). (d) The magnified SEM image taken from the region marked in (c), which shows that the sulfurization of $MoSe_2$ transferred on hBN yields a cracked alloy film, similar to our observations on the SiO_2 substrate. Scale bars in (a)-(d) represent, 50 µm, 50 µm, 10 µm, and 2µm, respectively.

3.3.2 Effect of Material Oxidation

Oxidation of the 2D materials, mostly at the crystal grain boundaries, can affect the PL of TMD films. [15] This effect may also be a part of the PL changes observed in Figure 3-4. However, I argue that possible oxidation at the edges of cracks does not significantly contribute into differences observed in the PL spectra collected from cracked and continuous regions. In fact, our observed shift in the PL peak position of MoS_2 films upon cracking is up to 140 meV, which is beyond the capacity of oxidation (i.e., ~20 meV) [15] for changing the emission spectrum of cracked MoS_2 regions. Thus, the contribution of material oxidation is not significant in our study. We also note that oxidative etching causes cracking only at the grain boundaries, while we see cracking even inside of crystal domains. In addition, for oxidative etching, annealing needs to be performed in the presence of an abundant oxygen content (e.g., in air), while our experiments are performed under a relatively high vacuum with a trace oxygen content.

3.3.3 Heterogeneous Spatial Composition

The optical properties of 2D TMDs are influenced by variations in the chemical composition of crystals, [16] which raises the question about the role of possible composition heterogeneities in different PL spectra obtained from cracked and continuous regions. Thus, to map out the elemental composition of the cracked and continuous regions, we carry out time-of-flight secondary-ion mass spectroscopy (ToF-SIMS) with an SEM-level visualization capability and a sub-micron lateral resolution. For this study, we identify a region of the converted sample that contains continuous and cracked films (Figure 3-8(a)) and then characterize it using the PL spectroscopy (Figure 3-8(b)) prior to ToF-SIMS

experiments. As illustrated in Figure 3-8(b), continuous regions emit light at lower energies and display a lower PL intensity, which is consistent with our measurements in Figure 3-4. In ToF-SIMS experiments, we probe (i) Mo, (ii) S, and (iii) Se ions in positive (Figure 3-8(c)) and negative (Figure 3-8(d)) scans (positive/negative refers to the polarity of the ions). Elemental maps in Figure 3-8(c)-(i) and Figure 3-8(d)-(ii) demonstrate the homogeneous incorporation of Mo and S atoms in both cracked and continuous regions of the converted crystals, respectively. This observation rules out non-homogeneous composition conversion as a significant contributor to different PL spectra collected from cracked and continuous crystals. Moreover, the absence of Se atoms in positive (Figure 3-8(c)-(iii)) and negative (Figure 3-8(d)-(iii)) scans reflects the complete conversion of the $MoSe_2$ crystals to MoS_2 (within the limits of the experimental measurements). It is worth noting that ToF-SIMS spectroscopy provides a qualitative analysis of the elemental composition rather than a stoichiometric-level analysis. This is due to the difficulties of preparing standard calibration samples to serve as benchmarks for estimating the precise stoichiometry of the sample under test. However, our qualitative analysis in Figure 3-8 remains reliable as far as the "relative" presence of the elements in cracked and continuous regions is concerned. However, the similarity of the emission spectra obtained from the cracked regions to those obtained from CVD-grown samples implies a complete or near-complete stoichiometric composition of the converted MoS_2 monolayer crystals. It is worth noting that X-ray photoelectron spectroscopy (XPS) has not been used here for two major reasons. First, visualization in XPS (and generally X-ray systems) is not sufficiently advanced to differentiate between cracked and continuous regions in a randomly distributed array of converted MoS_2 crystals. We note that optical imaging (used in XPS)

does not distinguish the cracked regions from the continuous ones (e.g., see Figure 3-4(b)). Second, the X-ray beam cannot be well focused on a small spot; thus, XPS provides a relatively low lateral resolution.

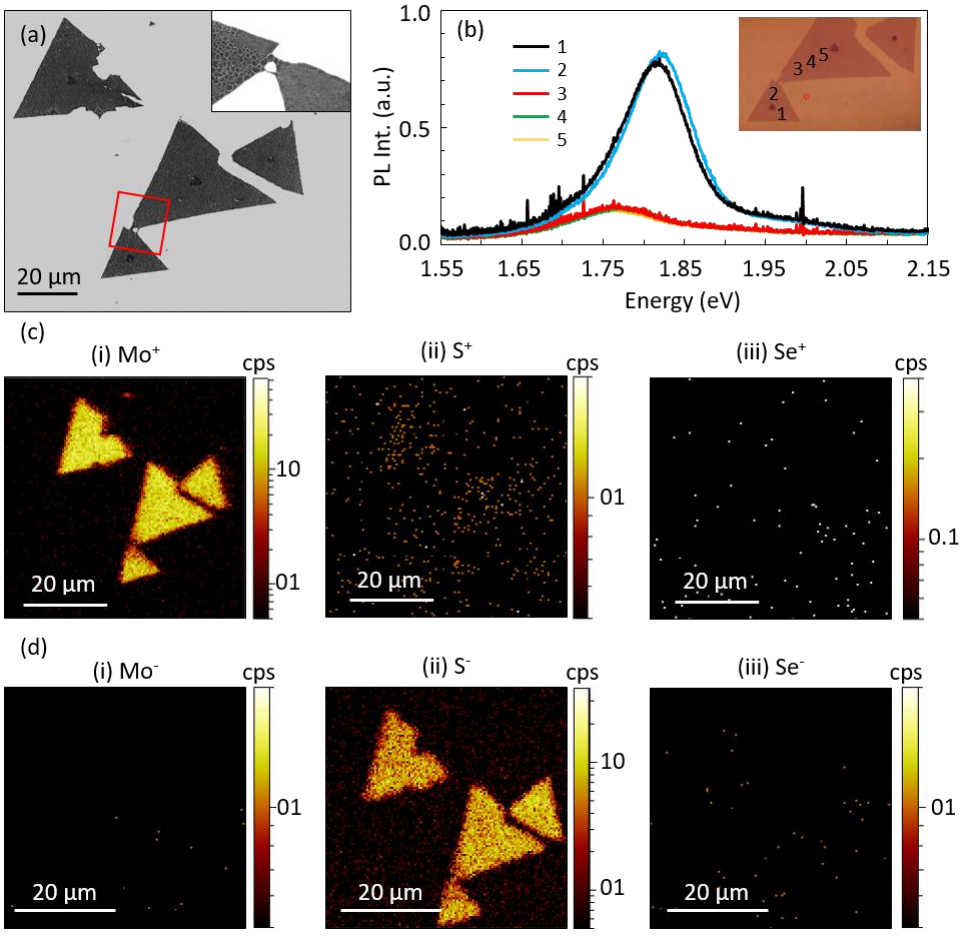

Figure 3-8: Elemental analysis of converted MoS_2 crystals using ToF-SIMS. (a) An SEM image of converted MoS_2 crystals in which cracked (the bottom) and continuous (three top) triangular films coexist. The inset illustrates a highly magnified image of the region marked by the square. (b) PL spectra obtained from several points of the MoS_2 crystals as marked on the optical image in the inset. The PL spectra of the continuous regions (points 3, 4, and 5) sit on the red side of the spectrum and demonstrate low emission intensities. (c, d) Elemental mapping of the converted MoS_2 using ToF-SIMS operated in positive and negative modes, respectively. In both modes, investigated ions are (i) molybdenum (Mo), (ii) sulfur (S), and (iii) selenium (Se). The absence of the Se ions in positive and negative scans confirms that the pristine $MoSe_2$ crystals are fully converted to MoS_2 in both cracked and continuous regions.

3.4 References

1. Hao, S., Yang, B. C. & Gao, Y. L. Quenching induced fracture behaviors of CVD-grown polycrystalline molybdenum disulfide films Rsc Adv. *6*, 59816-59822 (2016).
2. Van der Zande, A. M. et al. Grains and grain boundaries in highly crystalline monolayer molybdenum disulphide. Nat. Mater. *12*, 554-561 (2013).
3. Ly, T. H., Zhao, J., Cichocka, M. O., Li, L. J. & Lee, Y. H. Dynamical observations on the crack tip zone and stress corrosion of two-dimensional MoS_2. Nat. Commun. 8, (2017).
4. Wang, X. N., Tabarraei, A. & Spearot, D. E. Fracture mechanics of monolayer molybdenum disulfide. Nanotechnology 26, (2015).
5. T. H. Ly, J. Zhao, M. O. Cichocka, L. J. Li, and Y. H. Lee, "Dynamical observations on the crack tip zone and stress corrosion of two-dimensional MoS_2," Nat Com 8, (2017).
6. Conley, H. J., Wang, B., Ziegler, J. I., Haglund, R. F., Pantelides, S. T. & Bolotin, K. I. Bandgap engineering of strained monolayer and bilayer MoS_2. Nano Lett. *13*, 3626-3630 (2013).
7. Hui, Y. Y. et al. Exceptional tunability of band energy in a compressively strained trilayer MoS_2 sheet Acs Nano *7*, 7126-7131 (2013).
8. Zhu, C. R. et al. Strain tuning of optical emission energy and polarization in monolayer and bilayer MoS_2. Phys. Rev. B 88, (2013).
9. Plechinger, G. et al. Control of biaxial strain in single-layer molybdenite using local thermal expansion of the substrate 2D Mater. 2, (2015).
10. Lloyd, D. et al. Band gap engineering with ultra-large biaxial strains in suspended monolayer MoS_2. Nano Lett. *16*, 5836-5841 (2015).
11. Berkelbach, T. C., Hybertsen, M. S. & Reichman, D. R. Theory of neutral and charged excitons in monolayer transition metal dichalcogenides. Phys. Rev. B 88, (2013).
12. Bertolazzi, S., Brivio, J. & Kis, A. Stretching and breaking of ultrathin MoS_2. Acs Nano *5*, 9703-9709 (2011).
13. Yang, Y. C. et al. Brittle fracture of 2D $MoSe_2$. Adv. Mater. 29, (2017).
14. Yin, H. Q. et al. Griffith criterion for brittle fracture in graphene. Nano Lett. *15*, 1918-1924 (2015).
15. Nan, H. Y. et al. Strong photoluminescence enhancement of MoS_2 through defect engineering and oxygen bonding. Acs Nano *8*, 5738-5745 (2014).
16. Kim, I. S. et al. Influence of stoichiometry on the optical and electrical properties of chemical vapor deposition derived MoS_2. Acs Nano *8*, 10551-10558 (2014).
17. S. H. E.-M. A. B. L. EVANS, "The Thermal Expansion of 2H-MoS_2, 2H-$MoSe_2$ and 2H-WSe_2 between 20 and 800°C " J. Appl. Cryst (1976).
18. B. El-Kareh, "Fundamentals of semiconductor technologies," Kluwer Academic publishers (2002).
19. Z. Liu, M. Amani, S. Najmaei, Q. Xu, X. L. Zou, W. Zhou, T. Yu, C. Y. Qiu, A. G. Birdwell, F. J. Crowne, R. Vajtai, B. I. Yakobson, Z. H. Xia, M. Dubey, P. M. Ajayan, and J. Lou, "Strain and structure heterogeneity in MoS_2 atomic layers grown by chemical vapour deposition," Nat Commun 5(2014).
20. S. Bertolazzi, J. Brivio, and A. Kis, "Stretching and Breaking of Ultrathin MoS_2," Acs Nano 5, 9703-9709 (2011).

21. H. Taghinejad, A. Eftekhar, P. Campbell, M. Taghinejad, Y. Zhou, E. Reed, E. Vogel, A. Adibi " Alloying-induced biaxial strain in ternary alloys of transition-metal dichalcogenides (TMDs)," SPIE OPTO, Volume 10541, Photonic and Phononic Properties of Engineered Nanostructures VIII Conference, San Francisco, CA (2018).
22. H. Taghinejad, A. Eftekhar, M. Taghinejad, Y. Zhou, E. Reed, A. Adibi "Crack Formation induced by the Post-Growth Alloying of Two-Dimensional Transition-Metal Dichalcogenides," APS March Meeting, volume 63, A37. 00012, Los Angeles, CA (2018).
23. H. Taghinejad, A. Eftekhar, et al " Strain relaxation via formation of cracks in compositionally modulated two-dimensional semiconductor alloys," Nature, 2D Materials and Applications, 2, 10 (2018).

CHAPTER 4. SYNTHESIS OF LATERAL HETEROSTRUCTURES VIA POST-GROWTH ALLOYING

Heterostructures (HSs) of transition-metal dichalcogenides hold promising potentials for a realm of applications that are complementary to those offered by established III-V material platforms. First, the van der Waals interaction of two-dimensional (2D) TMDs in the out-of-plane direction lifts the lattice-matching constraint, which needs to be satisfied for the successful growth of III-V HSs. For instance, despite ~ 20% lattice mismatch, the epitaxial growth of MoS_2 layers on graphene substrates yields low-strain and rotationally commensurate HSs. [1] Therefore, TMD HSs can virtually be integrated on any substrate including flexible materials that are the holy grail of the emerging wearable devices. Second, the reduced dielectric screening and spatial confinement of carriers in an atomically thin plane enhance the Coulomb attraction between electrons and holes within the plane of 2D TMDs. Thus, the binding energy of excitons in TMDs can be as large as ~800 meV, [2] which is approximately two orders of magnitude larger than that in GaAs/AlGaAs HS quantum wells (~ 10 meV). [3] Therefore, the electro-optical modulation of excitonic emission/absorption with a far larger dynamic range (~ exciton binding energy) can be envisioned in TMD HSs. Third, the lifetime of radiative recombination in 2D TMDs (a few picoseconds) [4] is shorter than that in conventional GaAs/AlGaAs HSs (several hundreds of picoseconds), [5] which is a distinctive feature for the design of potentially faster and more efficient optical modulators and light emitters using TMD HSs.

Beyond their inherently unique properties, TMDs can be extensively engineered to better serve as building blocks for the realization of practical HS devices. For instance, the feasibility of synthesizing TMDs in both metallic and semiconducting phases allows for the implementation of all-2D-material device platforms in which the metallic and semiconducting phases can respectively serve as an electrical contact and active region. [6-8] Moreover, the electronic bandgap of the semiconducting phase can be altered via the rational selection of transition metal (Mo, W, etc.) or chalcogen (S, Se, etc.) elements, providing a digital portfolio of materials for operation over a wide spectral range from visible to near-infrared regimes. [9] This digital portfolio can be turned into an analog one through the alloying of 2D TMDs, [10-14] a unique feature that enables the design of 2D materials with customized properties. Such a rich diversity of chemical compositions, material phases, and electronic bandgaps renders TMDs a self-sufficient family of 2D materials for the implementation of HS devices with complex functionalities. In this regard, vertical stacking or lateral stitching of heterogenous TMDs have been employed for the formation of vertical (i.e., out-of-plane) and lateral (i.e., in-plane) heterojunctions, respectively. [15-23]

To put the promising potentials of TMD HSs into practice, advanced methods for the "engineerable" synthesis of high-quality HSs need to be established. Compared to vertical HSs with multiple established synthesis methods, the synthesis of lateral HSs has been far less developed and primarily realized by the edge-epitaxy method. [16, 17, 24] As we discussed in **Error! Reference source not found.**, section1.2, in edge epitaxy the unsaturated edges of a pre-grown TMD lattice serves as an active growth front for the lateral "epitaxy" of a dissimilar TMD film. Because of the relatively similar lattice

constants of various TMDs, edge epitaxy often yields lateral HSs with abrupt and coherent interfaces. However, the geometrical parameters of HSs (e.g., shape and lateral dimensions) are strictly determined by the crystal orientation, lattice symmetry, and chirality of exposed edges. Therefore, only thermodynamically allowed configurations such as triangles or hexagons can be achieved, [25, 26] which are often not practical for real-world applications. In addition, the edge epitaxy fails to produce lateral HSs at intended locations, and therefore, junctions are randomly located across the growth substrate. The lack of control over the spatial morphology of TMD HSs limits the use of the edge-epitaxy in practical applications and calls for alternative approaches capable of realizing lateral junctions with engineerable attributes.

In this chapter, I demonstrate that combining the post-growth alloying of monolayer TMDs (as discussed in CHAPTER 2) with lithographic patterning can provide the missing engineering degrees of freedom needed for the synthesis of lateral TMD HSs with arbitrary shapes and dimensions in pre-defined locations, a set of unique feature that no alternative can currently offer. Beside the full control over the morphology, our approach allows for the precise and continuous tuning of the bandgap energy on both sides of a heterojunction, an extra degree of freedom that enables customizing optoelectronic properties at the HS interface. In a representative demonstration, we employ monolayer films of $MoSe_2$ and convert them into $MoS_{2x}Se_{2(1-x)}$-$MoS_{2y}Se_{2(1-y)}$ lateral HSs in which optoelectronic properties of the engineered junctions are controllable by tuning x and y values. Using a systematic scanning transmission electron microscopy (STEM) analysis, we demonstrate that the post-growth alloying of monolayer $MoSe_2$ films yields a randomly mixed Mo-S-

Se compound, further supporting the feasibility of continuous bandgap tuning at the HS interface.

4.1 Heterostructure Synthesis Protocol

Our synthesis approach relies on converting monolayer TMD crystals into lateral HSs following a spatially controlled chalcogen substitution in pristine TMD monolayers. Figure 4-1(a) schematically illustrates our fabrication scheme for the formation of a prototypical lateral junction between $MoSe_2$ and MoS_2 monolayers. We protect desired parts of a pristine $MoSe_2$ monolayer by an inert mask that is assembled on top of the 2D material *via* standard lithography and deposition steps. Then, we anneal the sample in a sulfur (S) ambient to replace selenium (Se) atoms by S atoms in only exposed parts of the starting $MoSe_2$ film, yielding a lateral heterojunction between $MoSe_2$ (under protected regions) and MoS_2 (in exposed regions). To experimentally demonstrate this protocol, we employ an e-beam evaporated SiO_2 layer as the protecting mask (Figure 4-1(b)) and then anneal the sample under sulfur vapor for 15 mins at 950 ^oC to enable the chalcogen swapping. Our experiments suggest that for complete protection, the thickness of the SiO_2 mask should be at least 70 nm.

Photoluminescence (PL) mapping of the sample before (Figure 4-1(c)) and after (Figure 4-1(d)) annealing confirms that the sulfurization of the patterned $MoSe_2$ monolayer can successfully establish a lateral $MoSe_2$-MoS_2 HS. Indeed, the PL peak position at 680 ± 5 nm in sulfurized regions between SiO_2 lines mimics that of a pristine MoS_2 film, while the PL peak position at 820 ± 7 nm in the protected regions remains intact and identical to that of the starting $MoSe_2$ film. Furthermore, as shown in Figure 4-1(e), representative PL

spectra obtained from the two sides of the junction exhibit standard excitonic emission expected from $MoSe_2$ and MoS_2 monolayers. Similar conclusions can be obtained from Raman mapping (Figure 4-1(f-h)) in which, after the sulfurization step, the out-of-plane A_{1g} resonance of $MoSe_2$ at 241 ± 0.2 cm^{-1} disappears and the A_{1g} mode of MoS_2 at 408 ± 0.5 cm^{-1} appears in exposed regions. In addition to the A_{1g} mode, the representative Raman spectrum of sulfurized regions (Figure 4-1(i)) contains the in-plane Raman mode of MoS_2 (*i.e.*, E^1_{2g} mode) at 388 ± 0.5 cm^{-1}, which verifies that a high-quality lattice is established. Collectively, our Raman and PL studies substantiate that the chalcogen substitution is exclusive to the exposed regions of the starting $MoSe_2$ film, and the employed sulfurization process does no harm to the protected parts of the monolayer film. We note that our HS-synthesis approach is not limited to CVD-grown TMDs.

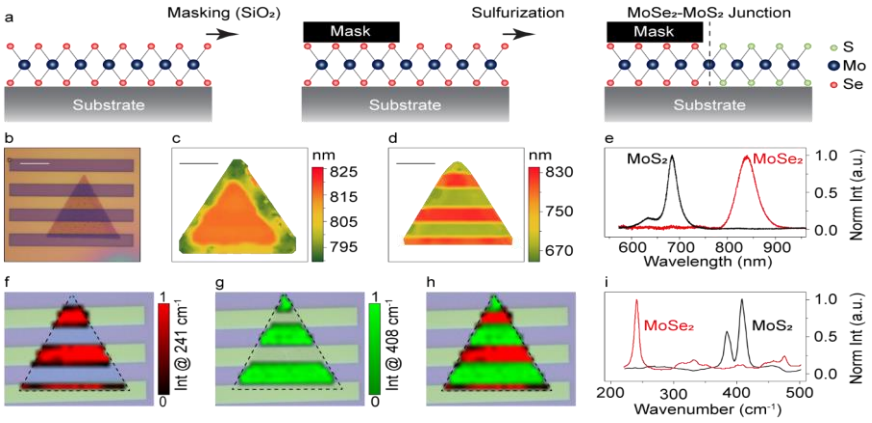

Figure 4-1: Fabrication of $MoSe_2$-MoS_2 lateral HSs. (a) The schematic description of the HS synthesis protocol based on the sulfurization of patterned $MoSe_2$ monolayers. (b) Optical image of a representative lateral HS. The thickness of the SiO_2 mask is 70 nm. (c, d) The spatial profile of the PL peak position before and after sulfurization at 950 ^oC for 15 mins, respectively. The emission wavelength in sulfurized and protected regions are 680 ± 5 nm and 820 ± 7 nm, respectively. In panel (c), the heterogeneities at the rim of the $MoSe_2$ film is due to previously reported edge effects. [34] (e) Representative PL spectra of protected $MoSe_2$ and converted MoS_2 monolayers. (f, g) Mapping the intensity of the A_{1g} Raman modes of $MoSe_2$ at 241 cm^{-1} and MoS_2 at 408 cm^{-1}, respectively. (h) The overlay of the maps shown in panels (f) and (g), which displays the formation of $MoSe_2$-MoS_2 lateral HSs. (i). Representative Raman spectra of protected $MoSe_2$ and converted MoS_2 monolayers. Scale bars in panels (b)-(d) represent 2 µm.

The integration of a lithography step with our employed sulfurization method enables the design of lateral TMD HSs with arbitrary shapes and dimensions in predefined locations, a set of features that no alternative approach can currently offer. In addition to the strip lines shown in Figure 4-1, we have presented examples of other geometries such as circular or any arbitrarily shaped (e.g., a smiley face) HSs in Figure 4-2. We note that such structures can be designed in cascaded arrangements for the realization of HSs with multiple junctions (e.g., Figure 4-1), all obtained in one straightforward sulfurization step. In contrast, the synthesis of multijunction configurations via alternative methods, such as edge-epitaxy, demands a complex system for the cyclic activation of different precursors for the sequential assembly of one TMD film on the edge of another dissimilar TMD film, [24]yet offering no systematic control over the spatial profile and lateral size of the obtained junctions. Thus, we believe that our approach provides the missing engineering element for potential fabrication of practical optoelectronic devices based on TMD HSs.

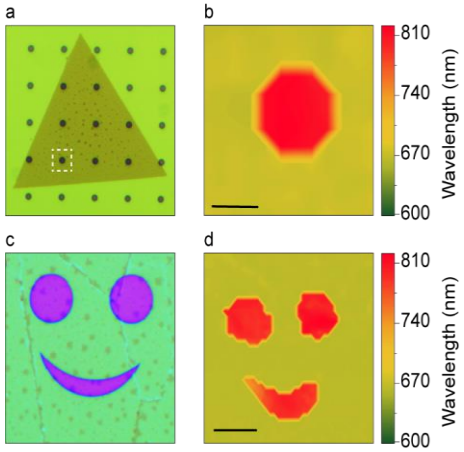

Figure 4-2: Fabrication of HSs with arbitrary geometries. (a) The optical image of an array of lateral HSs with circular geometries. (b) PL mapping across the region outlined by the dashed box in panel (a). (c, d) The optical image and PL map of a lateral HS in the shape of a smiley face, respectively, which exemplifies the possibility of forming HSs with arbitrary shapes. Color bars represent the wavelength of maximum PL intensity. Samples were sulfurized at 950 ^{o}C for 15 mins. Scale bars represent 2 µm and 10 µm in panels (b) and (d), respectively.

I note that, the e-beam lithography enables formation of patterns with lateral dimensions down to ~ 10 nm. However, this limit should not be simply projected into achievable lateral dimensions in our developed HS protocol. In fact, we have noticed that narrow SiO_2 lines cannot fully protect $MoSe_2$ films, probably because the sulfur gas can penetrate underneath SiO_2 masks. As a result, after the sulfurization process, the real size of remaining $MoSe_2$ segments are smaller than the lithographically defined dimensions. To experimentally illustrate this effect, we patterned sub-micrometer (~ 800 nm) SiO_2 masks on $MoSe_2$ monolayers (Figure 4-3(a)) and sulfurized the sample at 950 ^oC for 15 mins. As the Raman map in Figure 4-3(b) shows, in the protected regions, signatures of Mo-S bonds can be resolved, meaning that the sulfur gas penetrates underneath the narrow SiO_2 lines and leads to the partial S-Se exchange. Our experiments show that SiO_2 lines narrower than 300 nm are fully permeable and a complete S-Se substation occurs underneath the SiO_2 masks. However, I do believe that there is no fundamental limitation for pushing the lateral dimensions down to the limits of lithography if alternative masking materials with less gas permeability are developed.

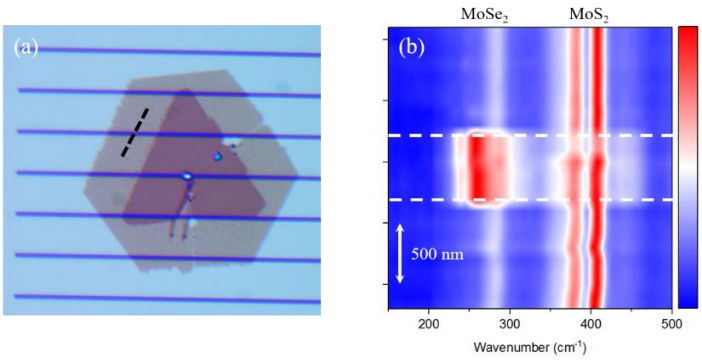

Figure 4-3: Sulfur penetration underneath narrow SiO_2 masks. (a) Optical image of a $MoSe_2$ film patterned with ~*8*00 nm-wide SiO_2 lines and sulfurized at 950 ^oC for 15 mins. (b) The Raman map across the dashed line shown in panel (a). The Raman spectra reveals the signature of Mo-S bonds under the protected region underneath the SiO_2 line (i.e., the region between the dashed lines).

4.2 Bandgap Engineering in Lateral Heterostructures

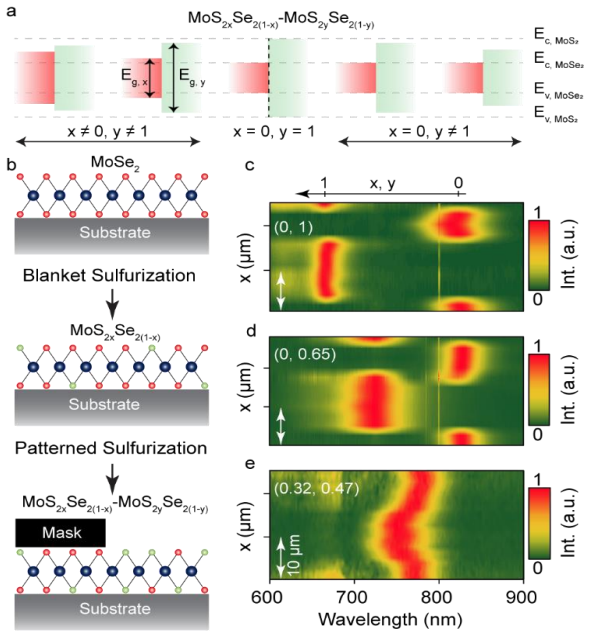

Figure 4-4: Tuning bandgap energies at the HS interface. (a) The schematic illustration of band alignments at the interface of an $MoS_{2x}Se_{2(1-x)}$-$MoS_{2y}Se_{2(1-y)}$ HS with x < y. Independent modulation of x and y enables independent control of the bandgap energy (E_g) on either side of the junction. As a reference, the minimum of the conduction band (E_c) and the maximum of the valance band (E_v) are shown for MoS_2 and $MoSe_2$ compositions. (b) The schematic representation of steps taken for the realization of an (x, y)-HS with x < y. (c-e) PL maps of three HSs with various (x, y) combinations as marked on the panels. The patterned sulfurization was performed at 950 ^oC, 850 ^oC, and 750 ^oC for 15 mins on samples shown in panels (c), (d), and (e) respectively. The blanket sulfurization performed at 800 ^oC for 5 min on sample shown in panel (e).

The optoelectronic behavior of semiconducting HSs primarily depends on the alignment of energy bands at the interface, where the carrier exchange and charge transport are predominantly influenced. Thus, engineering the optoelectronic performance of most HS devices such as transistors, lasers, light-emitting diodes, and solar cells often needs the tuning of energy bands at the interface. Previous studies have shown that, unlike vertical HSs, the lateral HSs of TMDs obtain a type-I band alignment in which the band edges of the large-bandgap material (*e.g.*, WSe_2) straddle those of the small-bandgap material (*e.g.*,

MoS_2). [27, 28] Here, we demonstrate that bandgap energies can be independently tuned on either side of such a type-I heterojunction *via* controlling the degree of chalcogen substitution. We establish a junction between $MoS_{2x}Se_{2(1-x)}$ and $MoS_{2y}Se_{2(1-y)}$ alloys ($x \neq y$, $0 < x, y < 1$) in which the independent control of x and y enables bandgap modulation at the HS interface (Figure 4-4(a)). We refer to these HSs as (x, y)-HSs in the remaining parts of this paper. Such a tuning mechanism is well supported by previous *ab initio* calculations, which suggest that changing the alloy composition linearly modulates the conduction-band minimum and valance-band maximum, hence, leading to the linear modulation of the bandgap energy in Mo-S-Se alloys. [29. 30]

As Figure 4-4(b) schematically displays, (x, y)-HSs can be realized *via* a three-step process: (i) the formation of the $MoS_{2x}Se_{2(1-x)}$ alloy *via* a blanket sulfurization of the starting $MoSe_2$ monolayer; (ii) the formation of SiO_2 masks in desired parts of the $MoS_{2x}Se_{2(1-x)}$ alloy; and (iii) the formation of the $MoS_{2y}Se_{2(1-y)}$ side *via* a second sulfurization step for increasing the sulfur content from x to y in unmasked regions ($y > x$). To study the modulation of interface properties, we use PL mapping to probe the variation of the bandgap energy (E_g) across the interface of synthesized (x, y)-HSs with various (x, y) combinations. Figure 4-4(c, d) displays representative examples of (x, y)-HSs in which only one side of the junctions (*i.e.*, the y side) are sulfurized, while the other side of the junction is kept intact at $x = 0$. According to the PL mapping, our strategy has led to the formation of (0, 1) and (0, 0.65) heterojunctions with the bandgap energies of (1.50 eV, 1.82 eV) and (1.50 eV, 1.71 eV), respectively.

The tuning of interfacial properties can be further extended to both sides of a lateral HS. As shown in a representative example in Figure 4-4(e), we first perform a blanket

sulfurization to establish an alloy with x ≈ 0.32, and then we fabricate the SiO_2 mask and increase the sulfur content in unmasked regions to y ≈ 0.47 through the second sulfurization step. Accordingly, a (0.32, 0.47)-HS with bandgap energies of (1.60 eV, 1.65 eV) is created, a demonstration that showcases the possibility of modulating both sides of an interface *via* a controlled sulfurization process. In our approach, the bandgap on either side of the junction can be independently tuned within a ~320 meV energy range, covering any arbitrary energy between 1.5 eV (in $MoSe_2$) and 1.82eV (in MoS_2). We note that the composition of alloys can be set through changing the sulfurization temperature. We believe that our approach can be applied to other TMD pairs such as WSe_2 (E_g ≈ 1.65 eV)-WS_2 (E_g ≈ 2.1 eV), which expands the diversity of bandgap energies that can be brought together at the interface of lateral TMD HSs. Here, I would like to note that the continuous tuning of the bandgap in lateral HSs stems from the random intermixing of S and Se elements during the sulfurization process. (see section 2.2 for details)

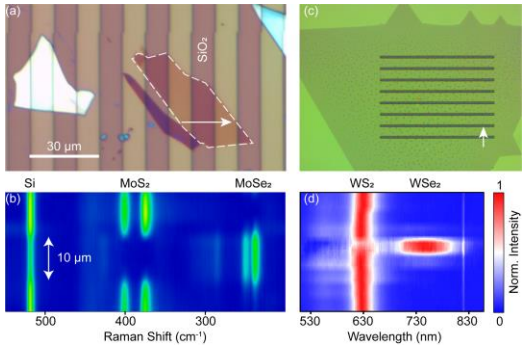

Figure 4-5: Universality of HS synthesis approach. (a) A representative optical image of an exfoliated $MoSe_2$ film converted into a lateral HS. The dashed line outlines the monolayer region. (b) Raman mapping across the arrow shown in panel (a). The observation of MoS_2 Raman lines in exposed regions and those of $MoSe_2$ in protected regions confirms the formation of a lateral HS in the exfoliated film. The Raman line of silicon (Si) serves as the reference in the Raman mapping. (c) Optical image of a WSe_2 film patterned with and an array of 5 μm-wide SiO_2 strips and sulfurized at ~1000 ºC for 15 mins. (b) The PL map across the arrow shown in panel (c). The observation of WSe_2 PL at ~ 755 nm in unmasked regions and WS_2 at ~ 630 nm in the masked region confirms the formation of WSe_2-WS_2 lateral HSs.

Synthesis of lateral HS using our developed post-growth alloying method is not limited to the CVD-grown films and any type of starting material such as exfoliated $MoSe_2$ also fits into our synthesis protocol. As we have shown in a representative example in Figure 4-5 (a), SiO_2 protection masks are pattered on an exfoliated $MoSe_2$ monolayer and then sulfurized at 950 ^oC for 15 to enable Se-Se atomic exchange. Raman mapping (Figure 4-5(b)) across a SiO_2 line directly confirms the formation of MoS_2-$MoSe_2$ lateral junctions in an exfoliated monolayer film. More importantly, lateral junctions can be established between dissimilar TMD films other than MoS_2 and $MoSe_2$. As we have shown in an example in Figure 4-5(c, d), using the similar lithographically generated SiO_2 masks and subsequent sulfurization, monolayer WSe_2 crystals can be converted into later WSe_2-WS_2 lateral junction. Thus, we conclude that our developed methodology is not constrained to any specific type or composition of the starting binary films and can be universally used for the formation of lateral junctions between various monolayer TMD films with virtually any synthesis root.

4.3 Electrical Characterization of Lateral HSs

Finally, we study the field-effect response of the as-synthesized lateral HSs *via* the fabrication of an electrical device that is schematically depicted in Figure 4-6(a). In our device architecture, two metal contacts (Au/Ti: 60/20 nm) are deposited on the two sides of the $MoSe_2$ region (*i.e.*, the protected region) so that a $MoS_{2x}Se_{2(1-x)}$ – $MoSe_2$ – $MoS_{2x}Se_{2(1-x)}$ double-junction HS forms between the electrical contacts (Figure 4-6(b)). The transfer characteristic of the device, Figure 4-6(c), clearly shows a field-effect behavior in which the drain-source current (I_{ds}) monotonically increases as the gate-source voltage (V_{gs}) is increased. The I_{ds}–V_{gs} curves suggest that the 2D material is intrinsically n

doped, probably due to the chalcogen vacancies as discussed above. In addition to the transfer curves, changing the back-gate voltage (*i.e.*, V_{gs}) modulates the output characteristic of the device (Figure 4-6(d)).

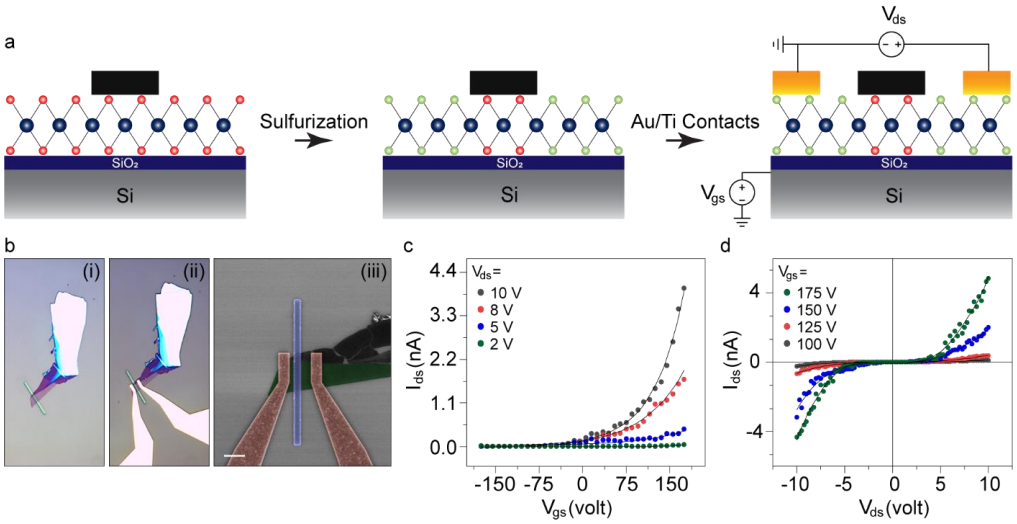

Figure 4-6: Field-effect response of lateral HSs. (a) The schematic representation of fabrication steps. Electrical contacts to drain and source are made of Au/Ti: 60/20 nm. Drain-source (ds) and gate-source (gs) polarities are designated on the schematic. (b) Optical images of the HS (i) before and (ii) after the formation of electrical contacts. The SEM image of the junction area is shown in part (iii). Blue: SiO_2 mask; green: exfoliated monolayer 2D material; brown: Au/Ti contacts. The scale bar in panel (b-iii) represents 5 µm. (c) The transfer curves (i.e., I_{ds}-V_{gs}) measured at multiple drain-source voltages (V_{ds}). (d) The output characteristic (i.e., I_{ds}-V_{ds}) measured at multiple gate-source voltages (V_{gs}).

The I_{ds}–V_{ds} curves of the double junction HS display an asymmetric response in which the ON voltages for positive and negative V_{ds} are slightly different. This effect could stem from minor differences between the left and right HS interfaces in the current path. As shown in Figure 4-7, For $V_{ds} > 0$, the electronic transport marked as (1) determines the I-V characteristic, while transport (2) occurs without any barrier. Thus, the electrical response is predominantly dictated by the right junction. Similarly, for the $V_{ds} < 0$, the transport marked as (2) and, accordingly, the left junction determines the I-V characteristic. Therefore, the difference observed in negative and positive V_{ds} in I_{ds}-V_{ds} response of our

double-junction device is due to minor difference in left and right junctions. Overall, considering the spatial addressability of the lateral junctions provided by the integration of a lithography step into the synthesis protocol, our electrical characterizations highlight the possibility of demonstrating advanced optoelectronic devices such as transistors, light emitters, and photodetectors using lateral TMD HSs. Further details of results presented in this chapter can be found in reference [35-39].

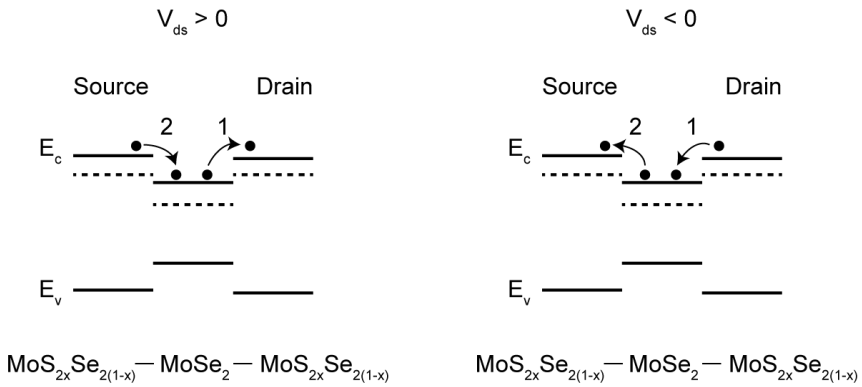

Figure 4-7: Simplified band alignment of the $MoS_{2x}Se_{2(1-x)}$ – $MoSe_2$ – $MoS_{2x}Se_{2(1-x)}$ double-junction device. Charge transport under $V_{ds} > 0$ (shown in the left panel) and $V_{ds} < 0$ (shown in the right panel). Considering $V_{gs} > 0$, we have assumed an electron-dominated charge transport.

4.4 References

1. Liu, X.; Balla, I.; Bergeron, H.; Campbell, G. P.; Bedzyk, M. J.; Hersam, M. C., Rotationally Commensurate Growth of MoS_2 on Epitaxial Graphene. *ACS Nano* **2016,** *10*, 1067-75.
2. Hanbicki, A. T.; Currie, M.; Kioseoglou, G.; Friedman, A. L.; Jonker, B. T., Measurement of High Exciton Binding Energy in the Monolayer Transition-Metal Dichalcogenides WS_2 and WSe_2. *Solid State Commun.* **2015,** *203*, 16-20.
3. Meney, A. T., Exciton Binding-Energies and Absorption in Intermixed GaAs-AlGaAs Quantum-Wells. *J. Appl. Phys.* **1992,** *72*, 5729-5734.
4. Wang, G.; Palleau, E.; Amand, T.; Tongay, S.; Marie, X.; Urbaszek, B., Polarization and Time-Resolved Photoluminescence Spectroscopy of Excitons in $MoSe_2$ Monolayers. *Appl Phys. Lett.* **2015,** *106*.

5. Meftah, A.; Ajlani, H.; Aloulou, S.; Oueslati, M.; Scalbert, D.; Allegre, J.; Maaref, H., Time-Resolved Photoluminescence of Delta-Doped AlGaAs/GaAs Heterostructures. *J. Lumin.* **2008,** *128*, 1317-1322.
6. Kappera, R.; Voiry, D.; Yalcin, S. E.; Branch, B.; Gupta, G.; Mohite, A. D.; Chhowalla, M., Phase-Engineered Low-Resistance Contacts for Ultrathin MoS_2 Transistors. *Nat. Mater.* **2014,** *13*, 1128-1134.
7. Duerloo, K. A. N.; Li, Y.; Reed, E. J., Structural Phase Transitions in Two-Dimensional Mo- and W-Dichalcogenide Monolayers. *Nat. Commun.* **2014,** *5*,4214.
8. Peng, J.; Liu, Y.; Luo, X.; Wu, J.; Lin, Y.; Guo, Y.; Zhao, J.; Wu, X.; Wu, C.; Xie, Y., High Phase Purity of Large-Sized 1T'-MoS_2 Monolayers with 2d Superconductivity. *Adv. Mater.* **2019,** *31*, 1900568.
9. Zhang, C. X.; Gong, C.; Nie, Y. F.; Min, K. A.; Liang, C. P.; Oh, Y. J.; Zhang, H. J.; Wang, W. H.; Hong, S.; Colombo, L.; Wallace, R. M.; Cho, K., Systematic Study of Electronic Structure and Band Alignment of Monolayer Transition Metal Dichalcogenides in Van Der Waals Heterostructures. *2d Materials* **2017,** *4*, 015026.
10. Taghinejad, H.; Rehn, D. A.; Muccianti, C.; Eftekhar, A. A.; Tian, M.; Fan, T.; Zhang, X.; Meng, Y.; Chen, Y.; Nguyen, T. V.; Shi, S. F.; Ajayan, P. M.; Schaibley, J.; Reed, E. J.; Adibi, A., Defect-Mediated Alloying of Monolayer Transition-Metal Dichalcogenides. *ACS Nano* **2018**, *12*, 12795-12804.
11. Taghinejad, H.; Eftekhar, A. A.; Campbell, P. M.; Beatty, B.; Taghinejad, M.; Zhou, Y.; Perini, C. J.; Moradinejad, H.; Henderson, W. J.; Woods, E. V.; Zhang, X.; Ajayan, P. M.; Reed, E. J.; Vogel, E. M.; Adibi, A., Strain Relaxation Via Formation of Cracks in Compositionally Modulated Two-Dimensional Semiconductor Alloys. *npj 2D Materials ad Applications* **2018,** *2*, 8.
12. Feng, Q.; Mao, N.; Wu, J.; Xu, H.; Wang, C.; Zhang, J.; Xie, L., Growth of $MoS_{(2(1-X))}Se_{(2x)}$ (X = 0.41-1.00) Monolayer Alloys with Controlled Morphology by Physical Vapor Deposition. *ACS Nano* **2015,** *9*, 7450-5.
13. Su, S.-H.; Hsu, W.-T.; Hsu, C.-L.; Chen, C.-H.; Chiu, M.-H.; Lin, Y.-C.; Chang, W.-H.; Suenaga, K.; He, J.-H.; Li, L.-J., Controllable Synthesis of Band-Gap-Tunable and Monolayer Transition-Metal Dichalcogenide Alloys. *Front. Energy Res.* **2014,** *2*, 8.
14. Susarla, S.; Hachtel, J. A.; Yang, X.; Kutana, A.; Apte, A.; Jin, Z.; Vajtai, R.; Idrobo, J. C.; Lou, J.; Yakobson, B. I.; Tiwary, C. S.; Ajayan, P. M., Thermally Induced 2d Alloy-Heterostructure Transformation in Quaternary Alloys. *Adv. Mater.* **2018,** *30*, 1804218.
15. Taghinejad, H.; Eftekhar, A. A.; Adibi, A., Lateral and Vertical Heterostructures in Two-Dimensional Transition-Metal Dichalcogenides. *Opt. Mater. Express.* **2019,** *9*, 1590-1607.
16. Duan, X.; Wang, C.; Shaw, J. C.; Cheng, R.; Chen, Y.; Li, H.; Wu, X.; Tang, Y.; Zhang, Q.; Pan, A.; Jiang, J.; Yu, R.; Huang, Y.; Duan, X., Lateral Epitaxial Growth of Two-Dimensional Layered Semiconductor Heterojunctions. *Nat. Nanotechnol.* **2014,** *9*, 1024-1030.
17. Gong, Y.; Lin, J.; Wang, X.; Shi, G.; Lei, S.; Lin, Z.; Zou, X.; Ye, G.; Vajtai, R.; Yakobson, B. I.; Terrones, H.; Terrones, M.; Tay, B. K.; Lou, J.; Pantelides, S. T.; Liu, Z.; Zhou, W.; Ajayan, P. M., Vertical and in-Plane Heterostructures from WS_2/MoS_2 Monolayers. *Nat. Mater.* **2014,** *13*, 1135-1142.

18. Lu, N.; Guo, H.; Zhuo, Z.; Wang, L.; Wu, X.; Zeng, X. C., Twisted MX_2/MoS_2 Heterobilayers: Effect of Van Der Waals Interaction on the Electronic Structure. *Nanoscale* **2017,** *9*, 19131-19138.
19. Zhou, R.; Ostwal, V.; Appenzeller, J., Vertical Versus Lateral Two-Dimensional Heterostructures: On the Topic of Atomically Abrupt P/N-Junctions. *Nano Lett.* **2017,** *17*, 4787-4792.
20. Lee, J. B.; Lim, Y. R.; Katiyar, A. K.; Song, W.; Lim, J.; Bae, S.; Kim, T. W.; Lee, S. K.; Ahn, J. H., Direct Synthesis of a Self-Assembled WSe_2 /MoS_2 Heterostructure Array and Its Optoelectrical Properties. *Adv. Mater.* **2019,** *31*, 1904194.
21. Zhang, J.; Wang, J.; Chen, P.; Sun, Y.; Wu, S.; Jia, Z.; Lu, X.; Yu, H.; Chen, W.; Zhu, J.; Xie, G.; Yang, R.; Shi, D.; Xu, X.; Xiang, J.; Liu, K.; Zhang, G., Observation of Strong Interlayer Coupling in MoS_2/WS_2 Heterostructures. *Adv. Mater.* **2016,** *28*, 1950-1956.
22. Lee, I.; Rathi, S.; Lim, D.; Li, L.; Park, J.; Lee, Y.; Yi, K. S.; Dhakal, K. P.; Kim, J.; Lee, C.; Lee, G.-H.; Kim, Y. D.; Hone, J.; Yun, S. J.; Youn, D.-H.; Kim, G.-H., Gate-Tunable Hole and Electron Carrier Transport in Atomically Thin Dual-Channel WSe_2/MoS_2 Heterostructure for Ambipolar Field-Effect Transistors. *Adv. Mater.* **2016,** *28*, 9519-9525.
23. Mahjouri-Samani, M.; Lin, M. W.; Wang, K.; Lupini, A. R.; Lee, J.; Basile, L.; Boulesbaa, A.; Rouleau, C. M.; Puretzky, A. A.; Ivanov, I. N.; Xiao, K.; Yoon, M.; Geohegan, D. B., Patterned Arrays of Lateral Heterojunctions within Monolayer Two-Dimensional Semiconductors. *Nat. Commun.* **2015,** *6*, 7749.
24. Sahoo, P. K.; Memaran, S.; Xin, Y.; Balicas, L.; Gutierrez, H. R., One-Pot Growth of Two-Dimensional Lateral Heterostructures Via Sequential Edge-Epitaxy. *Nature* **2018,** *553*, 63-67.
25. Zhang, X. Q.; Lin, C. H.; Tseng, Y. W.; Huang, K. H.; Lee, Y. H., Synthesis of Lateral Heterostructures of Semiconducting Atomic Layers. *Nano Lett.* **2015,** *15*, 410-415.
26. Zhou, J.; Tang, B.; Lin, J. L., D.; Shi, J.; Sun, L.; Zeng, Q.; Niu, L.; Liu, F.; Wang, X.; Liu, X.; Suenaga, K.; Jin, C.; Liu, Z., Morphology Engineering in Monolayer MoS_2-WS_2 Lateral Heterostructures. *Adv. Func. Mater*. **2018,** *28*, 1-7.
27. Zhang, C. D.; Li, M. Y.; Tersoff, J.; Han, Y. M.; Su, Y. S.; Li, L. J.; Muller, D. A.; Shih, C. K., Strain Distributions and Their Influence on Electronic Structures of WSe_2-MoS_2 Laterally Strained Heterojunctions. *Nat. Nanotechnol.* **2018,** *13*, 152-158.
28. Li, M.-Y.; Pu, J.; Huang, J.-K.; Miyauchi, Y.; Matsuda, K.; Takenobu, T.; Li, L.-J., Self-Aligned and Scalable Growth of Monolayer WSe_2–MoS_2 Lateral Heterojunctions. *Adv. Func. Mater*. **2018,** *28*, 1706860.
29. Kang, J.; Tongay, S.; Li, J. B.; Wu, J. Q., Monolayer Semiconducting Transition Metal Dichalcogenide Alloys: Stability and Band Bowing. *J Appl. Phys.* **2013,** *113*.
30. Yuan, X.; Yang, M. Y.; Wang, L.; Li, Y. Y., Structural Stability and Intriguing Electronic Properties of Two-Dimensional Transition Metal Dichalcogenide Alloys. *Physical Chemistry Chemical Physics* **2017,** *19*, 13846-13854.
31. Mahjouri-Samani, M.; Liang, L.; Oyedele, A.; Kim, Y.-S.; Tian, M.; Cross, N.; Wang, K.; Lin, M.-W.; Boulesbaa, A.; Rouleau, C. M.; Puretzky, A. A.; Xiao, K.; Yoon, M.; Eres, G.; Duscher, G.; Sumpter, B. G.; Geohegan, D. B., Tailoring Vacancies Far Beyond Intrinsic Levels Changes the Carrier Type and Optical Response in Monolayer $MoSe_{2-x}$ Crystals. Nano Lett. 2016, 16, 5213-5220.

32. Taghinejad, H.; Taghinejad, M.; Tarasov, A.; Tsa, M.-Y.; Hosseinnia, A. H.; Moradinejad, H.; Campbell, P. M.; Eftekhar, A. A.; Vogel, E. M.; Adibi, A., Resonant Light-Induced Heating in Hybrid Cavity-Coupled 2d Transition-Metal Dichalcogenides. *ACS Photonics* **2016,** *3*, 8.
33. Baugher, B. W. H.; Churchill, H. O. H.; Yang, Y. F.; Jarillo-Herrero, P., Intrinsic Electronic Transport Properties of High-Quality Monolayer and Bilayer MoS_2. *Nano Lett.* **2013,** *13*, 4212-4216.
34. Bao, W.; Borys, N. J.; Ko, C.; Suh, J.; Fan, W.; Thron, A.; Zhang, Y. J.; Buyanin, A.; Zhang, J.; Cabrini, S.; Ashby, P. D.; Weber-Bargioni, A.; Tongay, S.; Aloni, S.; Ogletree, D. F.; Wu, J. Q.; Salmeron, M. B.; Schuck, P. J., Visualizing Nanoscale Excitonic Relaxation Properties of Disordered Edges and Grain Boundaries in Monolayer Molybdenum Disulfide. *Nat. Commun.* **2015,** *6*, 7993.

35. Taghinejad, H.; Eftekhar, A. A.; Li, Z.; West, M. P.; Javani, M. H.; Abdollahramezani, S.; Zhang, X.; Tian, M.; Johnson-Averette, T.; Ajayan, P. M.; Vogel, E. M.; Shi, S. F.; Cai, W.; Adibi, A., Highly controlled lateral heterostructures in 2D transition metal dichalcogenides for optoelectronic applications. *ACS Nano* **2020,** *DOI: https://doi.org/10.1021/acsnano.0c02885*.

36. H. Taghinejad, A. Eftekhar, P. Campbell, M. Taghinejad, Y. Zhou, E. Reed, E. Vogel, A. Adibi " Alloying-induced biaxial strain in ternary alloys of transition-metal dichalcogenides (TMDs)," SPIE OPTO, volume 10541, 1054112, Photonic and Phononic Properties of Engineered Nanostructures VIII, San Francisco, CA (2018).
37. H. Taghinejad " Synthesis of lateral heterostructures of transition-metal dichalcogenides via spatially-controlled alloying," SPIE OPTO, volume 10927, 1092707, Photonic and Phononic Properties of Engineered Nanostructures IX Conference, San Francisco, CA (2019).
38. H. Taghinejad, A. Eftekhar, A. Adibi " Lateral heterostructures in two-dimensional transition metal dichaolcogenides for optoelectronic applications," SPIE Nanoscience + Engineering, volume 10721, 107210L, Active Photonic Platforms X Conference, San Diego, CA (2018).
39. H. Taghinejad, A. Eftekhar, A. Adibi " Planar heterostructures through selective-area alloying of 2D transition metal dichalcogenide," SPIE OPTO, volume 10534, 105340R, 2D Photonic Materials and Devices Conference, San Francisco, CA (2018).

CHAPTER 5. MASKLESS SYNTHESIS OF LATERAL HETEROSTRUCTURES

My conclusions about the important role of defects in post-growth alloying of $MoSe_2$ monolayers inspired me to explore the possibility of maskless synthesis of lateral HSs using defect engineering. As I discussed in section 2.3, defects can facilitate the exchange of chalcogen atoms during the post-growth alloying process. In other words, a larger density of defects in starting $MoSe_2$ crystals lowers the driving force for the Se-S exchange, implying that the sulfurization process can be conducted at a relatively lower temperature as compared to that of a defect-free crystal. This critical observation encouraged me to artificially engineer the spatial distribution of defects in an otherwise pristine $MoSe_2$ and leverage a delicately induced spatial inhomogeneity for the realization of a maskless technique for the synthesis of lateral HSs.

In this chapter, I will first demonstrate that focused-ion beam (FIB) irradiation of TMDs can be employed for the controlled introduction of defects and structural deformations in intended locations of a pristine $MoSe_2$ crystal with a spatial resolution down to a few tens of nanometers. Using multiple characterization techniques, the effect of ion dosage on the $MoSe_2$ monolayers will be systematically explored and accordingly leveraged for the optimization of the FIB-irradiation treatment. Then, I introduce a modified version of our previously developed post-growth alloying strategy for the selective substitution of chalcogen atoms in only FIB-treated regions without affecting the pristine $MoSe_2$ parts, leading to the realization of lateral $MoSe_2$-MoS_2 HSs. The developed method in this chapter enables the synthesis of lateral HSs with unprecedentedly small

lateral dimensions and tunable interfacial properties. I will conclude this chapter with a direct comparison between the maskless and mask-assisted HS synthesis techniques.

5.1 Ion Irradiation of Pristine $MoSe_2$

FIB-based material processing is a widely used technique with a broad range of applications for site-specific modification, deposition, imaging, and sputtering of materials; a technique that has extended its applicability in many areas as a multifunctional processing method. In its general form FIB machines are very similar to SEM microscopes in many ways with a major difference: SEM uses a focused beam of "electrons" (mostly for imaging purposes), while a FIB setup uses a focused beam of "ions" that can offer extra functionalities beyond imaging. However, current state-of-the-art FIB systems are mostly designed in a dual-column architecture, one column dedicated to the ion beam and the other column to the electron beam. Access to both electron and ion beams in one apparatus enables the sequential modification (e.g., using ion beam) and imaging (e.g., using electron beam). Such a combination can lend itself to a wide range of application such elemental tomography, supervised etching, and ion/electron beam induced surface modifications.

The ion source is an indispensable part of any FIB microscope. Liquid metal ion sources are very common in which a metal reservoir (typically gallium (Ga)) is placed in direct contact with a heating needle (typically tungsten) to melt the metal source and wet the needle. The radius of the metal cone, which forms at the tip of the needle, can be as small as a few nanometers, offering an extremely tight spatial resolution for material imaging/processing using FIB. Following the formation of the sharp tip, the field-ionization of Ga (upon the exertion of a strong electric field) generates the ion beam. Ion

sources are then accelerated and focused onto the sample using electrostatic lenses. The FIB machine used in our experiments is a dual-column FEI microscope that uses Ga ions accelerated at 30 keV with an adjustable current ranging from 1pA to 30 nA. The beam dosage can be changed in multiple ways such as changing the beam current, per-pixel dwell time, or by changing the number of the overwriting cycles in a loop-writing mode.

To elaborate the impact of the ion irradiation on monolayer $MoSe_2$ crystals, we irradiate several regions of a pristine $MoSe_2$ triangle with different ion dosages and study the exposed regions from multiple angles. Increasing the irradiation dosage changes the optical contrast between the ion-exposed and pristine regions, offering a fast means for distinguishing irradiated regions in the matrix of a pristine $MoSe_2$ film. We further studied the properties of the ion-irradiated regions using PL and Raman measurements. As shown in Figure 5-1 (a), $MoSe_2$ emission is significantly quenched in irradiated regions, primarily because optically generated carriers recombine non-radiatively in ion-beam-induced traps and crystal defects. Raman measurements further support the possibility of structural deformation in $MoSe_2$ crystals following the ion-beam irradiation. As depicted in Figure 5-1(b), the intensity of the characteristic A_{1g} vibration mode at ~ 241 cm^{-1} gradually drops as the irradiation dosage is increased. Moreover, alongside the intensity drop, the A_{1g} resonance undergoes a significant redshift and linewidth broadening (Figure 5-1(c)), both of which hint irradiation-induced structural defects and crystal deformations. Thus, the combination of the performed optical characterizations coherently attests that FIB can be used for the controlled introduction of site-specific defects and structural modifications in pristine $MoSe_2$ crystals, a point that we will later use for the synthesis of lateral junctions.

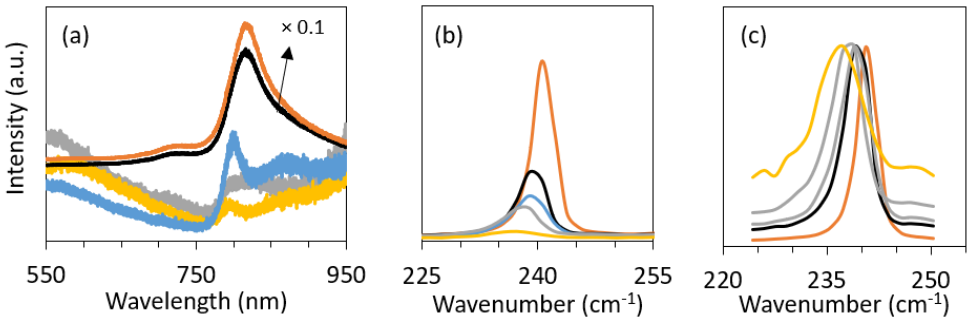

Figure 5-1: FIB-induced introduction of structural deformation in pristine $MoSe_2$ crystals. (a) PL spectra obtained from regions irradiated with different ion dosages. (b) A_{1g} Raman mode of $MoSe_2$ for different ion dosages, which shows a constant intensity drop as the ion dosage increases. (c) Normalized A_{1g} Raman mode shows a significant redshift and linewidth broadening in irradiated regions.

5.2 Sulfurization Procedure

After establishing the FIB irradiation condition, we carried out a set of systematic experiments to develop a sulfurization process that can selectively target the irradiated regions without affecting the pristine $MoSe_2$ matrix. As indicated in Raman spectra in Figure 5-2 (a), after sulfurization, the A_{1g} vibrational mode of $MoSe_2$ in the irradiated region is completely disappeared and, instead, the A_{1g} and E_{2g} modes of MoS_2 appeared, decisively confirming the Se-S substitution in the irradiated regions. In contrast, the A_{1g} mode of $MoSe_2$ in pristine regions has remained largely intact, implying that the composition of the lattice is not altered in those regions. Therefore, the selective Se-S substitution in irradiated regions transforms the defective – pristine $MoSe_2$ pairs into MoS_2 – $MoSe_2$ lateral HSs. Similarly, as shown in Figure 5-2(b), after sulfurization of the sample, the ion-irradiated region demonstrates a strong PL emission centered at ~ 1.85 eV, which corresponds to the well-known MoS_2 bandgap, further confirming the successful S-Se substitution and the formation of a lateral junction between MoS_2 – $MoSe_2$.

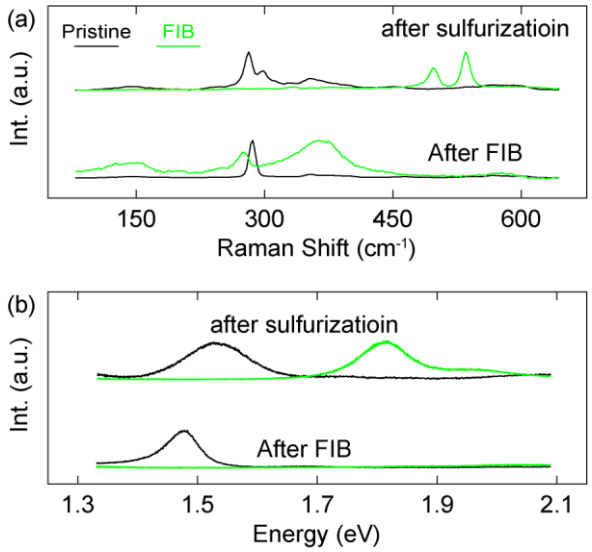

Figure 5-2: Selective chalcogen substitution in ion-irradiated regions. (a, b) Raman and PL spectra, respectively, of pristine and FIB irradiated regions before (bottom) and after (top) sulfurization. As evident in both Raman and PL, sulfurization only changes the chemical composition in ion-irradiated regions.

In comparison to the lithography-assisted approach, FIB technique eliminates the incorporation of hard masks (i.e., SiO_2) into the HS synthesis process. This change offers multiple important advantages. First and foremost, in the absence of SiO_2 masks, both sides of lateral junctions are immediately accessible for the placement of electrical contacts and device fabrication. Previously, access to the $MoSe_2$ side of the junction was blocked by the SiO_2 protection masks. Second, several fabrication steps including EBL lithography, oxide deposition, and overnight lift-off processes are eliminated, leading to a significant increase in the yield of lateral HS synthesis and subsequent device fabrication. Third, our SEM analysis shows that sulfurization of ion-irradiated CVD monolayers yields seamless crystals, meaning that the cracking issue that we discussed in previous chapters is successfully addressed in the FIB-assisted method. Therefore, in addition to the exfoliated films, CVD-grown monolayer $MoSe_2$ films can be used for the fabrication of devices based on lateral HSs, further improving the yield of device fabrication.

CHAPTER 6. ENHANCING LIGHT-2D MATERIAL INTERACTION IN HYBRID STRUCUTRES

Majority of the intriguing properties of 2D TMDs stem from their reduced dimensions to atomic scales. The formation of a direct optical bandgap, pronounced excitonic behavior, and robust mechanical strength are examples of properties that directly rely on the atomically thin nature of TMDs. However, along such unique advantages come some inherent shortcomings. Above all, the interaction of light with such thin films is relatively inefficient, primarily because the effective light-matter interaction length in a film thinner than 1nm is extremely small. This shortcoming has hindered the practical use of 2D TMDs in real world applications especially in designing LEDs, lasers, and photodetectors. In fact, because of the small material volume, generated light by 2D TMDs are often dim, and light-to-electricity-conversion efficiency of reported photodetectors are far below thresholds for practical applications. Thus, to address this shortcoming, the interaction of light with 2D TMDs needs to be enhanced.

In this chapter, I will discuss and implement two strategies for enhancing the light interaction with 2D materials: (i) integration with optical cavities (section6.1) and (ii) integration with plasmonic resonators (section 6.2). The major advantage of the first approach is the small optical mode volume of plasmonic resonators. In contrast, second approach offers much larger enhancement, primarily because photonic resonant structures offer larger quality factors at their resonance wavelength. We also discuss the optical heat generation in TMDs as a side effect, when atomically thin TMDs are integrated with such resonant structures.

6.1 Integration of 2D TMDs with Optical Cavities

Hybrid structures based on integration 2D TMDs with optical resonators have earned significant attention, primarily because the enhanced interaction of light with 2D materials in such hybrid structures can enable devices such as efficient light-emitting diodes and lasers. However, one of the factors affecting the performance of such devices is the effect of the optically induced heat on the optoelectronic properties of the 2D materials. In this section, we first systematically study the enhancement of light interaction with 2D TMDs and then investigate principal roots of heat generation in such hybrid cavity-coupled 2D films under optical pumping. The optical resonator exploited here is a Fabry-Perot (FP) resonator, which can enhance the light-MoS_2 interaction by a significant factor of 60 at its resonance wavelength. We have combined an accurate theoretical modeling with experimental Raman spectroscopy to unravel entangled roots of heat generation in MoS_2 films integrated with FP resonators.

Our investigations reveal that the strong modulation of light absorption in the MoS_2 film, induced by excitation of FP cavity at its resonant frequency, plays the primary role in excess heat generation in 2D material. Furthermore, through varying the cavity length, we show that on-resonance and off-resonance excitation of cavity results in completely different temperature profiles in the cavity coupled MoS_2. Also, by changing the resonance medium of the FP cavity (SiO_2 and air), we consider the role of the heat sinking effect of the substrate in heat generation in MoS_2 films. In our study, the temperature-dependent redshift of the Raman spectra is employed to monitor the local temperature of the MoS_2 films. Our results show the importance of the heating effect in such hybrid structures and

represent a step forward for the design of practical hybrid optical devices based on layered semiconducting 2D materials.

6.1.1 Characterization Approach

High-quality MoS_2 films were grown by direct sulfurization of molybdenum (Mo) thin films. [1] Briefly, a layer of 1 nm-thick Mo film was deposited on a 260 nm-thick SiO_2 film on a Si substrate using an electron-beam evaporator and, then, the sample was placed in a furnace and exposed to a controlled flow of the sulfur gas at the temperature of 1050 ^{0}C for uniform growth of MoS_2 on a large area. Following gradual cooling to 300 ^{0}C, the sample was taken out of the furnace. Using atomic force microscopy (not shown here), we identified the thickness of the as-prepared films to be 2.1 nm, which is equivalent to the height of a trilayer MoS_2 film. The MoS_2 film was then transferred onto new substrates through a standard wet-transfer technique. Our PL spectroscopy verifies similar excitonic emission spectrum of the as-synthesized trilayer MoS_2 films and chemical vapor deposition (CVD) grown MoS_2.

As we have shown in Figure 6-1, Raman spectroscopy was used to characterize the light-MoS_2 interaction as well as monitoring laser-induced heat generation in MoS_2 films integrated on FP resonators (referred to as MoS_2-on-FP). This selection is motivated by the fact that Raman signal strongly sensitive to the temperature variation. [2-5] Increasing the temperature through changing the effective binding length of vibrating molecules reduces the restoring force and softens the vibration strength. [3, 4] Furthermore, at elevated temperatures, the vibration of the molecules might not be modeled as a simple harmonic oscillator. Instead, for a complete description, contribution of non-harmonic vibrations

should also be taken into account, [2, 3] which in turn contributes to the softening of the vibrations. These two effects cause red-shift and broadening of the Raman spectrum as the temperature increases.

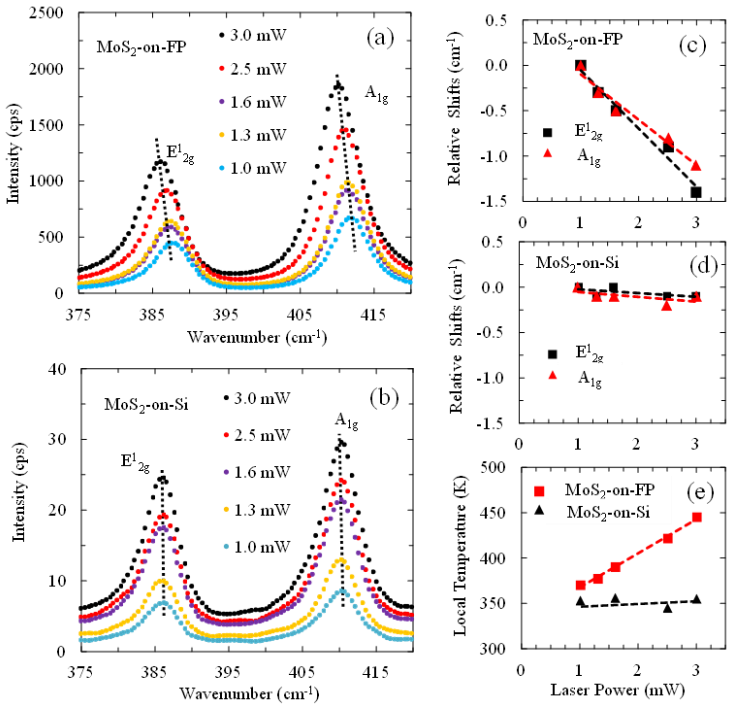

Figure 6-1: Effect of coupling to the FP cavity on laser-induced thermal heating of the MoS_2 films. Raman spectra are recorded at different laser powers ranging from 1 mW to 3 mW for (a) MoS_2-on-FP resonator (i.e., 256 nm SiO_2 on Si substrate) and (b) MoS_2-on-Si sample. The in-plane (E^1_{2g}) and out-of-plane (A_{1g}) characteristic resonances of the MoS_2 film are marked on the plots. Dashed lines are guides to eye connecting peak positions of the E^1_{2g} and A_{1g} resonances at different laser power. Peak positions of the A_{1g} and E^1_{2g} features manifest a linear red-shift by increasing power of the excitation laser as shown in panels (c) and (d) for the MoS_2-on-FP and MoS_2-on-Si samples, respectively. (e) Local temperature of the MoS_2 film at different laser powers, calculated from the ratio of Stokes to anti-Stokes integrated intensities of E^1_{2g} feature. The dashed lines are least square linear fits to the experimental data.

Figure 6-1 (a)-(b) show the Raman spectra of the MoS_2-on-FP sample (256 nm SiO_2/Si) and on a bare Si substrate (referred to as MoS_2-on-Si), respectively, measured at several laser powers ranging from 1 mW to 3 mW at the pump wavelength of 488 nm. Note that the minimum laser power is chosen so that the signal-to-noise ratio of the Raman signal

on the Si substrate is high enough for reliable measurements, and the maximum laser power is chosen to avoid a permanent damage to the MoS_2 film integrated on the FP resonators. In all measurements, the wavelength of the excitation laser is kept fixed at 488 nm. In these Raman spectra, the two prominent in-plane (E^1_{2g}) and out-of-plane (A_{1g}) vibrations of the MoS_2 films are observable. By fitting Lorentzian functions to the experimentally acquired spectra, the peak positions and linewidths are extracted at different laser powers. Figure 6-1**Error! Reference source not found.**(c)-(d) show that by increasing the excitation power, the E^1_{2g} and A_{1g} Raman peaks experience linear redshifts accompanied with linewidth broadening. However, a key observation here is that the Raman spectrum of the MoS_2-on-FP sample undergoes a remarkably larger red-shift as compared to that of the MoS_2-on-Si sample. This distinction can be inferred by looking at the slope of the E^1_{2g} (A_{1g}) red-shift of the MoS_2-on-FP sample, $\chi_{E^1_{2g}}$ = - 0.64 cm^{-1}/mW ($\chi_{A_{1g}}$ = - 0.47 cm^{-1}/mW), which is about one order of magnitude larger than that of the MoS_2-on-Si sample (i.e., $\chi_{E^1_{2g}}$ = - 0.05 cm^{-1}/mW ($\chi_{A_{1g}}$ = - 0.06 cm^{-1}/mW)). This effect was investigated more precisely by calculating the local temperature of the MoS_2 film on the two substrates (Figure 6-1 (e)) at different excitation laser powers. Here, the local temperature of the MoS_2 film is estimated using the following equation [2]:

$$\frac{I_S}{I_{AS}} = \kappa \, exp\left(\frac{\hbar\omega}{K_B T}\right), \qquad (6\text{-}1)$$

where I_S and I_{AS} are the integrated intensities of Stokes and anti-Stokes components of the E^1_{2g} resonance. In Equation (6-1), $\hbar\omega$, K_B, and T are the vibration energy of the E^1_{2g} resonance, Boltzmann constant, and the local temperature of the MoS_2, respectively. Also, κ is a pre-factor that accounts for absorption coefficients and scattering cross sections of

the Stokes, anti-Stokes, and the incident light components in the MoS_2 film. We note that we have chosen the E^1_{2g} resonance because coupling between optically generated electrons and phonons for this vibration mode is negligible, [6] and the observed changes in the Raman spectra can safely be attributed to the heating effects only.

Figure 6-1 (e) indicates two important facts: i) increasing the excitation laser power linearly increases the local temperature of the MoS_2 film. This suggests that laser-induced thermal heating is the origin of the redshift observed in the Raman spectra, which is in agreement with previous reports. [4, 5] ii) Excited at identical laser powers, the local temperature of the MoS_2-on-FP sample is significantly higher than that of the MoS_2-on-Si sample, which emphasizes the stronger redshift of the Raman spectrum observed on the FP resonator compared to that on the Si substrate. As Figure 6-1(e) shows, the variation of the local temperature caused by varying the excitation laser power is very small for MoS_2-on-Si sample, while it has a linear behavior with a slope of +37 K/mW for the MoS_2-on-FP sample. Indeed, excitation of the MoS_2 film on the FP resonator causes excess heating and yields a stronger redshift.

6.1.2 Coupling of 2D MoS_2 to FP Cavity

Two phenomena might contribute to the differences observed in Figure 6-1(e): i) different thermal conductivities of the substrate materials underneath the MoS_2 films (i.e., SiO_2 versus Si), and ii) enhanced light-MoS_2 interaction in the vicinity of the FP-cavity. Since the thermal conductivity of SiO_2 is lower than that of Si, the generated heat in the MoS_2-on-FP sample dissipates slower, resulting, in part, in increasing the local temperature. On the other hand, field enhancement induced by the constructive interference

of light in the FP resonator enhances light interaction with the MoS_2 film integrated on the FP resonator and builds up more heat. The strength of this effect can be more appreciated by noting that maximum intensity of the Raman signal of the MoS_2-on-FP sample is about 45 times higher than that of the MoS_2-on-Si sample (Figure 6-1 (a)-(b)). To identify the contribution of these two effects, by controlling the FP cavity length (i.e., thickness of the SiO_2 layer), we establish several FP resonators with different Raman enhancement strengths and repeat experiments similar to those explained in Figure 6-1. This allows exploring the sole role of the enhanced light interaction in the generation of excess heat in the MoS_2-on-FP sample while keeping the heat sinking property of the substrate in all samples are rather similar.

It is worth mentioning that the dependence of the thermal conductivity of a SiO_2 thin film on film thickness is essentially negligible if the film is thicker than approximately 150-200 nm. [7] Therefore, to avoid different heat sinking effects from the substrate, the SiO_2 layers of all the FP resonators are designed to be thicker than 200 nm. Figure 6-2(a)-(b) represents variation of the E^1_{2g} and A_{1g} red-shifts with laser power at three FP cavity lengths of 197 nm, 256 nm, and 273 nm along with that of the MoS_2-on-Si sample. Our later discussions clarify the rationale behind choosing these specific thicknesses. The results shown in Figure 6-2 were obtained by measuring relative shifts in the peak positions of the E^1_{2g} and A_{1g} resonances at different excitation laser powers with respect to peak positions at 1mW laser power. As is evident from Figure 6-2, changing the thickness of the SiO_2 slab varies the slope of the red-shift in the Raman spectrum, which is a manifestation of the increase in laser-induced heating of MoS_2. This observation is an indication of

changing the strength of the laser light interaction with changing the FP resonance wavelength, which is dictated by the length of the cavity as will be explained later.

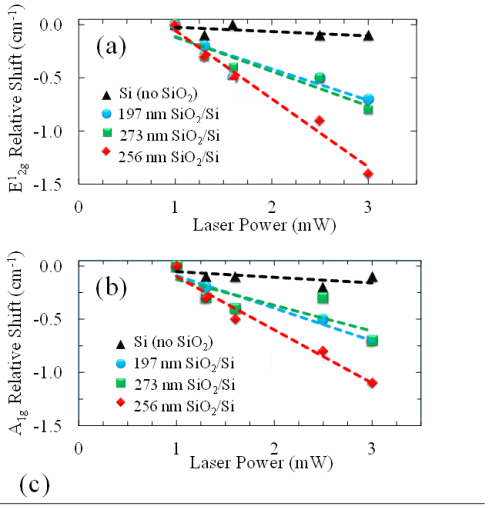

(c)

Substrate	$\chi_{E^1_{2g}}$ (cm^{-1}/mW)	$\chi_{A_{1g}}$ (cm^{-1}/mW)
Si (no SiO_2)	-0.05	-0.06
197 nm SiO_2/Si	-0.27	-0.26
273 nm SiO_2/Si	-0.31	-0.26
256 nm SiO_2/Si	-0.64	-0.47

Figure 6-2: Effect of the FP cavity length on heat generation. Variation of the red-shift experienced by (a) E^1_{2g} and (b) A_{1g} vibrations of tri-layer MoS_2-on-FP sample through changing cavity length (i.e., thickness of the SiO_2 slab). For the sake of comparison, redshift of E^1_{2g} and A_{1g} resonances on Si substrate (no SiO_2) at different laser powers are also represented. Symbols are experimental results and dashed lines are linear fits. (c) Quantitative values for the slopes of the MoS_2 Raman redshifts on different substrates are tabulated for E^1_{2g} (i.e., $\boldsymbol{\chi_{E^1_{2g}}}$) and A_{1g} (i.e., $\boldsymbol{\chi_{A_{1g}}}$) resonances. Negative signs of the slopes are an indication of the redshift.

Slopes of the red-shifts for E^1_{2g} (i.e., $\chi_{E^1_{2g}}$) and A_{1g} (i.e., $\chi_{A_{1g}}$) resonances on different substrates are extracted by fitting linear trends to the experimental results in Figure 6-2(a)-(b), and the quantitative values of the slopes are tabulated as shown in Figure 6-2(c). Notice that negative signs of the slopes point to the redshift of the resonances. Numerical values reveal that both $\chi_{E^1_{2g}}$ and $\chi_{A_{1g}}$ are considerably larger for the case where FP is excited on-

resonance (i.e., cavity length of 256 nm) as compared to the off-resonance cases (i.e., cavity lengths of 197 nm and 273 nm). To interpret these differences, we study the effect of varying SiO_2 thickness on the interference of light inside the FP cavity and its effect on modulation of light interaction with the MoS_2 film through a numerical model based on successive reflections of light from the boundaries of the SiO_2 slab (as shown in **Error! R eference source not found.**(a)), which is formulated by Li et al. [8] The mathematical modeling of light-MoS_2 interaction is presented in Appendix A.

As a figure of merit, we define the total enhancement factor (TEF) as the ratio of the maximum intensity of the E^1_{2g} Raman peak of the MoS_2-on-FP samples ($I_{max, FP}$) to that of the MoS_2-on-Si sample ($I_{max, Si}$), that is TEF = $I_{max, FP}$ / $I_{max, Si}$. The map of Figure 6-3(b) illustrates the results of this modeling for trilayer MoS_2 films integrated on FP resonators with various SiO_2 thicknesses while the excitation laser wavelength varies between 380 nm and 900 nm. In this map, at a fixed SiO_2 thickness, the wavelength-dependent enhancement profile illustrates irregularities that originate from the combined effect of the FP interference and the wavelength-dependent refractive index of the MoS_2 film [8, 9] (see appendix B). At a fixed excitation wavelength, however, the enhancement spectrum periodically depends on the thickness of the SiO_2 layer. Figure 6-3(c) shows the variation of the TEF with the SiO_2 thickness at the excitation wavelength of λ = 488 nm (used in our experiments) associated with the dashed line overlaid on the 2D map of Figure 6-3(b). Figure 6-3(c) suggests that the maximum enhancement can be reached, to the first order approximation, when the SiO_2 thickness is equal to the odd multiples ($2l + 1$) of one quarter of the wavelength in the resonance medium ($\frac{\lambda}{4n}$), that is:

$$d_{l,max} = (2l + 1)\frac{\lambda}{4n}, \qquad (6\text{-}2)$$

where n and l are the refractive index of SiO_2 (~ 1.46) and an integer number (mode index), respectively. However, the fairly large imaginary part of the refractive index of MoS_2 at λ = 488 nm (~ 1.65) gives rise to a reflection phase addition at the MoS_2/SiO_2 interface, which is not considered in Equation (6-2). Thereby, a thinner SiO_2 (less than what Equation (6-2) predicts) meets the condition for the maximum enhancement of the E^1_{2g} Raman peak. For example, Equation (6-2) predicts $d_{l\,=\,0,max} = 83$ nm, while the results of more complete modeling determine an optimal thickness of 67 nm. Nevertheless, Equation (6-2) clearly elucidates the periodic dependence of the TEF on the SiO_2 thickness with a period of $\frac{\lambda}{2n}$ = 167 nm, very close to 165 nm that the results of modeling (Figure 6-3) predicts. To verify accuracy of our modeling, Figure 6-3(c) represents the experimentally measured TEFs (square symbols) for the three MoS_2-on-FP samples (used in the Raman measurements of Figure 6-3). Good agreement between the simulation and the experimental results for the three samples are evident from Figure 6-3(c). Notice that 5-7 cm^{-1} linewidth of the E^1_{2g} Raman resonance is equivalent to less than 1 nm spectral width. Therefore, we can safely assume that the entire E^1_{2g} resonance spectrum gains an identical enhancement and variation of the TEF over the Raman linewidth is negligible. Detailed discussion regarding the effect of the MoS_2 thickness on the TEF is presented in the Appendix B.

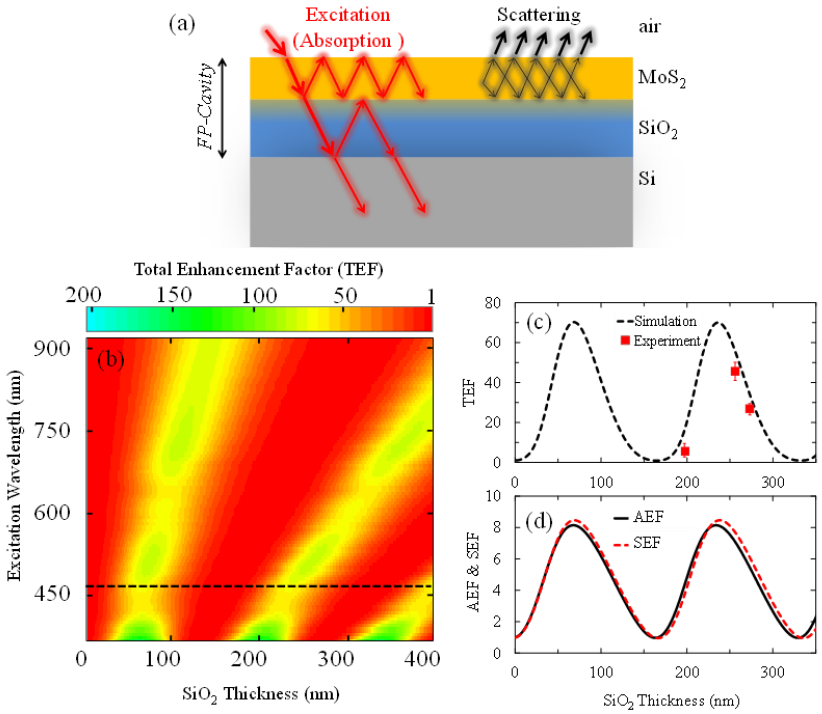

Figure 6-3: The enhanced light-MoS_2 interaction on the FP cavity. (a) The schematic illustration of the cavity structure. The ray trace shows the propagation of light beams inside the cavity. (b) Simulation results representing the enhancement of the E^1_{2g} Raman signal of the MoS_2-on-FP sample as a function of the SiO_2 thickness (cavity length) and the wavelength of the excitation laser. The color-bar represents the enhancement factor. (c) The enhancement spectra at 488 nm excitation wavelength (used in our experiments) for a trilayer MoS_2 film on the SiO_2 substrate (corresponding to the dashed line in panel (b)). Squares represent the experimental results. (d) The separate contribution of the improved light absorption (i.e., AEF) and light scattering (i.e., SEF), as represented in the schematic illustration of part (a) to the total enhancement of E^1_{2g} Raman signal (i.e., TEF) at the 488 nm excitation wavelength.

Comparing the TEF of the E^1_{2g} peak intensity of MoS_2 on different FP resonators (Figure 6-3 (c)) with the slope of the redshift of the E^1_{2g} resonance (as an indication of the local temperature) on corresponding substrates (Figure 6-2 (a)) provides insightful information. FP-cavities with 197 nm, 256 nm, and 273 nm SiO_2 thicknesses provide TEFs of 5.6, 45.6, and 26.9 for the E^1_{2g} resonance, respectively. The corresponding $\chi_{E^1_{2g}}$s on these substrates are – 0.27 cm^{-1}/mW, – 0.64 cm^{-1}/mW, and – 0.32 cm^{-1}/mW, respectively. In other words, the higher the TEF, the larger the slope of the redshift of the Raman spectra.

This confirms the principal role of the enhanced interaction of light with MoS_2 on excess heat generation. However, although the TEF on the FP resonator with 256 nm SiO_2 is more than 8 times larger than that on the FP resonator with 197 nm SiO_2, the slope of the red-shift on 256 nm SiO_2 substrate is only 2 times larger than that of the resonator with 197 nm SiO_2 thickness. More interestingly, the FP cavity with the SiO_2 thickness of 273 nm provides a TEF of approximately 5 times larger than that on the FP cavity with 197 nm SiO_2 thickness, while the slope of the red-shift on the 273 nm SiO_2 resonator is just slightly larger than that of the 197 nm SiO_2 resonator.

The inconsistency between the TEFs and the redshifts of the E^1_{2g} resonance can be resolved by considering details of the enhancement mechanism. Improvement of the Raman intensity of the MoS_2-on-FP samples has two roots: (1) enhancement of the MoS_2 excitation (equivalently, light absorption) and (2) enhancement of the Raman scattering (emission) from the MoS_2 film (see Figure 6-3(a)). Combination of the improved excitation and emission contribute to the enhancement of the Raman signal of the MoS_2-on-FP sample and determines the TEF. However, the heat generation is primarily entangled with the enhancement of the light absorption. Therefore, we need to introduce two separate enhancement factors: absorption enhancement factor (AEF) and scattering enhancement factor (SEF). In Figure 6-3(d), we present dependence of these two factors on the thickness of the SiO_2 cavity at excitation wavelength of 488nm (see Appendix A for details). In these calculations, AEF and SEF are computed by dividing, respectively, the absorption and scattering components of the Raman signal of the MoS_2-on-FP samples to the corresponding components of the MoS_2-on-Si sample. Figure 6-3(d) shows that the AEF and SEF have similar profiles with maximum enhancement factors of approximately 8.

This general resemblance is due to the small energy exchange upon E^1_{2g} Raman scattering that results in small wavelength shift between incoming and scattered light and, thus, leads to similar FP cavity response for the excitation and scattering signals. However, since the wavelength of the scattered light is slightly longer than that of the incoming light (Stokes shift), based on Equation (6-2), the maximum enhancement for the scattering profile occurs at a slightly thicker SiO_2 layer than that for the absorption profile in Figure 6-3(d). Further minute differences between the absorption and scattering spectra, in Figure 6-3(d), can be related to the wavelength dependent reflection of light (for the incoming and scattered light) at the MoS_2-SiO_2 boundary caused by the dependence of the refractive index of MoS_2 on wavelength.

Figure 6-3 (d) shows that for MoS_2-on-FP samples with SiO_2 thicknesses of 197 nm, 256 nm, and 273 nm, light absorption by MoS_2 gains enhancement factors of AEF = 3.9, 7.3, and 4.3, respectively. Comparing these values with the slope of the red-shift on the corresponding substrates (Figure 6-2 (c)) reveals that the trend of the red-shift agrees well with the trend of the absorption enhancement. For example, the AEF for the FP resonator with 256 nm SiO_2 layer is approximately twice that for the resonator with 197 nm SiO_2, which is consistent with the slope of the E^1_{2g} redshifts on these two samples. Likewise, approximately similar absorption enhancement on resonators with 197 nm and 273 nm SiO_2 layers is consistent with rather identical slopes for the E^1_{2g} redshifts of the Raman resonances on these substrates. These observations suggest that modulation of the light absorption (not the total enhancement) is the underlying mechanism for the excess heat generation in MoS_2-on-FP structures, which manifests itself in the amount of the red-shift observed in the Raman spectra. Therefore, the in-resonance excitation of the FP cavity (as

in sample with 256 nm SiO_2 layer) increases the MoS_2 temperature significantly more than the off-resonance excitation (as in samples with 197 and 273 nm SiO_2 layers).

6.1.3 Spatial Modulation of Light-2D Material Interaction

Another phenomenon that affects heating in the integrated 2D materials on resonators is the heat conductivity of the substrate (or the substrate heat sinking effect). To study this effect, we etch an array of holes with diameters of 4-5 μm into the 256 nm-thick SiO_2 on Si substrate, and then, suspend the trilayer MoS_2 film over it (Figure 6-4 (a)) to establish two types of FP resonators that are spatially adjacent: one resonator has a 256 nm air-gap as the resonance medium (i.e., the suspended MoS_2 region over the holes) and the other one has a 256 nm SiO_2 as the resonance medium (i.e. the supported MoS_2 regions outside the holes). In these two types of resonators, different thermal conductivities of the air and SiO_2 allow investigating the strength of the heat sinking effect of the substrate on heat generation in MoS_2 film.

We map the Raman spectrum of the MoS_2 across a line passing over one of the holes, at a fixed laser power of 3 mW, and record the Stokes and anti-Stokes spectra. Figure 6-4(b) illustrates the map of Stokes Raman spectra at different positions, where the dashed lines mark the peak positions of the E^1_{2g} and A_{1g} vibrations and the solid vertical lines outline edges of the hole, where MoS_2 is suspended. In order to monitor the evolution of the E^1_{2g} and A_{1g} resonances, we pick vibration frequencies of a point outside the hole as the reference to measure the relative shifts of the E^1_{2g} and A_{1g} resonances along the scanned line (Figure 6-4 (c)). Results show that by moving from a point outside the hole toward the center of the hole, both vibrations experience symmetric blue-shifts and reach their maxima

at the center of the hole. Also, in Figure 6-4(d), we have estimated spatial temperature profile (based on Equation (6-1)) along the scanned line where local temperature of the MoS_2 film drops from an average value of 432 K over the SiO_2-supported regions to 380 K over the suspended regions. Therefore, the blueshifts observed in Figure 6-4(c) are due to the lower local temperature of the suspended MoS_2.

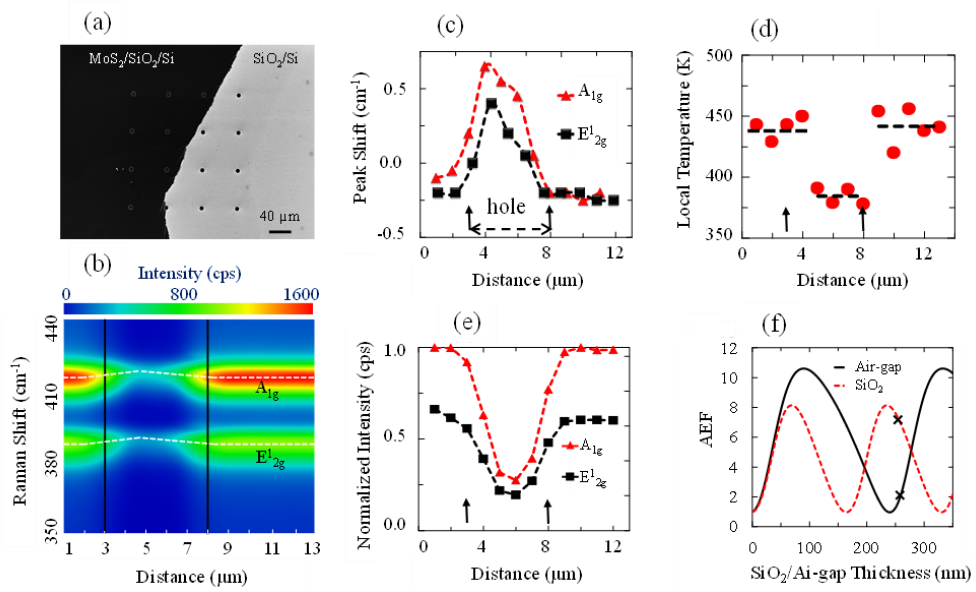

Figure 6-4: Spatial modulation of light-2D material interaction. (a) SEM image of the trilayer MoS_2 film suspended over an array of holes etched into a 256 nm thick SiO_2 layer on Si substrate. The darker region is covered with MoS_2. (b) Raman mapping across a line passing over a hole in (a). Horizontal dashed lines are guides to the eyes showing Raman peak positions. Vertical lines depict edges of the hole. (c) Relative change of the A_{1g} and E^1_{2g} peak positions across the scanned line compared to a reference point outside the hole. Dashed lines are guides to the eyes. The arrows show the extent of the hole. (d) Spatial temperature profile across the scanned line. Three regions are distinguishable: suspended MoS_2 at the middle and SiO_2-supported MoS_2 at the left and right regions. Dashed lines show the average temperature at each region. The arrows show the extent of the hole. (e) Normalized intensity of the A_{1g} and E^1_{2g} across the scanned line. Dashed lines are guides to the eyes. The arrows show the extent of the hole. (f) Comparing enhancement of light absorption (i.e., AEF) in the MoS_2 film integrated on SiO_2 (dashed line) and air-gap (solid line) FP cavities. The crosses mark the values for the cavity length of 256 nm, which is used in our experiment.

Figure 6-4 (e) depicts the normalized Raman scattering intensities corresponding to the E^1_{2g} and A_{1g} vibrations, where both manifest symmetric drops moving toward the center of the hole, indicating weaker light-matter interaction in the suspended MoS_2 regions compared to that of the SiO_2-supported regions. In fact, despite the better thermal conductivity of SiO_2 compared to the air, stronger light-MoS_2 interaction in SiO_2 supported regions elevates the MoS_2 temperature outside the holes and creates the temperature profile of Figure 6-4(d) and (as a direct result) the blue-shift profile of Figure 6-4(c). To verify this claim, in Figure 6-4(f), we have compared AEFs of FP resonators having either air-gap or SiO_2 as the resonance medium through the same method used above. In Figure 6-4(f), owing to the larger refractive index of the SiO_2, the maximum absorption enhancement can be reached at a shorter cavity length (compared to the air-gap FP resonator) as predicted by Equation (5-2). Also, maximum achievable AEF on the air-gap resonator (~ 11) is larger than that over the SiO_2 resonator (~ 8). This effect can be explained on the basis of the refractive index contrast at the upper (i.e., MoS_2-SiO_2/air) and lower (Si-SiO_2/air) boundaries of the two types of FP cavities. Higher refractive index contrast provides larger reflection coefficients at the two boundaries and increases the quality factor of the cavity. Therefore, knowing that the refractive index contrasts at both upper and lower boundaries are larger for the air-gap cavity compared to the SiO_2 cavity, we expect a higher quality factor for the former resonator. Thus, potentially, air-gap resonator enables stronger light-MoS_2 interaction than the resonators having SiO_2 as the resonance medium. However, for the specific cavity length of 256 nm (used in the analysis of Figure 6-4), the AEFs are 7.4 and 1.4 over the SiO_2-supported and air-gap FP resonators, respectively (as marked by two crosses in Figure 6-4(f)). This is primarily due to the

existence of a FP cavity mode in the SiO_2 resonator at the excitation wavelength of 488 nm and lack of such a mode in the air-gap cavity. In other words, while excitation at 488 nm wavelength is on-resonance for SiO_2 FP cavity, it is an off-resonance excitation for air-gap FP cavity. Therefore, illuminated at identical laser powers, a greater portion of light gets absorbed by MoS_2 films integrated over the SiO_2 FP resonator compared to that over the air-gap resonator, which generates the temperature profile of Figure 6-4(d). Results of Figure 6-4 demonstrates that effect of absorption modulation can completely overwhelm the heat sinking effect of the substrate material and governs the heat generation upon coupling of the 2D materials to the optical cavities. It can also be inferred that by selecting the proper cavity length for the SiO_2 and air-gap resonators, a large range of performance variations can be achieved.

Our study clearly highlights the importance of the enhanced light-mater interaction as well the thermal effects that comes along such a pronounced interaction. These thermal effects are inherent in the optical characterization of resonance-enhanced phenomena in hybrid integration of 2D materials with photonic (or plasmonic) structures. Thus, extreme care must be given to the interpretation of the experimental results in such studies by decoupling the light-induced thermal effects (that usually result in changing the temperature distribution over the 2D material) from the other (desired) effects.

In addition to its importance in proper interpretation of the experimental results, the outcomes of this paper can be useful from practical perspective, especially for energy harvesting applications. As an example, the spatial modulation of the light absorption in MoS_2 through substrate engineering can be exploited for artificial generation of a temperature gradient (as in Figure 6-4(d)). Knowing that MoS_2 has a large Seebeck

coefficient (up to 30 mV/K), this temperature gradient can be converted into an electric signal (e.g., voltage) by application of two electrodes (e.g., indium-tin-oxide (ITO)) at cold and hot regions. Indeed, through a photo-thermo-electric conversion chain, light generates a temperature gradient (e.g., 50 K in Figure 6-4(d)) that can be converted into a voltage difference through the Seebeck effect (e.g., between the hole center and the surrounding region in Figure 6-4(a)). This effect can be optimized by engineering the shape and distribution of the holes in Figure 6-4(a). A separate study is currently underway to explore the practical prospects of this idea.

6.2 Integration of 2D TMDs with Plasmonic Resonators

In this section, through the integration of a strongly coupled plasmonic nanoantenna array with a monolayer $MoSe_2$, spatial maps of the photoluminescence (PL) are acquired on- and off-resonance to exhibit the role of the lattice plasmon modes on the enhancement of the PL from the $MoSe_2$ monolayer. The on-resonance excitation of the hybrid nanostructure at 785 nm reveals a significant PL enhancement of more than 25 (compared to the PL enhancement factor that a Fabry-Perot resonance provides), while the off-resonance excitation at 488 nm only results in an enhancement factor of five. Polarization-resolved optical reflection spectroscopy is also experimented to verify the role of the coupled nanoantenna array on the PL enhancement. Full-wave numerical simulations of the complete structure are also performed to support the observed experimental results. These findings enrich our knowledge regarding the light interaction with 2D materials mediated by plasmonic nanostructures and pave the way for the design of a new class of hybrid 2D material plasmonic devices that utilize enhanced light-matter interaction.

6.2.1 Fabrication of Hybrid Plasmonic-$MoSe_2$ Structures

High-quality $MoSe_2$ layers, used in this research, were grown on a 290 nm-thick layer of thermally grown silicon dioxide (SiO_2) on a silicon (Si) substrate using the CVD technique, as reported previously. [10, 11] Using Raman spectroscopy, monolayer regions of $MoSe_2$ were identified and were used for integration with plasmonic nanostructures. To enhance the PL emission of monolayer $MoSe_2$, we designed and integrated a set of plasmonic nanostructures, each supporting lattice plasmon (LP) modes near the direct band gap of the $MoSe_2$ monolayer. Lattice plasmon waves are propagating electromagnetic modes that are formed by the interaction between the localized surface plasmon polaritons (LSPPs) and the Bragg scattering in a periodic plasmonic structure.[12] LP modes have been used to enhance the light-matter interaction for different applications [13–15]. In our research, the designed plasmonic nanostructures are composed of two sets of horizontally and vertically oriented Au nanorods with the fixed width and thickness of, respectively, w = 30 nm and t = 30 nm and inter-antenna spacing (or period) of a = 250 nm. This particular configuration of nanorods was chosen to induce two wideband LP waves (far from the LP band edge), to enhance both excitation and emission light in both horizontal and vertical polarizations. To find the optimal nanorod length to match the LP resonance and $MoSe_2$ emission wavelengths, we performed a set of full-wave numerical simulations using the FDTD method, taking into account the complex refractive index of ML-$MoSe_2$. [16] In addition, we fabricated several plasmonic arrays with a fixed lattice constant and different nanorod lengths to compensate for anisotropy in the permittivity of $MoSe_2$ that was not included in the numerical modeling.

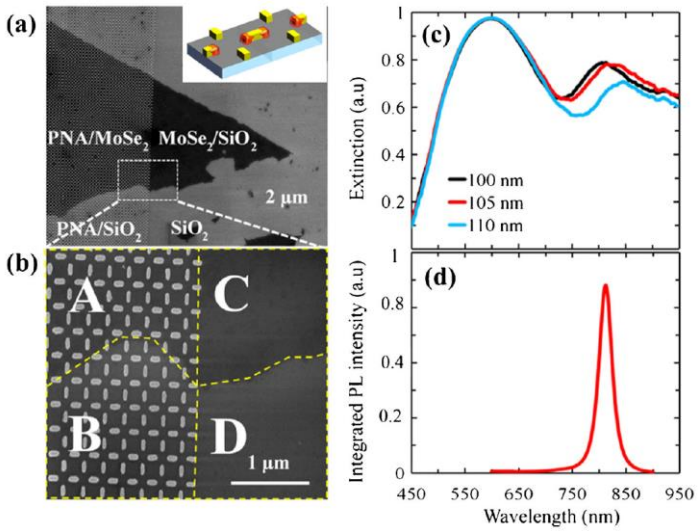

Figure 6-5: Hybrid plasmonic-$MoSe_2$ structures. (a) The SEM image of the structure that integrates the coupled PNA array with a $MoSe_2$ monolayer. The black areas are covered by the $MoSe_2$. The inset shows the three-dimensional schematic of the fabricated PNA composed of two arrays of coupled gold nanorods. (b) A closer look at the selected region in (a). Region A: PNA/$MoSe_2$/SiO_2, Region B: PNA/SiO_2, Region C: $MoSe_2$/SiO_2, and Region D: SiO_2 substrate. Thickness, width, and length of each individual gold nanoantenna are t = 30 nm, w = 30 nm, and l = 105 nm, respectively, with the PNA periodicity of a = 250 nm in both horizontal and vertical directions. (c) Extinction spectra of the hybrid $MoSe_2$-PNA structure (region A) obtained from optical reflection spectroscopy for different nanoantenna lengths of 100, 105, and 110 nm with t = 30 nm, w=30 nm, and a = 250 nm. The two observed resonances in all three spectra correspond to the PNA resonance (peak around 800 nm) and F-P resonance due to the interference of light inside the SiO_2 substrate (peak at around 600 nm). (d) The PL spectrum of the $MoSe_2$ on SiO_2 (region C) with a luminescence peak at 810 nm, which matches with the long-wavelength resonance of the PNA structure with l = 105 nm.

Coupled plasmonic nanoantenna (PNA) (i.e., Au nanostructure) arrays were fabricated using standard electron beam lithography (EBL), metal deposition, and a lift-off process. Figure 6-5(a, b) illustrates representative scanning electron microscopy (SEM) images of the fabricated device. In Figure 6-5(b), four different regions can be distinguished based on the overlap of the plasmonic nanostructure with the $MoSe_2$ monolayer. We refer to these regions as A, B, C, and D throughout the manuscript. In region A, the PNA and monolayer $MoSe_2$ have complete overlap (this is the active region, where the enhancement of light-matter interaction occurs). Regions B and C identify parts of the structure with only PNA

(no $MoSe_2$) and only ML-$MoSe_2$ (no PNA), respectively. Finally, region D identifies the area with bare SiO_2 substrate (no PNA or $MoSe_2$).

To match the resonance of the PNA with the PL peak of the ML-$MoSe_2$, we measured the optical reflection of the hybrid PNA-$MoSe_2$ structure (region A in Figure 6-5(b)) with different nanorod lengths and compared the results with the PL spectra of the bare ML-$MoSe_2$ on SiO_2 (region B in Figure 6-5(b)). Comparing the measured extinction (i.e., change in the optical reflection) for PNAs with different length (Figure 6-5 (c)) and the PL of the ML-$MoSe_2$ (Figure 6-5 (d)) show that for w = 30 nm, t = 30 nm, and a = 250 nm, the optimal length of the gold nanorods in the PNA is l = 105 nm. Note that two distinct peaks are present in the optical reflection spectra of Figure 6-5(c). The first peak at shorter wavelengths (around 600 nm) can be associated to the F-P resonance caused by the interference of the light inside the SiO_2 layer as explained elsewhere. [18] The second peak at longer wavelengths (around 800 nm) corresponds to the plasmonic resonance of the coupled PNA. The second resonance is of interest in this work as it has a good spectral overlap with the measured PL of the ML- $MoSe_2$ (Figure 6-5 (d)).

To investigate the effect of the PNA on the PL enhancement of the $MoSe_2$ film, we conduct spatially resolved PL measurements over the entire region shown in Figure 6-5(a). To highlight the role of the LP modes on modifying the PL of the ML-$MoSe_2$, we performed separate measurements with two excitation wavelengths of 488 nm (off-resonance, Figure 6-5(a, c)) and 785 nm (on-resonance, Figure 6-6(b, d)). The laser power was set to 1mWat both excitation wavelengths and the spot size of the laser was ~1.2 μm. As seen in Figure 6-6(a, b), the PL intensity is enhanced where the ML-$MoSe_2$ is integrated with the PNA (region A). A key observation from Figure 6-6(a, b) is that the PL

enhancement (defined as the ratio of the PL collected from region A to that of region C) is larger when the sample is pumped at a wavelength closer to the PNA resonance (i.e., 785 nm). To quantitatively investigate this observation, in Figure 6-6(c, d), the emission spectra of the ML-$MoSe_2$ with and without the PNA and the resulting PL enhancement spectra are compared. To exclude the spatial variation of the PL intensity in calculation of the enhancement factor, we averaged the spectra over each individual region. For the near-resonance excitation (Figure 6-6 (d)), a notch filter centered at 785 nm was used to block the reflection at the pump wavelength at the output; thus, the measured PL shown in Figure 6-6(d) will be discussed at wavelengths longer than ~800 nm. These results reveal a maximum of 25-fold PL enhancement for near-resonance excitation (Figure 6-6 (d)) as compared to a maximum of 5-fold PL enhancement for the off-resonance excitation (Figure 6-6 (c)).

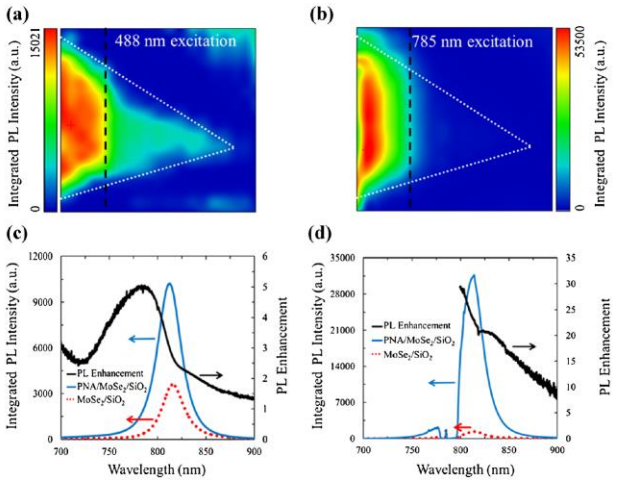

Figure 6-6: Photoluminescence enhancement in Hybrid Plasmonic-$MoSe_2$ structures. PL maps measured at two different excitation wavelengths of (a) 488 nm and (b) 785 nm. Maps are represented at the wavelength of 810 nm (i.e., maximum PL intensity of the $MoSe_2$). The location of the monolayer $MoSe_2$ is outlined by white dotted lines, and the PNA covers the left side of the black dashed line. The PL spectra of the $MoSe_2$ with and without PNA are compared for excitation wavelengths of (c) 488 nm and (d) 785 nm. The PL enhancement factors are calculated and shown on the right vertical axes in (c) and (d). The PL enhancement spectrum for excitation at 785 nm is shown only above 800 nm wavelength, where notch filter on pump does not distort the collected spectrum.

Another interesting observation from Figure 6-6(c, d) is the shift in the location of the PL peak emission wavelength of the ML-$MoSe_2$, when integrated with the PNA. To explain this observation, we numerically estimated the excitation intensity enhancement by the PNA through three-dimensional (3D) full-wave simulation using Lumerical FDTD solution. In this analysis, the dispersive complex refractive index of the 0.7 nm-thick $MoSe_2$ film was modeled by a seventh-order polynomial that was fitted to the experimentally measured wavelength-dependent complex refractive index of the ML-$MoSe_2$ [16]. In this simulation, a single unit cell of the structure (composed of two similar horizontally and vertically oriented Au nanorods) is modeled using the periodic boundary condition on its four sides and perfectly matched layer (PML) boundary condition on the top and bottom of the structure. The structure is excited by a plane wave propagating in the direction normal to the PNA plane. The amount of the resulted PNA-enhanced electric field is then probed at the middle of the $MoSe_2$ film and is averaged over one unit-cell of the PNA structure. In Figure 6-7(a, b), the electric field profiles of the hybrid nanostructure are drawn in the x-y plane at the two wavelengths of λ_{ex} = 785 nm and λ_{em} = 822 nm, respectively. In Figure 6-7(c, d), we have shown the electric field profile in the x-z plane at the same wavelengths. Using these field profiles, we calculated the excitation enhancement by averaging the intensities of the excitation field ($|E_{exc}|^2$) over one PNA unit cell. The average value of the excitation field enhancement at λ_{ex} = 785 nm is 3.7 (compared to 0.67 at λ_{ex} = 488 nm), which results in ~5.5 times more enhancement for λ_{ex} = 785 nm comparing to λ_{ex} = 488 nm. This is in good agreement with the measured ratio of the enhancement factors shown in Figure 6-6(c, d) (i.e., 25/5 = 5). It should be noted that a

larger portion of the total PL enhancement comes from the enhancement of the emitted light caused by the Purcell effect [17], which requires separate calculations.

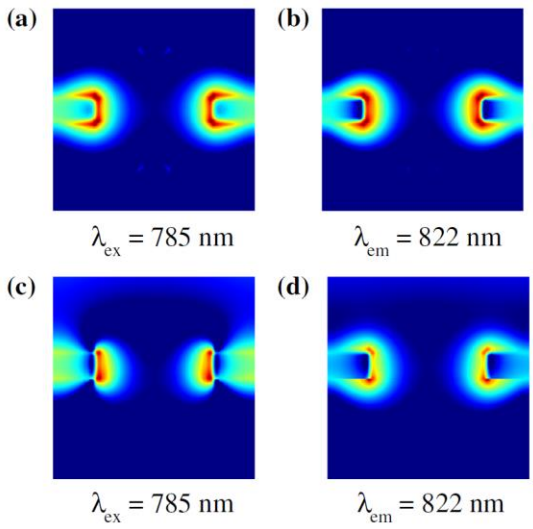

Figure 6-7: Lumerical simulation of hybrid plasmonic-$MoSe_2$ structure. Enhancement (damping) of the pump and PL emission enhancement incurred by the strongly coupled nanoantenna array. (a, b) The x-y cross-section of the normalized field enhancement inside the $MoSe_2$ layer, at excitation (λ_{ex} = 785 nm) and emission (λ_{em} = 822 nm) wavelengths (the colormap is in log scale). The average value of the field enhancement ($\Gamma_{ex} = |E_{ex}|^2$) across the $MoSe_2$ layer is 3.70. (c, d) The x-z cross-sections of the same enhancement factors at 785 and 822 nm wavelength, respectively.

The same simulation approach is used to calculate the reflection of both passive PNA (without $MoSe_2$) and active hybrid PNA-$MoSe_2$ structures and the results are shown in Figure 6-8(a). Also, in Figure 6-8(b), corresponding experimental results are presented for comparison. The presence of two extinction peaks, one at 600 nm wavelength (corresponding to F-P resonance [18]) and one around 800 nm (corresponding to the LP mode of the PNA) seen in simulation results in Figure 6-8(a), agrees well with the experimental measurements in Figure 6-8(b). The differences between the theoretical and experimental extinctions of the passive PNA/SiO_2 structure are due to the lower experimental quality factor (Q) of the LP mode of the PNA caused by the fabrication

imperfections. The results shown in Figure 6-8 imply that the addition of the PNA to the $MoSe_2$ monolayer changes the spectral shape of the extinction. This suggests that by integrating a monolayer of a 2D material with a properly designed PNA, we might be able to shape the PL spectrum of the hybrid structure.

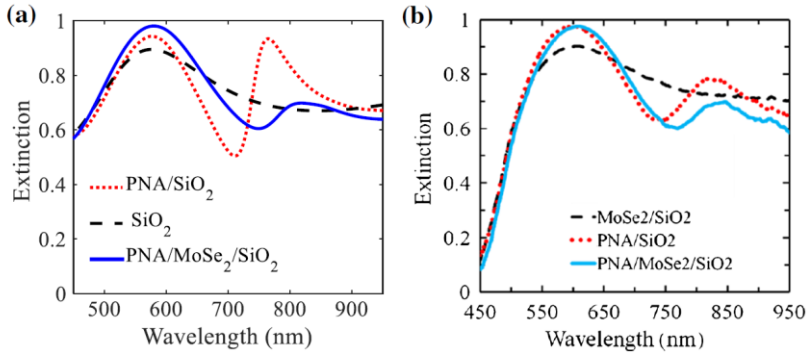

Figure 6-8: Linear responses of the passive and active coupled PNAs. (a) Calculated extinction (i.e., change in the reflection) spectra of the substrate (290 nm-thick thermal SiO_2 on Si, black dashed curve), passive (PNA without ML-$MoSe_2$, red dotted curve), and active (PNA with ML-$MoSe_2$, blue solid curve) structures. The resonance wavelengths of the passive and active arrays are at 766 and 822 nm, respectively, corresponding to a resonance shift of 56 nm in simulations. (b) Measured reflection extinction spectra of the monolayer $MoSe_2$ on substrate (black dashed curve), passive PNA (red dotted curve), and active PNA/$MoSe_2$ structures (black dashed curve). Both simulation and experimental data are for PNAs with the nanoantenna length of l = 105 nm, width of w = 30 nm, thickness of t = 30 nm, and the periodicity of a = 250 nm.

We measured the polarization-dependent extinction of the structures in different regions of Figure 6-5(b), and the results are shown in Figure 6-9. Figure 6-9(a) simply compares the extinction of the three structures at 0° polarization (i.e., the electric field of the excitation light parallel to the horizontal nanorods in Figure 6-5(b)). Figure 6-9(b–d) shows the polarization-dependent extinction of the PNA/SiO_2 (region B), $MoSe_2$/SiO_2 (region C), and PNA/$MoSe_2$/SiO_2 (region A), respectively. While the original device is designed symmetric to have a polarization insensitive response, Figure 6-9(d) shows clear polarization sensitivity of the extinction of the structure since the fabrication imperfections

have resulted in a difference in dimensions of the vertically and horizontally aligned Au nanorods. More importantly, comparison of the extinction spectra shown in Figure 6-9(d) with those shown in Figure 6-9(b, c) clearly suggests that the polarization dependence of the device extinction is primarily caused by the response of the PNA structure and not by the intrinsic polarization-dependent extinction of the ML-$MoSe_2$. While the polarization sensitivity here is caused by fabrication imperfection, Figure 6-9 suggests that by proper design of the PNA, we can engineer the polarization dependence of the structure far beyond what the bare $MoSe_2$ monolayer can offer. This is another indication that by integrating a monolayer of a 2D material with a carefully designed PNA, we can engineer emission properties to a large extent.

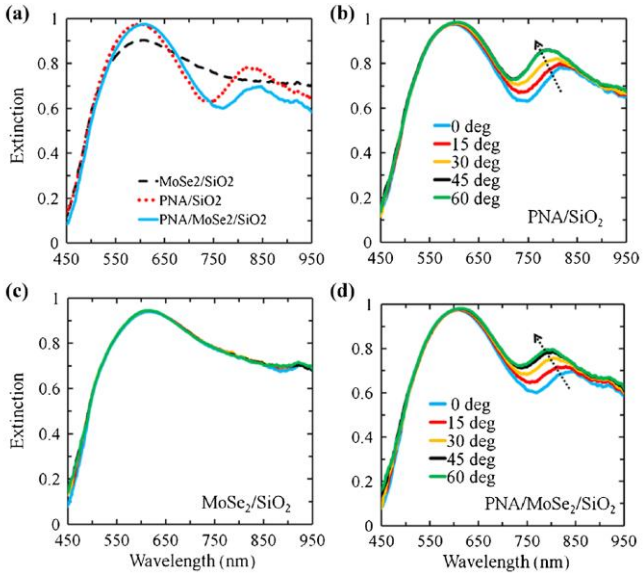

Figure 6-9: Polarization dependence of the extinction coefficient in hybrid PNA/$MoSe_2$ monolayer. (a) Extinction coefficients of the $MoSe_2/SiO_2$ (dashed line), PNA/SiO_2 (dotted line), and $PNA/MoSe_2/SiO_2$ (solid line) parts (as depicted in Figure 6-5(b)), all measured at 0° polarizations, where 0° angle is defined to be parallel to the horizontal nano-antennas. Polarization-resolved extinction coefficient of (b) the PNA/SiO_2, (c) monolayer $MoSe_2$ on SiO_2, and (d) $PNA/MoSe_2/SiO_2$ structures when the polarization of the input light is changed from 0° to 60° in equal steps of 15°. Comparing extinction coefficients of the $MoSe_2$ with and without PNA reveals that the main source of the polarization sensitivity originates from the PNA, which is caused by fabrication imperfections.

Details of the results presented in this chapter are presented in References [18-22]. Results shown in this chapter encourages further consideration of 2D materials in hybrid platforms. For example, there has been a recent surge of interest in finding novel materials to serve as charge (i.e., electron or holes) acceptors in hybrid plasmonic platforms (see for example Reference [23-39]). In such applications, the relative energy barrier between plasmonic metals and acceptor materials is a key parameter for efficient exchange of charged carriers. Thus, considering the variety of 2D TMDs with different band structures combined with the possibility of continuous tuning of the bands using alloying techniques, I believe hybrid plasmonic-2D TMDs can offer a unique platform for studying interesting physics and novel functionalities upon enhancement of light interaction with 2D TMDs. In addition, hybrid platforms may also enable dynamic tuning of optoelectronic properties for semiconducting 2D TMDs, for example, via integration with electrically tunable materials such as phase-change alloys. [40, 41]

6.3 References

1. A. Tarasov, P. M. Campbell, M. Y. Tsai, Z. R. Hesabi, J. Feirer, S. Graham, W. J. Ready, and E. M. Vogel, "Highly Uniform Trilayer Molybdenum Disulfide for Wafer-Scale Device Fabrication," *Adv. Funct. Mater.*, vol. 24, no. 40, pp. 6389–6400, 2014.
2. E. H. M. Balkanski, R.F. Wallis, "Anharmonic Effects in Light Scattering Due to Optical Phonons in Silicon," *Phys. Rev. B*, vol. 28, no. 4, pp. 1928–1934, 1983.
3. J. Menendez, M. Cardona, "Temperature Dependence of the First-Order Raman Scattering by Phonon in Si, Ge, and a-Sn: Anharmonic Effects," *Phys. Rev. B*, vol. 29, no. 4, pp. 2051–2059, 1984.
4. S. Sahoo, A. P. S. Gaur, M. Ahmadi, and R. S. Katiyar, "Temperature-Dependent Raman Studies and Thermal Conductivity of Few-Layer MoS_2," *J. Phys. Chem. C.*, vol. 117, no. 17, pp. 9042-9047, 2013.
5. N. A. Lanzillo, A. Glen Birdwell, M. Amani, F. J. Crowne, P. B. Shah, S. Najmaei, Z. Liu, P. M. Ajayan, J. Lou, M. Dubey, S. K. Nayak, and T. P. O'Regan, "Temperature-Dependent Phonon Shifts in Monolayer MoS2," *Appl. Phys. Lett.*, vol. 103, no. 9, 2013.

6. B. Chakraborty, A. Bera, D. V. S. Muthu, S. Bhowmick, U. V. Waghmare, and A. K. Sood, “Symmetry-Dependent Phonon Renormalization in Monolayer MoS_2 Transistor,” *Phys. Rev. B - Condens. Matter Mater. Phys.*, vol. 85, no. 16, pp. 2–5, 2012.
7. H. C. Chien, D. J. Yao, M. J. Huang, and T. Y. Chang, "Thermal Conductivity Measurement and Interface Thermal Resistance Estimation Using SiO_2 Thin Film," Review of Scientific Instruments, vol. 79, 054902, 2008.
8. S. L. Li, H. Miyazaki, H. Song, H. Kuramochi, S. Nakaharai, and K. Tsukagoshi, “Quantitative Raman Spectrum and Reliable Thickness Identification for Atomic Layers on Insulating Substrates,” *ACS Nano*, vol. 6, no. 8, pp. 7381–7388, 2012.
9. D. H. Lien, J. S. Kang, M. Amani, K. Chen, M. Tosun, H. P. Wang, T. Roy, M. S. Eggleston, M. C. Wu, M. Dubey, S. C. Lee, J. H. He, and A. Javey, “Engineering Light Outcoupling in 2D Materials,” *Nano Lett.*, vol. 15, no. 2, pp. 1356–1361, 2015.
10. Xia J, Huang X, Liu LZ, Wang M, Wang L, Huang B, Zhu DD, Li JJ, Gu CZ, Meng XM (2014) CVD synthesis of large-area, highly crystalline MoSe2 atomic layers on diverse substrates and application to photodetectors. Nanoscale 6:8949–8955
11. Wang X, Gong Y, Shi G, Chow WL, Keyshar K, Ye G, Vajtai R, Lou J, Liu Z, Ringe E, Tay BK, Ajayan PM (2014) Chemical vapor deposition growth of crystalline monolayer MoSe2. ACS Nano 8: 5125–5131
12. Mousavi SHS, Eftekhar AA, Atabaki AH, Adibi A (2015) Bandedge bilayer plasmonic nanostructure for surface enhanced Raman spectroscopy. ACS Photonics 2:1546–1551
13. McMahon MD, Lopez R, Haglund RF, Ray EA, Bunton PH (2006) Second-harmonic generation from arrays of symmetric gold nanoparticles. Phys Rev B 73:041401
14. Zhou W, Dridi M, Suh JY, Kim CH, Co DT, Wasielewski MR, Schatz GC, Odom TW (2013) Lasing action in strongly coupled plasmonic nanocavity arrays. Nat Nanotechnol 8:506–511
15. Zhou W, Odom TW (2011) Tunable subradiant lattice plasmons by out-of-plane dipolar interactions. Nat Nanotechnol 6:423–427
16. Liu HL, Shen CC, Su SH, Hsu CL, Li MY, Li LJ (2014) Optical properties of monolayer transition metal dichalcogenides probed by spectroscopic ellipsometry. Appl Phys Lett 105:201905
17. Gerard JM, Sermage B, Gayral B, Legrand B, Costard E, ThierryMieg V (1998) Enhanced spontaneous emission by quantum boxes in a monolithic optical microcavity. Phys Rev Lett 81:1110–1113
18. 193511 15. Taghinejad H, Taghinejad M, Tarasov A, Tsai MY, Hosseinnia AH, Moradinejad H, Campbell PM, Eftekhar AA, Vogel EM, Adibi A Resonant light-induced heating in hybrid cavity-coupled 2D transition-metal dichalcogenides. ACS Photonics 3:700–707 (2016).
19. H. Taghinejad, M. Taghinejad, A. Tarasov, A. Hosseinnia, H. Moradinejad, A. Eftekhar, E. Vogel, A. Adibi " Enhancement of light-2D material interaction envisioned for energy harvesting applications," CLEO: Science and Innovations, ISBN: 978-1-943580-27-9, San Jose, CA (2017).
20. T. Fan, H. Taghinejad, A. Eftekhar, A. Adibi " Light-matter interaction in 2D material heterostructures," SPIE OPTO, volume 10112, 1011216, Photonic and

Phononic Properties of Engineered Nanostructures VII Conference, San Francisco, CA (2017).
21. T. Fan, A. Eftekhar, H. Taghinejad, P. M. Ajayan, A. Adibi " Optical Properties of MoS2/MoSe2 Heterostructures," Frontiers in Optics, ISBN: 978-1-943580-19-4, Rochester, N. Y. (2016).
22. M. Taghinejad, H. Taghinejad, A. Adibi " Ultra-sharp and tunable lattice plasmons in film-coupled metallic nanostructures," SPIE OPTO, volume 10541, 105410T, Photonic and Phononic Properties of Engineered Nanostructures VIII Conference, San Francisco, CA (2018).
23. M. Taghinejad, H. Taghinejad, Z. Xu, K. T. Lee, S. P. Rodrigues, J. Yan, A. Adibi, T. Lian, W. Cai, Ultrafast Control of Phase and Polarization of Light Expedited by Hot-Electron Transfer. Nano Letters 18, 5544-5551 (2018).
24. M. Taghinejad, H. Taghinejad, Z. Xu, Y. Liu, S. P. Rodrigues, K. T. Lee, T. Lian, A. Adibi, W. Cai, Hot-Electron-Assisted Femtosecond All-Optical Modulation in Plasmonics. Advanced Materials 30, 17049015 (2018).
25. M. Taghinejad, H. Taghinejad, S. T. Malak, H. Moradinejad, E. V. Woods, Z. Xu, Y. Liu, A. A.Eftekhar, T. Lian, V.V. Tsukruk, A. Adibi, A. Sharp and Tunable Crystal/Fano-type Resonances Enabled by Out-of-Plane Dipolar Coupling in Plasmonic Nanopatch Arrays. Annalen Physik (Berlin) 530, 1700395 (2018).
26. M. Taghinejad, Z. Xu, H. Wang, H. Taghinejad, A. Adibi, X. Qian, T. Lian, W. Cai, Photocarrier-Induced Active Control of Second-Order Optical Nonlinearity in Monolayer MoS2. Small, 16, 1906347 (2020).
27. M. Taghinejad, Z. Xu, K. T. Lee, X. Qian, T. Lian, W. Cai, Transient Second-Order Nonlinear Media: Breaking the Spatial Symmetry in the Time Domain via Hot-Electron Transfer. PRL, 124, 013901 (2020).
28. M. Taghinejad, W. Cai, All-optical Control of Light in Micro- and Nano-photonics. ACS Photonics, 6, 1082-1093 (2019).
29. L. Kang, S. P. Rodrigues, M. Taghinejad, S. Lan, K.-T. Lee, Y. Liu, D. H. Werner, A. Urbas, W. Cai, Preserving Spin States upon Reflection: Linear and Nonlinear Responses of a Chiral Meta-Mirror. Nano Lett., 17, 7102-7109 (2017).
30. S. Lan, X. Zhang, M. Taghinejad, S. Rodrigues, K.-T. Lee, Z. Liu, W. Cai, Metasurfaces for near-eye augmented reality. ACS Photonics, 6, 864-870 (2019).
31. S. Lan, S. P. Rodrigues, M. Taghinejad, W. Cai, Dark plasmonic modes in diatomic gratings for plasmoelectronics. Laser & Photonics Reviews, 11, 1600312 (2017).
32. K.-T. Lee, M. Taghinejad, J. Yan, A. S. Kim, L. Raju, D. K. Brown, W. Cai, Electrically Biased Silicon Metasurfaces with Magnetic Mie Resonance for Tunable Harmonic Generation of Light. ACS Photonics, 6, 2663-2670 (2019).
33. M. Taghinejad, W. Cai, Hot-Electron Plasmonics for Ultrafast Control of Intensity, Phase, and Polarization of light. APS April, volume 64, Presented at Bulletin of the American Physical Society Conference, Denver, Co (2019).
34. M. Taghinejad, W. Cai, Field-and Carrier-Induced Nonlinear Metamaterials. CLEO: QELS_Fundamental Science, ISBN: 978-1-943580-42-2, San Jose, CA (2018).
35. M. Taghinejad, W. Cai, Femtosecond All-Optical Control of Plasmons: Hot-Electron versus Phonon Relaxation. APS March Meeting, H18. 004, Presented at APS March Conference, Los Angeles, CA (2018).

36. M. Taghinejad, W. Cai, All-optical modulation of ultrasharp lattice plasmons. IEEE Photonics Conference (IPC), volume 17393102, 647-648, IPC Conference, Orlando, FL (2017).
37. A. Darabi, M. J. Leamy, "Clearance-type nonlinear energy sinks for enhancing performance in electroacoustic wave energy harvesting," Nonlinear Dynamics, 87, no. 4, pp. 2127-2146, 2017.
38. A. Darabi, M. J. Leamy, "Clearance-type nonlinear energy sinks for enhancing performance in electroacoustic wave energy harvesting," Smart Materials and Structures, 26, no. 8, 085015, 2017.
39. A. Darabi, M. J. Leamy, "Reconfigurable topological insulator for elastic waves," The Journal of the Acoustical Society of America, 146, no. 1, 773-781, 2019.
40. H. Taghinejad, S. Abdollahramezani, A. A. Eftekhar, T. Fan, A. H. Hosseinnia, O. Hemmatyar, A. Eshaghian Dorche, A. Gallmon, A. Adibi, ITO-Based -Heaters for Multi-Stage Switching of Phase-Change Materials: Towards Beyond-Binary Reconfigurable Integrated Photonics. arXive (2020), arXiv preprint arXiv:2003.04097 .
41. S. Abdollahramezani, H. Taghinejad, T. Fan, Y. Kiarashinejad, A. A. Eftekhar, A. Adibi, Reconfigurable multifunctional metasurfaces employing hybrid phase-change plasmonic architecture. arXive (2018), arXiv preprint arXiv:1809.08907.

APPENDIX A. MODELING LIGHT-INTERACTION WITH MOS_2 ON THE FP CAVITY

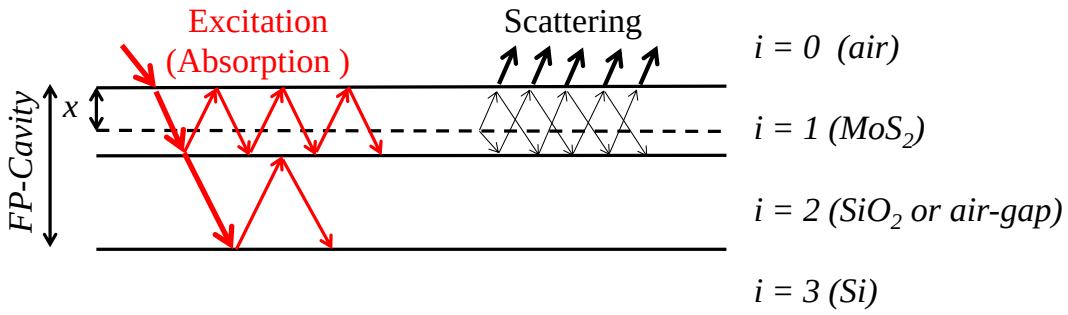

Figure A1: Schematic of the optical path of light in a FP cavity. Absorption (excitation) and scattering parts are shown separately. The depth "*x*" in the MoS_2 layer is highlighted with a dashed line. The trilayer MoS_2 is shown with an exaggerated thickness for the sake of clarity.

Figure A1 illustrates the schematic of the light interference within a FP resonator (having either SiO_2 or air-gap as the cavity), which is used to calculate the enhancement of the E^1_{2g} Raman resonance intensity of the trilayer MoS_2-on-FP sample. Here we have assigned an index i = 0, 1, 2, and 3 to air, MoS_2 film, SiO_2 or air-gap, and silicon (Si), respectively. For the sake of calculations, corresponding refractive indices, which are complex quantities in the most general form, are designated as n_i. Reflection and transmission coefficients of the electric field component of the light at *i-j* boundaries (assuming normal incidence) are defined as $r_{ij} = (n_i - n_j) / (n_i + n_j)$ and $t_{ij} = 2n_i / (n_i + n_j)$. Also, $\beta_i = 2\pi n_i d_i / \lambda$ and $\beta_x = 2\pi n_1 x / \lambda$ are the amount of the phase change that light beam with wavelength λ acquires over a path of length d_i (thickness of *i-th* medium), and length x in the trilayer MoS_2 film (as shown in Figure S5), respectively. Following the ray-tracing method, we calculate the total amplitude of the electric field components of the excitation

(absorption) light (i.e., E_{ex} or E_{ab}) at wavelength λ and the corresponding E^1_{2g} Raman scattered light (E_{sc}) at depth x of the MoS_2 film as follows:

$$E_{ex} = t_{01}.\frac{e^{-i\beta x}+Re^{-i(2i\beta_1-\beta x)}}{1+Rr_{01}e^{-i2\beta x}}, \qquad \text{(A1)}$$

and

$$E_{sc} = t_{01}.\frac{e^{-i\beta x}+Re^{-i(2i\beta_1-\beta x)}}{1+Rr_{01}e^{-i2\beta x}}, \qquad \text{(A2)}$$

where, $R = \frac{r_{12}+r_{23}e^{-i2\beta_2}}{1+r_{12}r_{23}e^{-i2\beta_2}}$ is the effective reflection coefficient at the MoS_2/SiO_2 or MoS_2/air-gap boundaries for a light of wavelength λ. Note that, although equations describing E_{ex} (or E_{ab}) and E_{sc} are similar, they work at different wavelengths of λ_{ex} (or λ_{ab}) and λ_{sc} that relate to each other as follows:

$$\frac{1}{\lambda_{ex}} - \frac{1}{\lambda_{sc}} = E^1_{2g}\ resonance\ wavenumber \quad \text{(A3)}$$

Thereby, the output intensity of the E^1_{2g} Raman light is

$$I_{E^1_{2g}} = \int_0^{d_1} |E_{ab}(x)E_{sc}(x)|^2\, dx \qquad (A4)$$

Therefore, based on Equation (S5), total enhancement factor (TEF) is defined as:

$$\text{TEF} = I_{E^1_{2g}}(MoS_2\text{-on-FP}) \,/\, I_{E^1_{2g}}\ (MoS_2\text{-on-Si}) \quad \text{(A5)}$$

Note that the wavelength-dependent refractive index of the trilayer MoS_2 film, used in the modeling, over a wavelength range of 390-900 nm is shown in Figure A2.

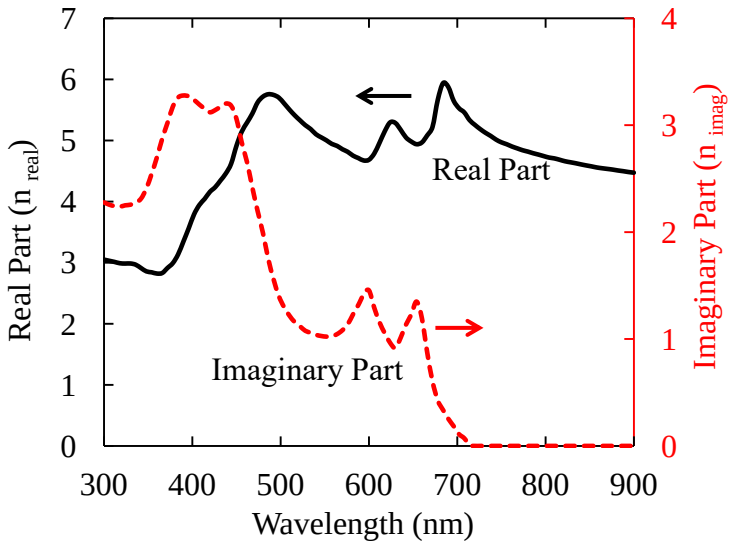

Figure A2: Refractive index of MoS_2. Real (left axis) and imaginary (right axis) parts of the refractive index of the MoS_2 at different wavelengths used for the modeling of the light-MoS_2 interaction.

Based on above discussions and the schematic of Figure A1, light absorption (Ab) and light scattering (S) by the trilayer MoS_2 film can be computed as:

$$\text{Ab} = \int_0^{d_1} |E_{ab}(x)|^2 \, dx \,, \quad \text{(A6)}$$

and

$$\text{S} = \int_0^{d_1} |E_{sc}(x)|^2 \, dx \,, \quad \text{(A7)}$$

where E_{ab} and E_{sc} are the electric field amplitudes of the light inside the MoS_2 film and the scattered light outside the film, respectively. Therefore, absorption enhancement factor (AEF) and scattering enhancement factor (SEF) are defined as:

$$\text{AEF} = \text{Ab } (MoS_2\text{-on-FP}) \,/ \text{Ab } (MoS_2\text{-on-Si}) \quad \text{(A8)}$$

$$\text{SEF} = \text{S } (MoS_2\text{-on-FP}) \,/ \text{S } (MoS_2\text{-on-Si}) \quad \text{(A9)}$$

APPENDIX B. THICKNESS-DEPENDENT ENHANCEMENT OF LIGHT INTERACTION WITH MOS_2

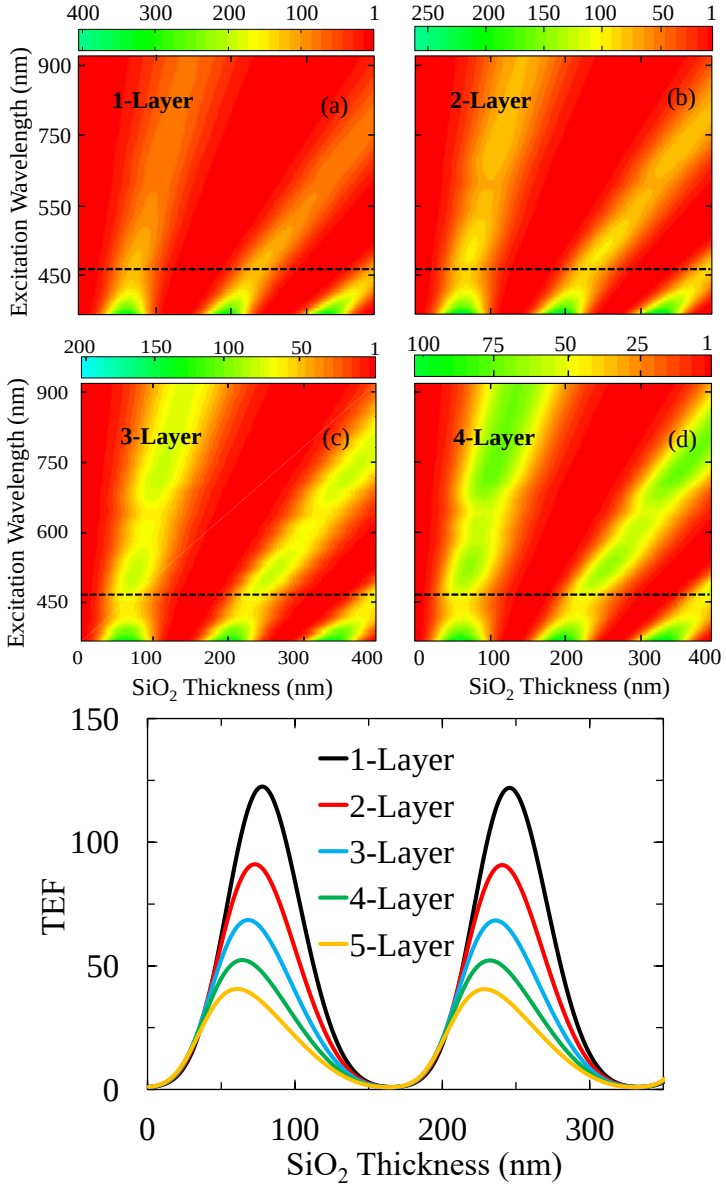

Figure B1: The MoS_2 thickness-dependent TEF. The 2D map of TEF for (a) 1-layer, (b) 2-layer, (c) 3-layer, and (d) 4-layer MoS_2 films. The color-bars represent the expected TEF induced by the FP resonance. (e) The comparison of TEFs that can be achieved for samples with the MoS_2 films of various thicknesses ranging from one to five layers when the samples are excited at 488 nm laser line (corresponding to the dashed lines overlaid on the 2D maps of (a)-(d)).

Two important observations can be made from Figure B1. First, increasing the number of the MoS_2 layers decreases the potential enhancement that can be achieved upon integration of the MoS_2 films on the FP resonators. This effect can be explained on the basis of the large imaginary part of the refractive index of MoS_2 at 488 nm (~ 1.65), which causes optical loss and lowers the quality factor of the cavity. That is, in samples with thicker MoS_2 films, light travels a longer path in the lossy part of the cavity and therefore gains lower enhancement. Second, for thicker MoS_2 samples, maximum TEF is achievable at a shorter cavity length. This fact can be explained based on the effective optical length (EOL) of the cavity as defined below:

$$EOL = n_{SiO_2} d_{SiO_2} + n_{MoS_2} d_{MoS_2}, \quad \text{(B1)}$$

where, 'n' and 'd' are, respectively, refractive index and thickness of the SiO_2 and MoS_2 layers. As discussed in the main text, the maximum enhancement can be reached when the optical length is designed so that cavity acts as a quarter waveplate. Therefore, increasing the number of MoS_2 layers (i.e., d_{MoS_2} in Eq. (B1)) decreases the required SiO_2 thickness needed to satisfy the condition for maximum TEF. For instance, considering the refractive index of MoS_2 at $\lambda = 488$ nm to be 5.8 (Figure A2) and the thickness of an individual layer to be 0.8 nm, the optical length in the MoS_2 film increases from 4.6 nm in the 1-layer sample (i.e., 5.8×(1×0.8)) to 23.2 nm in the 5-layer sample (i.e., 5.8×(5×0.8)). Thus, based on Eq. (B1), this change is balanced by the decrease in the SiO_2 thickness. Figure B1 (e) shows that the amount of decrease in the SiO_2 thickness (at maximum TEF) equals the amount of increase in the optical length imposed by increasing the number of MoS_2 layers.